Met Office

Developments in the Met Office InTEM volcanic ash source estimation system Part 2: Results

Forecasting Research Technical
Report No: 618

15/9/2017

H. N. Webster, D. J. Thomson and M. C. Cooke

Contents

Abstract

The Met Office's volcanic ash inversion system uses satellite observations of volcanic ash clouds and results from the NAME dispersion model to estimate volcanic ash source characteristics. This report describes the effects of a number of changes which have been made to the system. The main changes are in the method of coarse-graining the satellite data, in the algorithm used to find the optimal source characteristics, and in the *a priori* emission model. This report focuses on describing the effects of the changes, with the changes themselves presented in a companion report (Thomson, D. J., H. N. Webster and M. C. Cooke, Developments in the Met Office InTEM volcanic ash source estimation system Part 1: Concepts. *Forecasting Research Technical Report* 616, Met Office, UK). The effects are explored by applying the inversion system to the eruptions of Grímsvötn in 2011 and Eyjafjallajökull in 2010. The main benefit arises from the changes in the algorithm used to solve the optimisation problem. These changes result in a substantial reduction in computational cost and a more complete convergence to the optimal solution. The changes in the *a priori* emission model, while being significant conceptual improvements, make only minor differences to the results. These minor differences seem beneficial, although it is difficult to draw definitive conclusions from the limited number of cases studied here.

1 Introduction

An operational method for estimating volcanic ash emissions was implemented at the Met Office in January 2015. This method is described by Pelley et al. [5] and uses the InTEM (Inversion Technique for Emissions Modelling) inversion system and the NAME (Numerical Atmospheric-Dispersion Modelling Environment) atmospheric dispersion model. Following the operational implementation, some modifications to the system have been investigated and implemented. The modifications are described in a companion report [7] and results are presented here. The modifications include changes to the way the satellite retrievals are converted from their original resolution to match the coarser resolution of the NAME model output, changes to the solution algorithm in order to reduce the run time and improve the efficiency of the code, and changes to the *a priori* description of the source (in the Bayesian sense) resulting in a more consistent (although still not completely consistent) statistical representation of the problem. All the results presented here use the new method of converting the satellite data resolution to match the resolution of the NAME output. We introduce the other modifications incrementally (see sections 2-5), validating and assessing the impact of the introduced changes at each stage using the eruption of Eyjafjallajökull in 2010 and the eruption of Grímsvötn in 2011 as test scenarios. The tests are conducted in a 'rolling framework', showing how the estimates of the emissions change as more satellite data becomes available. Results are expressed throughout in terms of the effective ash emissions. These are defined as the emissions suitable for use in a passive dispersion model which is aimed at predicting the distal plume and which doesn't treat near source processes such as plume rise and the near source fall out of large particles or of small particles via aggregation processes.

The error assumptions and whether they seem plausible in the light of the available data are investigated in section 6. For example we explore whether the *a posteriori* emission estimates are consistent with the uncertainty range for the *a priori* emission estimates. Similarly we explore whether the uncertainty range for the (*a posteriori*) estimates made using the satellite data available up to a given time are consistent with later estimates made when more satellite data becomes available.

In section 7 we compare the concentration predictions using the *a posteriori* emissions with a range of independent (non-satellite) data which was not used in the inversion. The dataset used is that considered by Webster et al. [8] and consists of ground and aircraft based concentration measurements. The results are assessed using the same metrics that were used by Webster et al. [8].

Finally, in the appendices we explore the convergence of the original simulated annealing solution algorithm, the sensitivity of results to some of the parameters in the new *a priori* model and the sensitivity of results to the height-time resolution with which the emissions are discretised.

This report should be read in conjunction with [5] and [7].

2 A base case - the original Pelley et al. code

We begin with the Pelley et al. [5] code in order to provide a base case from which to assess the impacts of all future modifications. A description of the method and details of the technique can be found in Pelley et al. [5].

Note that, as discussed above, the processing of the satellite observations has changed since the work of Pelley et al. [5], with the method of combining ash and clear sky data onto the coarser NAME grid being modified to avoid any biases in regions with both types of data. Additional minor changes include extending the geographical region over which observations are used in the inversion. The code tested here also includes some minor bug fixes. These bugs affected the calculation of the analysis (i.e. *a posteriori*) error and the uncertainty reduction from the *a priori* error to the analysis error, but did not affect the determined solution.

2.1 Grímsvötn 2011

The eruption of Grímsvötn (64.42°N, 17.33°W) at 19:13 UTC on 21/05/2011 lasted approximately four days, ending at 02:30 UTC on 25/05/2011. Figure 1 shows the *a priori* mean effective emission profile which is based on observations of the eruption plume height, the Mastin relationship between eruption plume height and mass eruption rate [4], and the assumption of a 5% distal fine ash fraction, following the approach described in [5]. Despite the assumption of a uniform vertical profile for the *a priori* source, the source resolution can result in less mass being released in the highest source elements (when the eruption plume height lies below the top of the highest source element or varies in time so as to lie for a time in some lower source elements) giving a non-uniform profile for the *a priori* mean source. The uncertainty in the *a priori* eruption plume height is assumed, as in [5], to be $\pm$2 km.

Satellite retrievals of ash column loadings and clear sky regions from SEVIRI data provide observations from the Grímsvötn eruption for the inversion system. Satellite retrievals until 00:00 UTC 31/05/2011 are used, thereby allowing observations of ash remaining in the atmosphere past the end of the eruption to be included in the inversion.

Figure 2 shows the modelled plume between 23:00 UTC on 22/05/2011 and 00:00 UTC on 23/05/2011 using the *a priori* mean emission profile from figure 1. The *a priori* plume is located, at this time, over, and mainly to the north of, Iceland. In comparison to satellite retrievals valid at this time (see figures 4a and 6a), the *a priori* source over-estimates the ash quantities within the plume substantially.

2.1.1 Ash-only observations

After processing, a total of 3293 satellite observations of volcanic ash from the 2011 Grímsvötn eruption are available to use with the volcanic ash inversion system to determine the best fit emis-

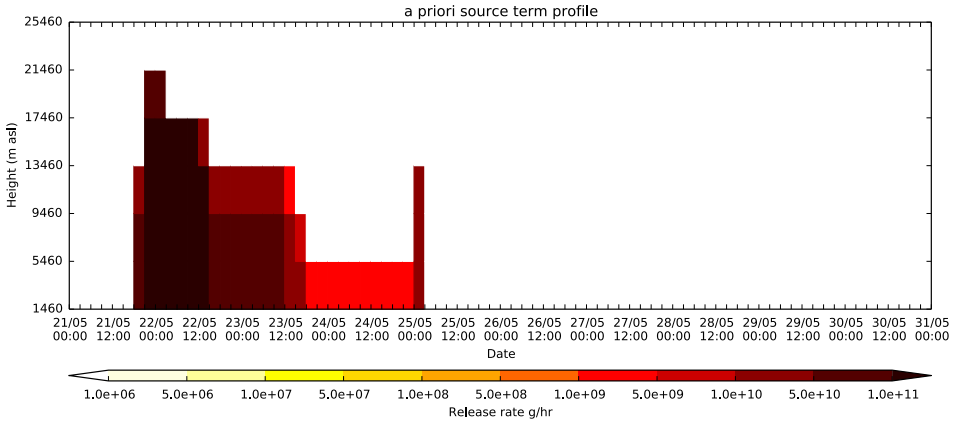

Figure 1: The *a priori* mean emission profile for the eruption of Grímsvötn in May 2011.

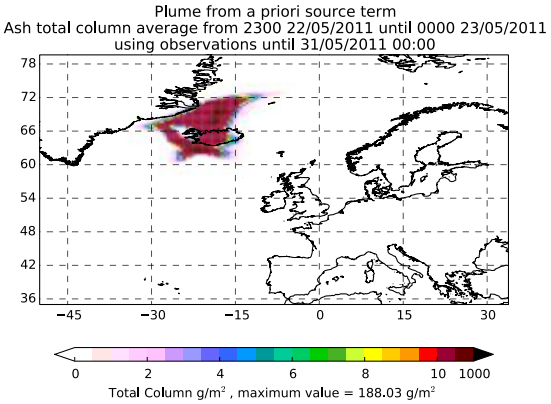

Figure 2: The NAME plume averaged between 23:00 UTC on 22/05/2011 and 00:00 UTC on 23/05/2011 for the 2011 Grímsvötn eruption, obtained using the *a priori* mean emission profile in figure 1.

sion profile. Figure 3 shows the *a posteriori* best fit source (with three hourly time resolution and 4 km vertical resolution) determined using ash-only observations until the dates shown and using the Pelley et al. [5] inversion code. One can see that there is, in all cases, a large reduction in the effective emitted mass when compared to the *a priori* source (cf. figure 1).

The best fit emission profile can then be used in NAME to give a prediction of the transport and spread of the ash plume. Figure 4 shows the modelled plume between 23:00 UTC on 22/05/2011 and 00:00 UTC on 23/05/2011 using the *a posteriori* emission profiles in figure 3, together with the ash observations from the satellite retrieval valid at the same time. The *a posteriori* source leads to an ash plume with a large reduction in mass relative to the *a priori* plume (cf. figure 2).

2.1.2 Ash and clear sky observations

Using both volcanic ash and clear sky satellite observations, a total of 88791 observations from the 2011 Grímsvötn eruption are available after processing for use with the volcanic ash inversion system to determine the best fit emission profile. Figure 5 shows the *a posteriori* best fit source (again with three hourly time resolution and 4 km vertical resolution) determined using all satellite observations (both ash and clear skies) until the dates shown and using the Pelley et al. [5] inversion code. The use of clear sky observations, in addition to the ash observations, reduces the mass further in the eruption emission profile.

Figure 6 shows the modelled plume between 23:00 UTC on 22/05/2011 and 00:00 UTC on 23/05/2011 using the *a posteriori* emission profiles in figure 5, together with the ash and clear sky observations from the satellite retrieval valid at the same time. The clear sky satellite observations are shown in brown in figure 6a. Using the *a posteriori* source, there is a large reduction in the mass of ash predicted within the plume. In particular, the ash cloud to the north of Iceland is removed from the predicted plume when a good number of observations are included.

2.2 Eyjafjallajökull 2010

The eruption of an ash cloud from the Icelandic volcano Eyjafjallajökull (63.63°N, 19.62°W) started at approximately 09:00 UTC on 14/04/2010 and continued for nearly 40 days. Reports of the eruption plume height, based on radar observations, were obtained throughout the event from the Icelandic Meteorological Office (IMO). Figure 7 shows the *a priori* mean effective emission profile which is based on these plume height observations, the Mastin relationship linking the mass eruption rate with the eruption plume height [4], and the assumption of a 5% distal fine ash fraction. The uncertainty in the *a priori* eruption plume height is again assumed to be ± 2 km.

Satellite retrievals of ash column loadings and clear sky regions from SEVIRI data provide observations from the 2010 Eyjafjallajökull eruption. Satellite data from the start of the eruption until 23:00 UTC on 29/05/2010 are used here in the inversion.

Figure 8 shows the modelled plume between 17:00 UTC and 18:00 UTC on 06/05/2010 using

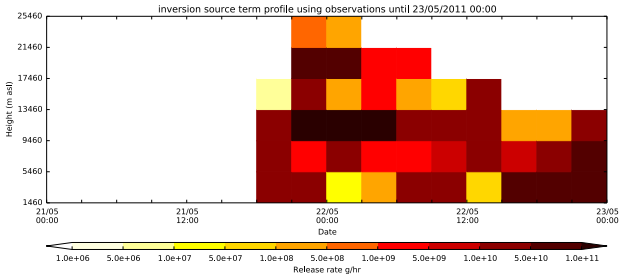

(a) emissions using satellite retrievals up to 00:00 UTC 23/05/2011

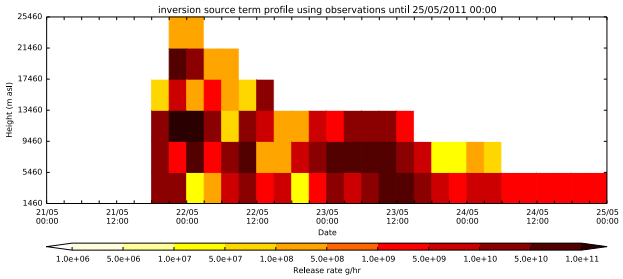

(b) emissions using satellite retrievals up to 00:00 UTC 25/05/2011

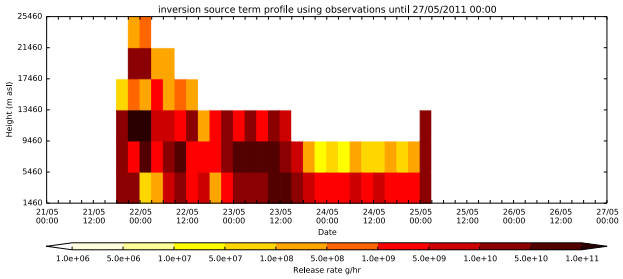

(c) emissions using satellite retrievals up to 00:00 UTC 27/05/2011

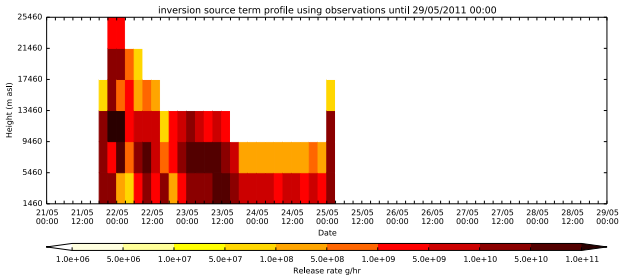

(d) emissions using satellite retrievals up to 00:00 UTC 29/05/2011

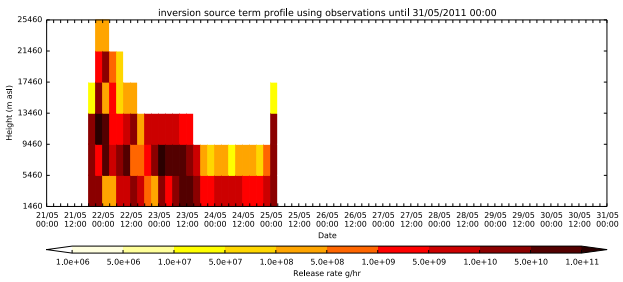

(e) emissions using satellite retrievals up to 00:00 UTC 31/05/2011

Figure 3: The best fit emission profile for the eruption of Grímsvötn using ash-only satellite observations and the Pelley et al. [5] inversion code. (Note the different scales used along the time axis.)

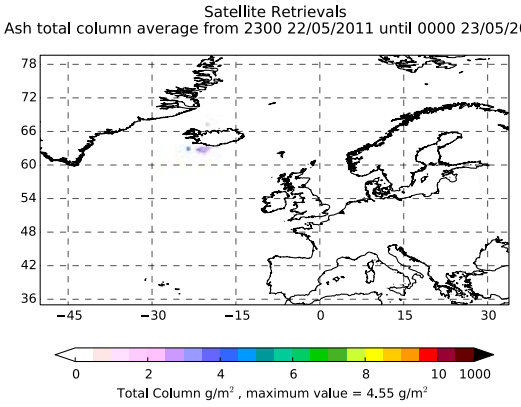

(a) ash-only satellite retrievals

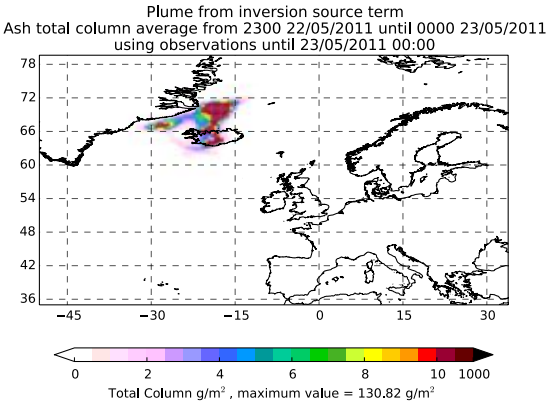

(b) plume using retrievals up to 00:00 UTC 23/05/2011

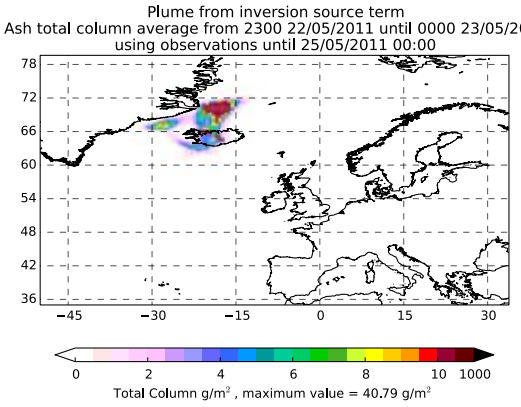

(c) plume using retrievals up to 00:00 UTC 25/05/2011

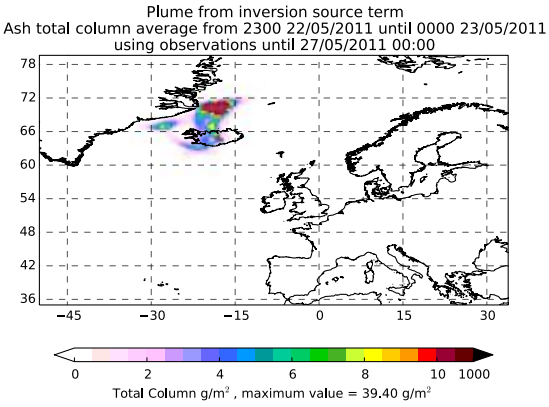

(d) plume using retrievals up to 00:00 UTC 27/05/2011

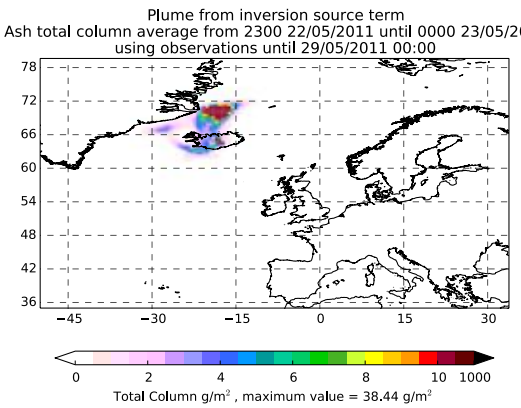

(e) plume using retrievals up to 00:00 UTC 29/05/2011

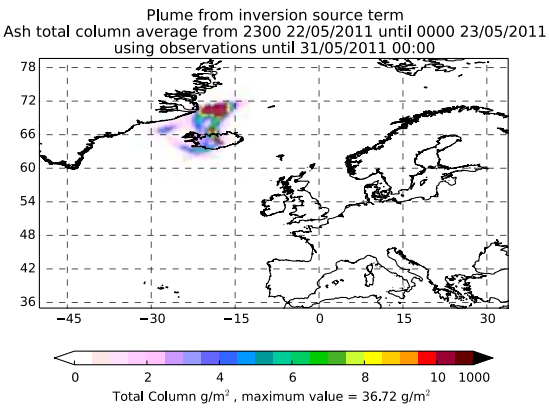

(f) plume using retrievals up to 00:00 UTC 31/05/2011

Figure 4: The Grímsvötn plume averaged between 23:00 UTC on 22/05/2011 and 00:00 UTC on 23/05/2011: (a) as observed by satellite (ash only); and (b-f) as predicted by NAME with emissions determined using ash-only satellite observations and the Pelley et al. [5] inversion code.

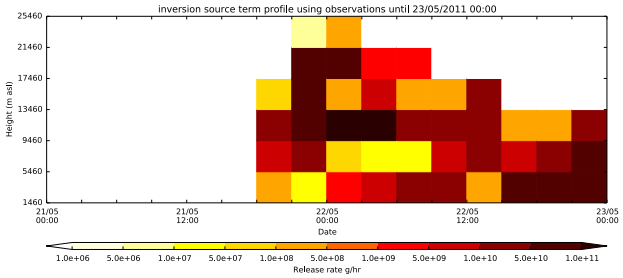

(a) emissions using satellite retrievals up to 00:00 UTC 23/05/2011

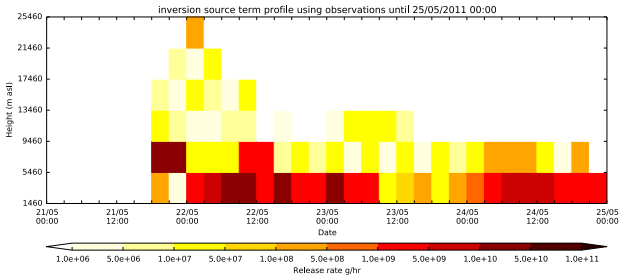

(b) emissions using satellite retrievals up to 00:00 UTC 25/05/2011

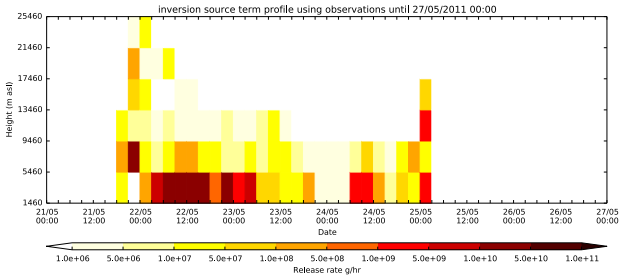

(c) emissions using satellite retrievals up to 00:00 UTC 27/05/2011

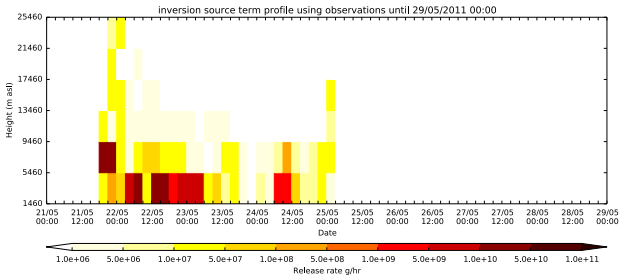

(d) emissions using satellite retrievals up to 00:00 UTC 29/05/2011

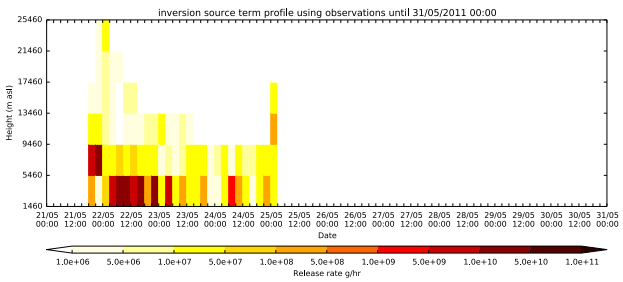

(e) emissions using satellite retrievals up to 00:00 UTC 31/05/2011

Figure 5: The best fit emission profile for the eruption of Grímsvötn using both ash and clear sky satellite observations and the Pelley et al. [5] inversion code. (Note the different scales used along the time axis.)

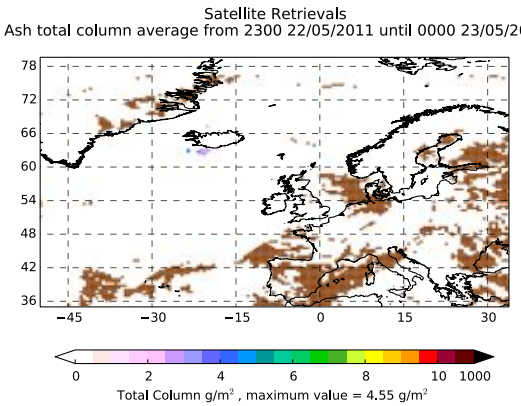

(a) ash and clear sky satellite retrievals

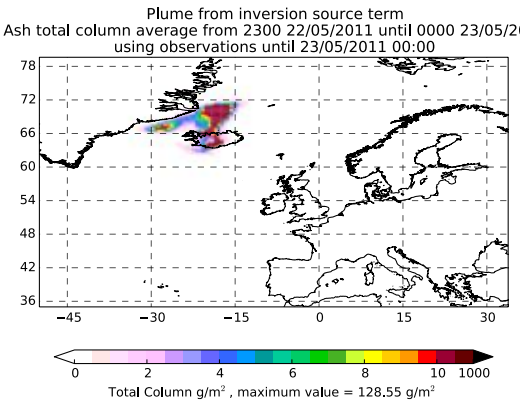

(b) plume using retrievals up to 00:00 UTC 23/05/2011

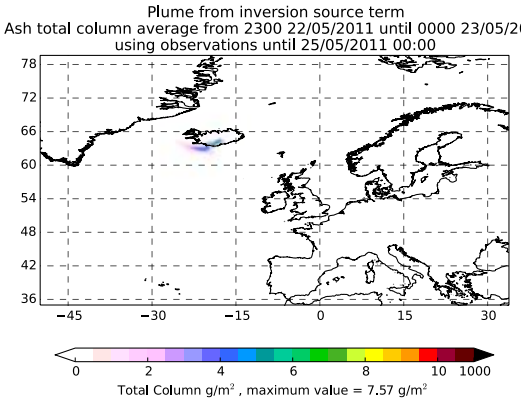

(c) plume using retrievals up to 00:00 UTC 25/05/2011

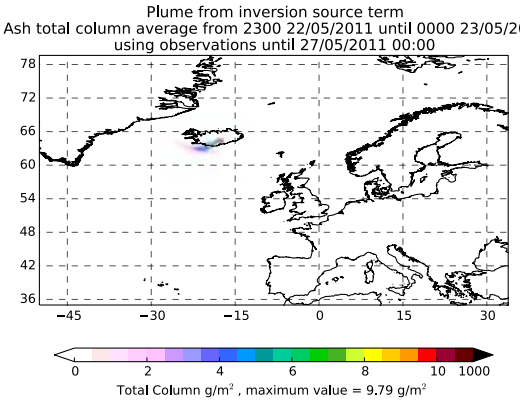

(d) plume using retrievals up to 00:00 UTC 27/05/2011

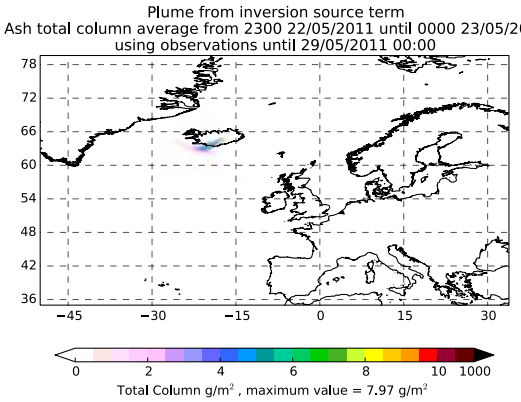

(e) plume using retrievals up to 00:00 UTC 29/05/2011

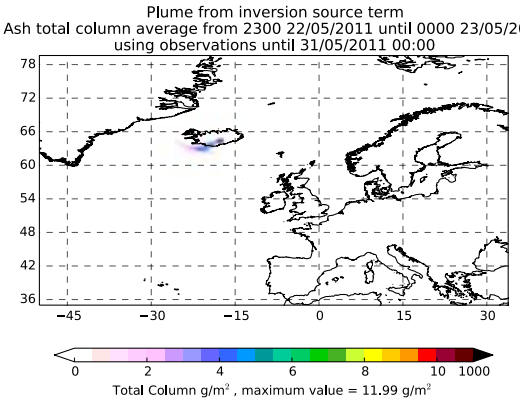

(f) plume using retrievals up to 00:00 UTC 31/05/2011

Figure 6: The Grímsvötn plume averaged between 23:00 UTC on 22/05/2011 and 00:00 UTC on 23/05/2011: (a) as observed by satellite (ash and clear skies, with clear skies shown in brown); and (b-f) as predicted by NAME with emissions determined using both ash and clear sky satellite observations and the Pelley et al. [5] inversion code.

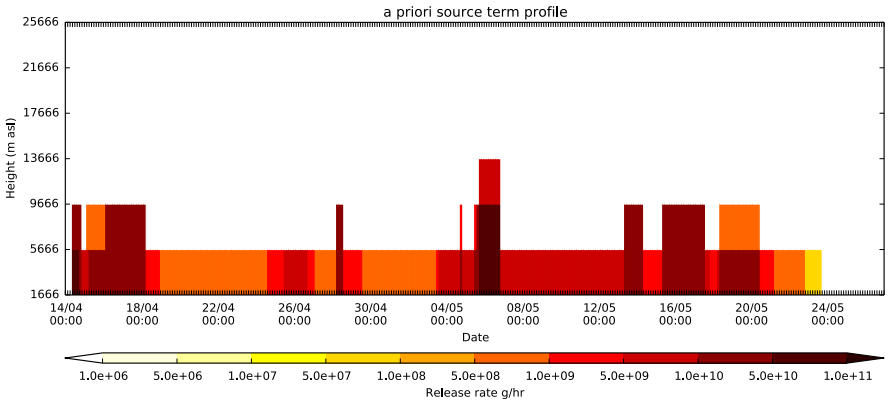

Figure 7: The *a priori* mean emission profile for the eruption of Eyjafjallajökull in 2010.

the *a priori* mean source from figure 7. The *a priori* plume is located, at this time, south of Iceland over the North Atlantic. In comparison to satellite retrievals valid at this time (see figures 10a and 12a), the *a priori* source over-estimates the ash quantities within the plume.

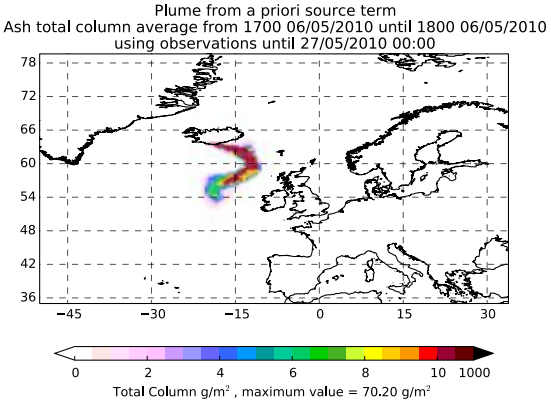

Figure 8: The NAME plume averaged between 17:00 UTC and 18:00 UTC on 06/05/2010 for the 2010 Eyjafjallajökull eruption, obtained using the *a priori* mean emission profile in figure 7.

2.2.1 Ash-only observations

After processing, a total of 40047 satellite observations of volcanic ash from the 2010 Eyjafjallajökull eruption are available to use with the volcanic ash inversion system to determine the best fit emission profile. Figure 9 shows the *a posteriori* best fit emission profile (with three hourly time resolution and 4 km vertical resolution) determined using ash-only observations until the dates shown and using the Pelley et al. [5] inversion code. As was seen for the Grímsvötn 2011 example, the effective emitted mass in the *a posteriori* source is less than that in the *a priori* source (cf. figure 7).

Figure 10 shows the modelled plume between 17:00 UTC and 18:00 UTC on 06/05/2010 using the *a posteriori* emission profiles in figure 9, together with the ash observations from the satellite retrieval valid at the same time. The *a posteriori* source leads to an ash plume with a large reduction in ash mass relative to the *a priori* plume.

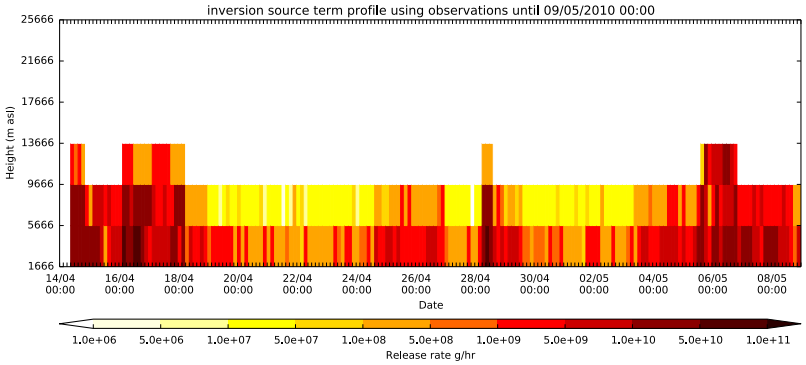

(a) emissions using satellite retrievals up to 00:00 UTC 09/05/2010

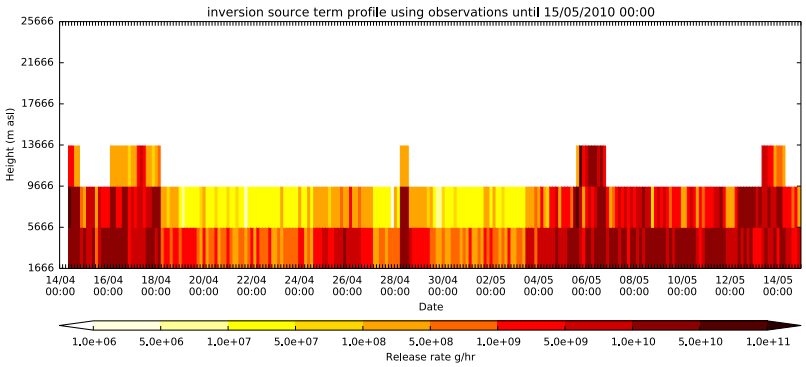

(b) emissions using satellite retrievals up to 00:00 UTC 15/05/2010

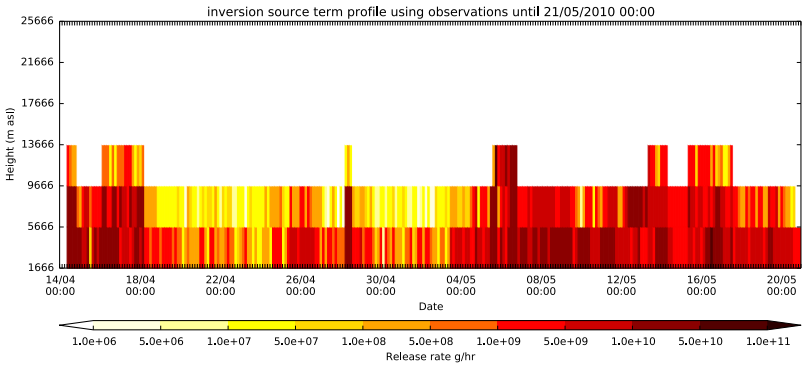

(c) emissions using satellite retrievals up to 00:00 UTC 21/05/2010

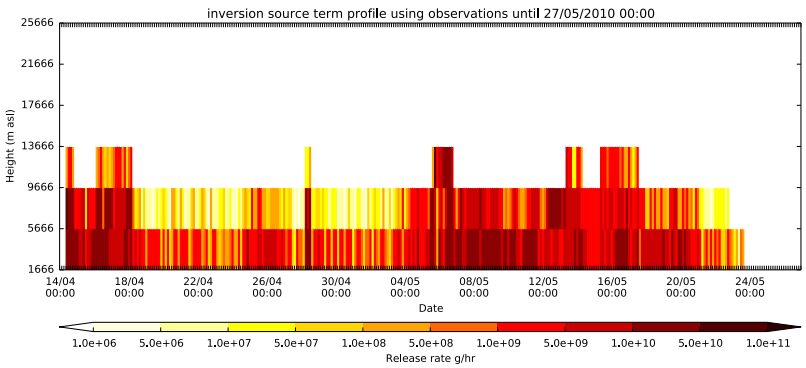

(d) emissions using satellite retrievals up to 00:00 UTC 27/05/2010

Figure 9: The best fit emission profile for the eruption of Eyjafjallajökull using ash-only satellite observations and the Pelley et al. [5] inversion code. (Note the different scales used along the time axis.)

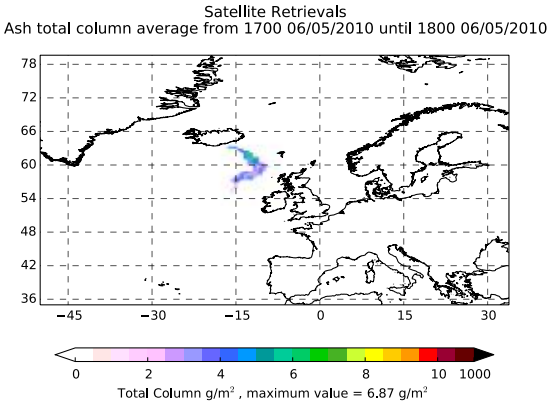

(a) ash-only satellite retrievals

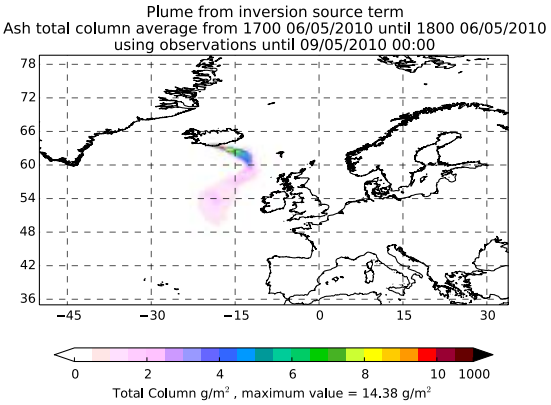

(b) plume using retrievals up to 00:00 UTC 09/05/2010

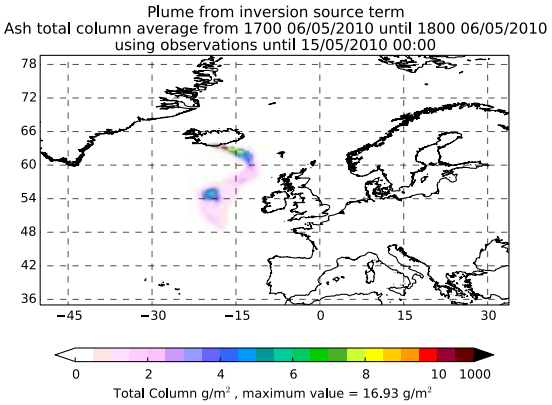

(c) plume using retrievals up to 00:00 UTC 15/05/2010

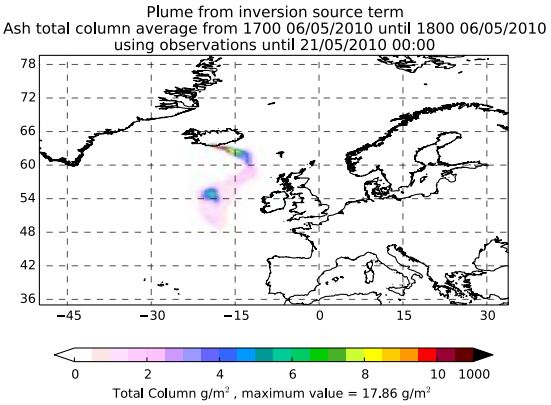

(d) plume using retrievals up to 00:00 UTC 21/05/2010

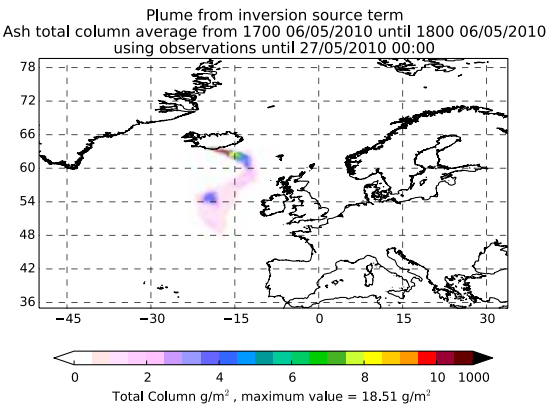

(e) plume using retrievals up to 00:00 UTC 27/05/2010

Figure 10: The Eyjafjallajökull plume averaged between 17:00 UTC and 18:00 UTC on 06/05/2010: (a) as observed by satellite (ash only); and (b-e) as predicted by NAME with emissions determined using ash-only satellite observations and the Pelley et al. [5] inversion code.

2.2.2 Ash and clear sky observations

Using both volcanic ash and clear sky satellite observations, a total of 689492 observations from the 2010 Eyjafjallajökull eruption are available after processing for use with the volcanic ash inversion system to determine the best fit emission profile. Figure 11 shows the *a posteriori* best fit source (again with three hourly time resolution and 4 km vertical resolution) determined using all satellite observations (both ash and clear skies) until the dates shown and using the Pelley et al. [5] inversion code. As was the case for Grímsvötn, the use of clear sky observations, in addition to the ash observations, reduces the mass further in the eruption emission profile.

Figure 12 shows the modelled plume between 17:00 UTC and 18:00 UTC on 06/05/2010 using the *a posteriori* emission profiles in figure 11, together with the ash observations from the satellite retrieval valid at the same time. Using the *a posteriori* source determined using both ash and clear sky satellite observations, there is a further reduction in the mass of ash predicted within the plume. In particular, the ash cloud to the west of Ireland is removed from the predicted plume when clear sky observations are included.

2.3 Simulated annealing convergence

During testing conducted here, an issue with the simulated annealing solver became apparent. The inversion scheme under the rolling framework was continued past the end of the available satellite observations (and long past the end of the eruption). With no new observations available, the best fit for the eruption emission profile should be the same as that given by the previous inversion. However, this is not the case when using the simulated annealing solver, with two inversions using the same satellite observations yielding different solutions. The two solutions differ quite significantly in places and have slightly different values for the cost function (for further details see appendix A). Of course we don't expect complete converge in a finite number of steps. However it is interesting to note that the results are different for two situations that are mathematically equivalent but are presented to the code in two different ways. The simulated annealing technique employed is a slightly modified version of that given by Press et al. [6, pp. 443-447], with the modification requiring all source component emissions to be strictly positive. It seems possible that this "> 0" restriction slows down the convergence rate of the approach, and possibly prevents complete convergence, even asymptotically in the limit of infinitely many steps. Certainly, with the parameters and stopping criteria used, it gets close, but not 'very close', to the best fit emission profile. The Lawson and Hanson method [3] for solving non-negative least squares (NNLS) problems, which allows the source to have zero components, seems to converge better (see section 4 below).

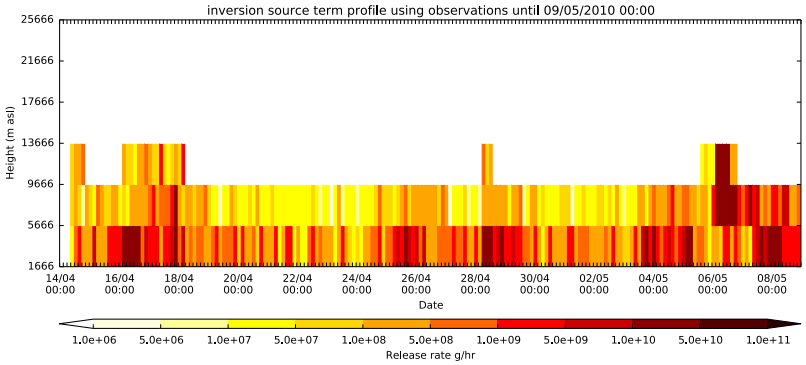

(a) emissions using satellite retrievals up to 00:00 UTC 09/05/2010

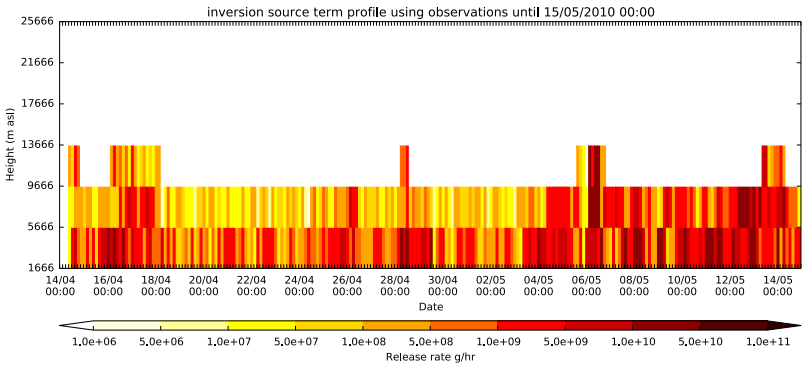

(b) emissions using satellite retrievals up to 00:00 UTC 15/05/2010

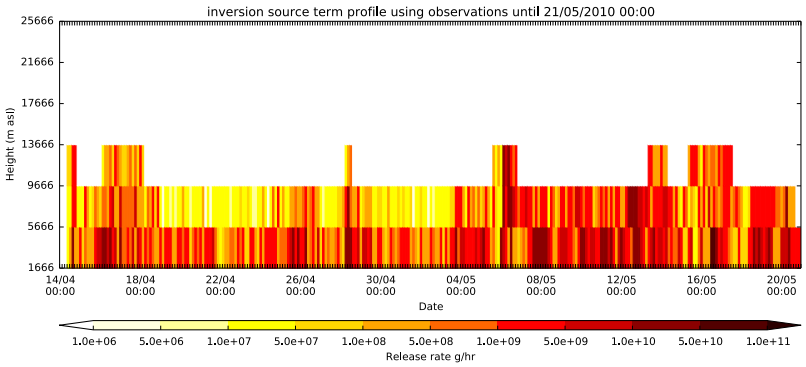

(c) emissions using satellite retrievals up to 00:00 UTC 21/05/2010

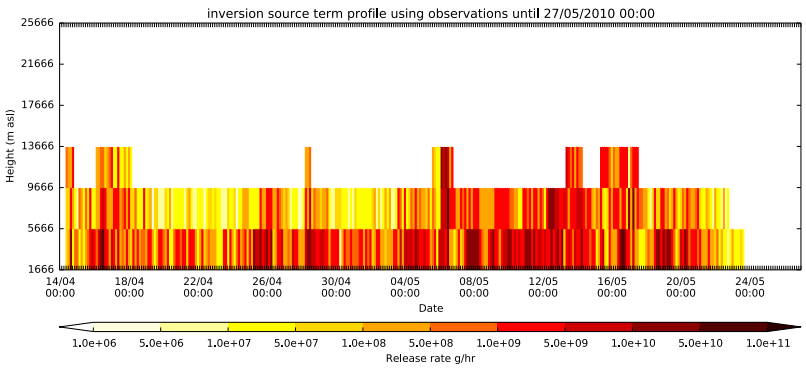

(d) emissions using satellite retrievals up to 00:00 UTC 27/05/2010

Figure 11: The best fit emission profile for the eruption of Eyjafjallajökull using both ash and clear sky satellite observations and the Pelley et al. [5] inversion code. (Note the different scales used along the time axis.)

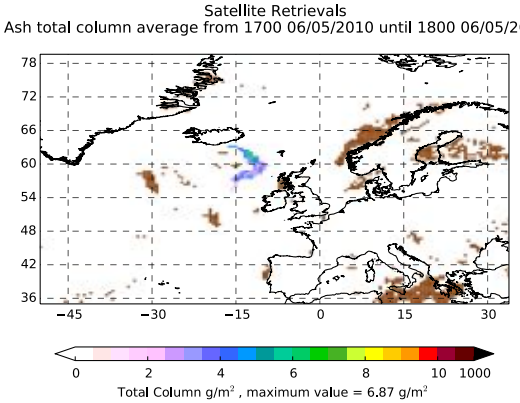

(a) ash and clear sky satellite retrievals

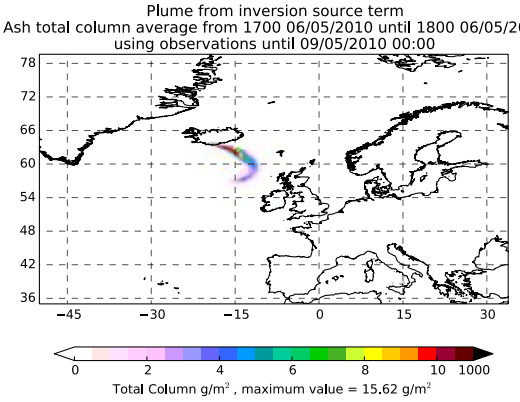

(b) plume using retrievals up to 00:00 UTC 09/05/2010

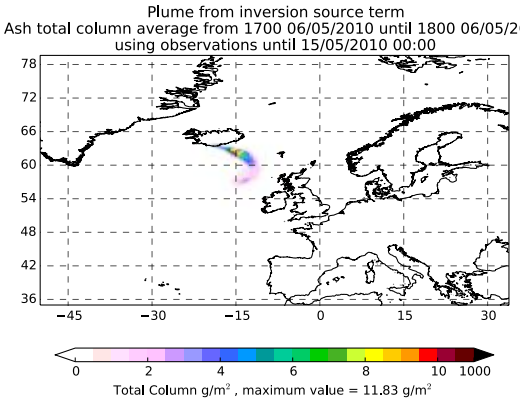

(c) plume using retrievals up to 00:00 UTC 15/05/2010

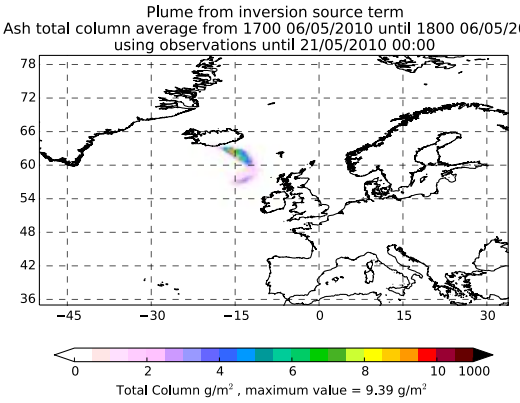

(d) plume using retrievals up to 00:00 UTC 21/05/2010

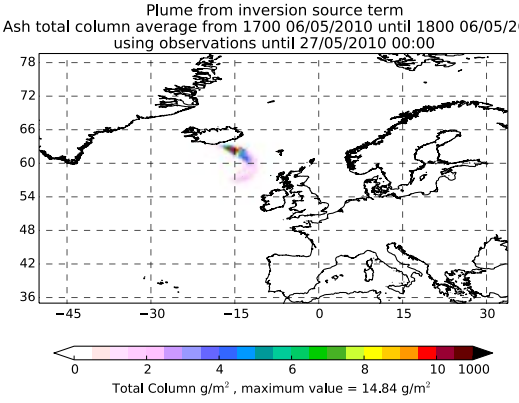

(e) plume using retrievals up to 00:00 UTC 27/05/2010

Figure 12: The Eyjafjallajökull plume averaged between 17:00 UTC and 18:00 UTC on 06/05/2010: (a) as observed by satellite (ash and clear skies, with clear skies shown in brown); and (b-e) as predicted by NAME with emissions determined using both ash and clear sky satellite observations and the Pelley et al. [5] inversion code.

3 Pre-calculation of the cost function coefficients

The cost function to be minimized is given by

$$J(\mathbf{e}) = (\mathbf{Me} - \mathbf{o}_a)^T \mathbf{R}^{-1} (\mathbf{Me} - \mathbf{o}_a) + (\mathbf{e} - \mathbf{e}_{ap})^T \mathbf{B}^{-1} (\mathbf{e} - \mathbf{e}_{ap}), \quad (1)$$

where $\mathbf{M}$ is the source-receptor dilution matrix, $\mathbf{o}_a$ is the vector of satellite observations, $\mathbf{R}$ is the covariance matrix for the errors in the satellite retrievals and the transport model, $\mathbf{B}$ is the error covariance matrix for the *a priori* source, and $\mathbf{e}_{ap}$ is the mean of the *a priori* probability distribution of emissions. The cost function is computed many times in iterating to find the best fit emission profile, $\mathbf{e}$, and hence it is beneficial to compute it in an efficient way. In the original Pelley et al. [5] code, computing the cost function involved summing over both the satellite observations and the source components each time. There are generally many more observations than source components and, for this reason, the summation over observations is parallelised in the Pelley et al. [5] code. In addition, Pelley et al. [5] exploit the fact that the transport matrix $\mathbf{M}$ is, in the main, sparse, performing matrix operations in an efficient way. Despite this, for large numbers of observations relative to the number of source components, summation over the observations at each iteration is both expensive and unnecessary, since the observations are unchanged during the process of iterating to the solution. The first modification of the Pelley et al. [5] code is to pre-calculate the summations over the observations and store these for use over many cost function evaluations.

Equation (1) can be expressed as a quadratic function of $\mathbf{e}$,

$$J(\mathbf{e}) = \mathbf{e}^T \left(\mathbf{M}^T\mathbf{R}^{-1}\mathbf{M} + \mathbf{B}^{-1}\right)\mathbf{e} - 2\left(\mathbf{o}_a^T\mathbf{R}^{-1}\mathbf{M} + \mathbf{e}_{ap}^T\mathbf{B}^{-1}\right)\mathbf{e} + \mathbf{o}_a^T\mathbf{R}^{-1}\mathbf{o}_a + \mathbf{e}_{ap}^T\mathbf{B}^{-1}\mathbf{e}_{ap}. \quad (2)$$

The quadratic, linear and constant coefficients, namely

$$\begin{aligned} \mathbf{A}^{-1} &= \mathbf{M}^T\mathbf{R}^{-1}\mathbf{M} + \mathbf{B}^{-1}, \\ \mathbf{c} &= -2\left(\mathbf{o}_a^T\mathbf{R}^{-1}\mathbf{M} + \mathbf{e}_{ap}^T\mathbf{B}^{-1}\right), \\ d &= \mathbf{o}_a^T\mathbf{R}^{-1}\mathbf{o}_a + \mathbf{e}_{ap}^T\mathbf{B}^{-1}\mathbf{e}_{ap}, \end{aligned}$$

involve only summations over observations and are pre-calculated. Here $\mathbf{A}$ is the analysis (i.e. *a posteriori*) error covariance matrix, at least to the extent that we can ignore the truncation of the Gaussian distributions. With these coefficients known, computation of the cost function at each iteration requires only a summation over the source components. For a large number of observations (relative to the number of source components), this reduces the cost of finding the solution. However, although some sparse matrix calculations are used in pre-calculating the cost function coefficients, the potential benefits of the sparse matrix representation are much reduced in the subsequent use of these coefficients to evaluate the cost function (for example, one cannot in general assume that $\mathbf{A}^{-1} = \mathbf{M}^T\mathbf{R}^{-1}\mathbf{M} + \mathbf{B}^{-1}$ is sparse, even if $\mathbf{M}$ is sparse). Hence we have not used

sparse matrix representations in these subsequent evaluations, with the cost function evaluated using full explicit matrix forms at each iteration. For relatively small numbers of observations, therefore, this pre-calculation does not necessarily result in a speed up of the code (in fact, it can result in a slow down). However, reducing the cost of the most expensive inversions is considered most important, even if it does result in an increase in the cost of inexpensive inversions.

3.1 Grímsvötn 2011

3.1.1 Ash-only observations

Figure 13 shows the *a posteriori* source determined using ash-only observations until the dates given and using the restructured inversion code which pre-calculates the coefficients of the cost function. Encouragingly, in the initial stages when relatively few ash satellite observations are used, there is very good agreement with the source determined using the original Pelley et al. [5] code (cf. figure 3). However, as the process continues, with more and more ash observations from later times being included in the inversion, differences appear between the best fit source determined using the restructured code and that obtained using the original Pelley et al. [5] code. These differences are likely to be due to incomplete convergence of the simulated annealing solver as discussed in section 2.3 and appendix A. Indeed, the value of the cost function ($J(\mathbf{e})$) for the solution ($\mathbf{e}$) obtained using the restructured code differs from that for the solution determined using the original Pelley et al. [5] code (see table 1 below).

Figure 14 shows the modelled plume between 23:00 UTC on 22/05/2011 and 00:00 UTC on 23/05/2011 using the *a posteriori* emission profiles in figure 13, together with the ash observations from the satellite retrieval valid at the same time. The predicted plumes are similar to those obtained with the original Pelley et al. [5] code (cf. figure 4) but, as was seen for the best fit emissions, whilst they look identical in the initial stages, noticeable differences do appear as more and more observations from later times are included in the inversion process.

Table 1 shows the run time of the restructured code using all available ash-only satellite observations until 00:00 UTC on 31/05/2011. Note the run times given are for the inversion calculation only and do not include the runs of the NAME model which are needed to calculate $\mathbf{M}$. In this case, the restructured code with the pre-calculation of the coefficients of the cost function is less efficient than the original Pelley et al. [5] code, although not greatly so.

3.1.2 Ash and clear sky observations

Figure 15 shows the *a posteriori* source determined using both ash and clear sky satellite observations until the dates given and using the restructured inversion code which pre-calculates the cost function coefficients. The determined emissions agree well with those obtained using the original Pelley et al. [5] code (cf. figure 5). The value of the cost function for the best fit emissions is also similar to that obtained using the original Pelley et al. [5] code (see table 2 below).

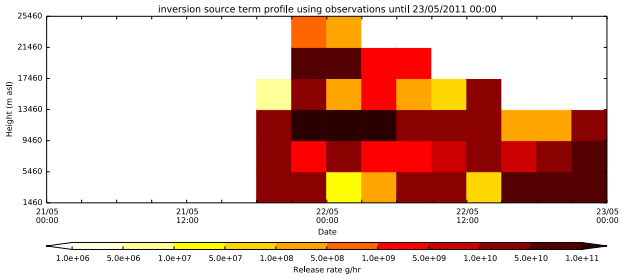

(a) emissions using satellite retrievals up to 00:00 UTC 23/05/2011

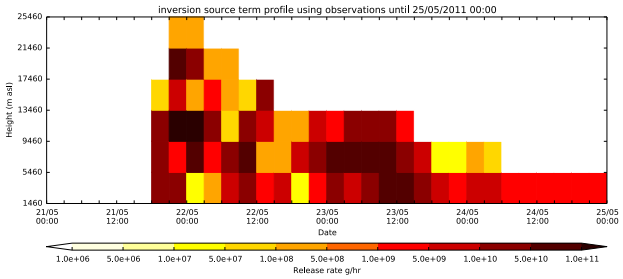

(b) emissions using satellite retrievals up to 00:00 UTC 25/05/2011

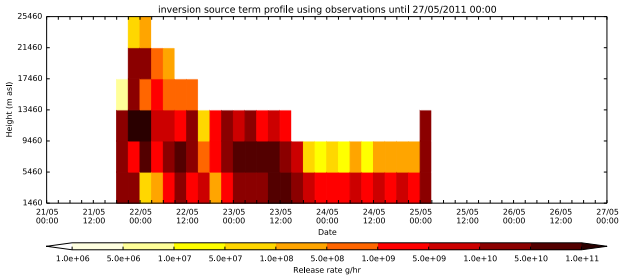

(c) emissions using satellite retrievals up to 00:00 UTC 27/05/2011

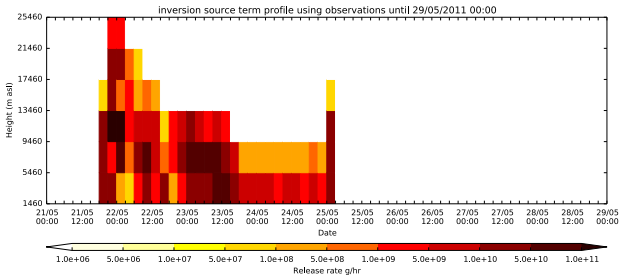

(d) emissions using satellite retrievals up to 00:00 UTC 29/05/2011

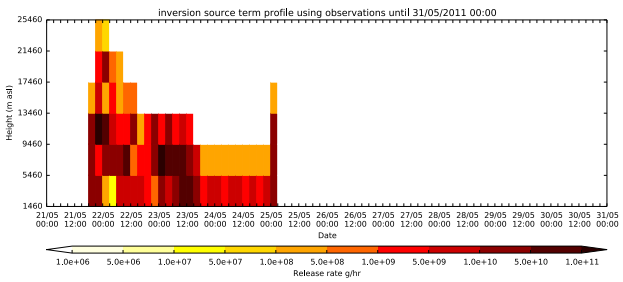

(e) emissions using satellite retrievals up to 00:00 UTC 31/05/2011

Figure 13: The best fit emission profile for the eruption of Grímsvötn using ash-only satellite observations and inversion code with pre-calculation of the cost function coefficients. (Note the different scales used along the time axis.)

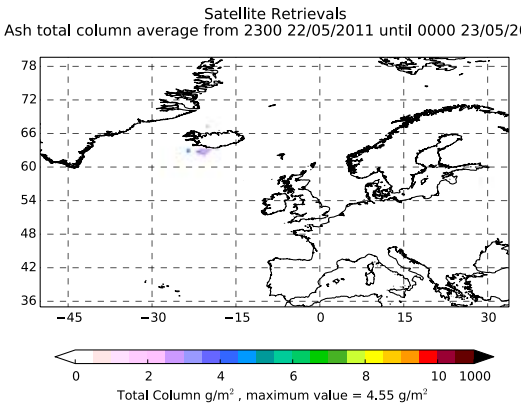

(a) ash-only satellite retrievals

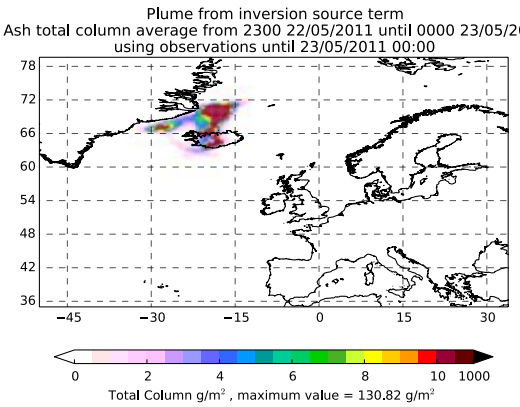

(b) plume using retrievals up to 00:00 UTC 23/05/2011

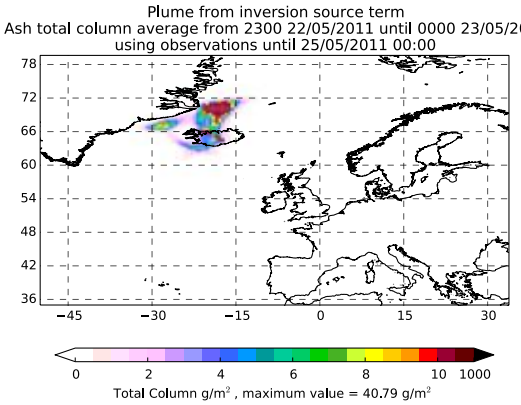

(c) plume using retrievals up to 00:00 UTC 25/05/2011

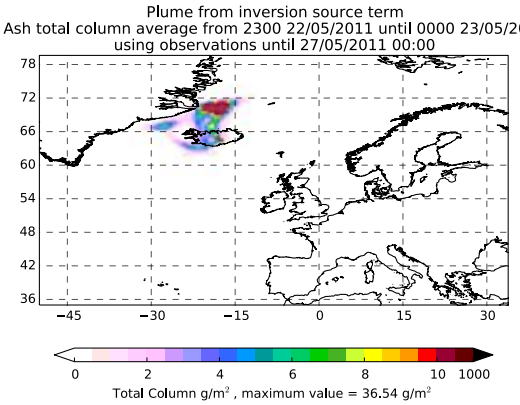

(d) plume using retrievals up to 00:00 UTC 27/05/2011

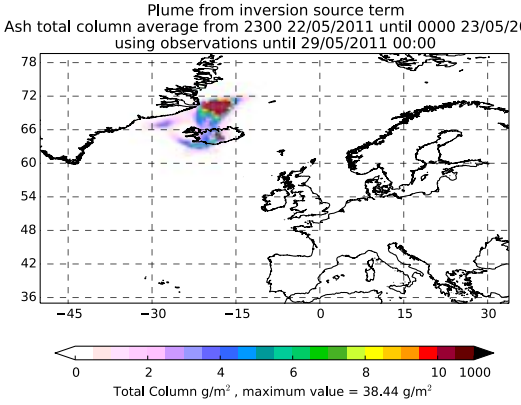

(e) plume using retrievals up to 00:00 UTC 29/05/2011

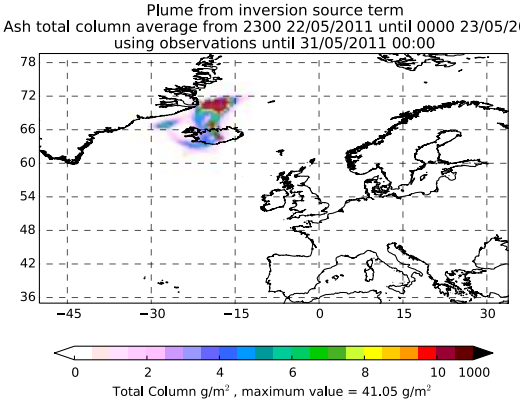

(f) plume using retrievals up to 00:00 UTC 31/05/2011

Figure 14: The Grímsvötn plume averaged between 23:00 UTC on 22/05/2011 and 00:00 UTC on 23/05/2011: (a) as observed by satellite (ash only); and (b-f) as predicted by NAME with emissions determined using ash-only satellite observations and inversion code with pre-calculation of the cost function coefficients.

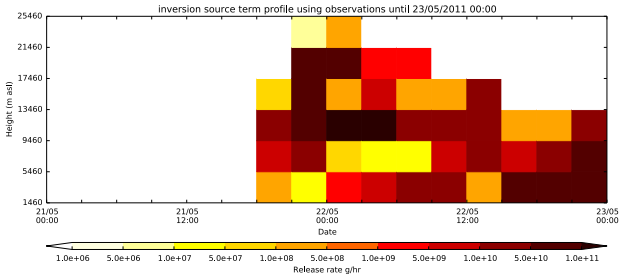

(a) emissions using satellite retrievals up to 00:00 UTC 23/05/2011

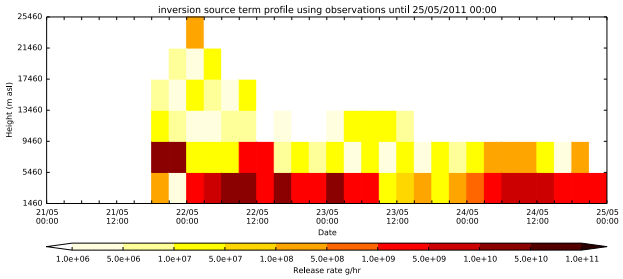

(b) emissions using satellite retrievals up to 00:00 UTC 25/05/2011

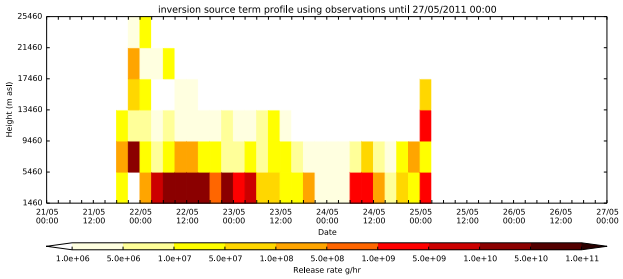

(c) emissions using satellite retrievals up to 00:00 UTC 27/05/2011

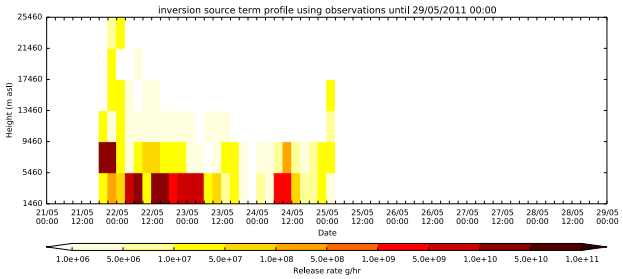

(d) emissions using satellite retrievals up to 00:00 UTC 29/05/2011

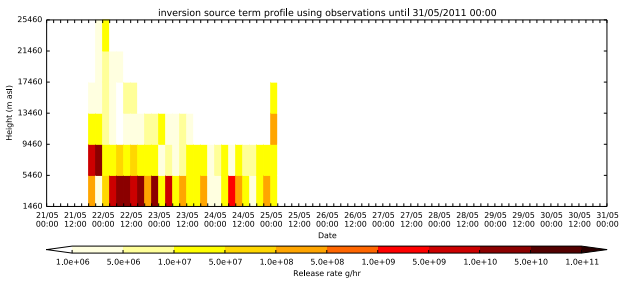

(e) emissions using satellite retrievals up to 00:00 UTC 31/05/2011

Figure 15: The best fit emission profile for the eruption of Grímsvötn using both ash and clear sky satellite observations and inversion code with pre-calculation of the cost function coefficients. (Note the different scales used along the time axis.)

Code modifications	Run-time	Normalised cost function
Pelley et al. [5] code	3 min 46.626 sec	0.05905
Pre-calculating cost function coefficients	4 min 9.466 sec	0.05805
Lawson and Hanson [3] NNLS solver	0 min 11.474 sec	0.05753
Lawson and Hanson [3] NNLS solver with *a priori* cross correlations	0 min 12.860 sec	Not comparable

Table 1: The inversion run time and the normalised cost function (normalised with number of observations) for the determined solution using 3293 ash-only satellite observations until 00:00 UTC on 31/05/2011 from the 2011 Grímsvötn eruption.

Figure 16 shows the modelled plume between 23:00 UTC on 22/05/2011 and 00:00 UTC on 23/05/2011 using the *a posteriori* source in figure 15, together with the satellite observations valid at the same time, for comparison. Again there is good agreement with the results from the Pelley et al. [5] code (cf. figure 6).

Table 2 assesses the run time of the restructured inversion code using all satellite observations (both ash and clear skies) from the 2011 eruption of Grímsvötn until 00:00 UTC on 31/05/2011. Pre-calculating the cost function coefficients has much benefit here with the relatively large number of observations. An inversion calculation which took about an hour and twenty minutes using the original Pelley et al. [5] code can be completed in less than five minutes, giving a speed up of about a factor of 18.

Code modifications	Run-time	Normalised cost function
Pelley et al. [5] code	80 min 34.601 sec	0.003134
Pre-calculating cost function coefficients	4 min 23.971 sec	0.003137
Lawson and Hanson [3] NNLS solver	1 min 1.390 sec	0.003112
Lawson and Hanson [3] NNLS solver with *a priori* cross correlations	1 min 5.287 sec	Not comparable

Table 2: The inversion run time and the normalised cost function (normalised with number of observations) for the determined solution using 88791 satellite observations (both ash and clear skies) until 00:00 UTC on 31/05/2011 from the 2011 Grímsvötn eruption.

3.2 Eyjafjallajökull 2010

3.2.1 Ash-only observations

Figure 17 shows the *a posteriori* source determined using ash-only observations until the dates given and using the restructured inversion code which pre-calculates the coefficients of the cost

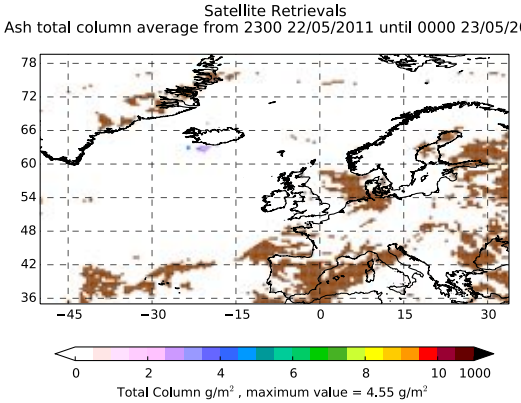

(a) ash and clear sky satellite retrievals

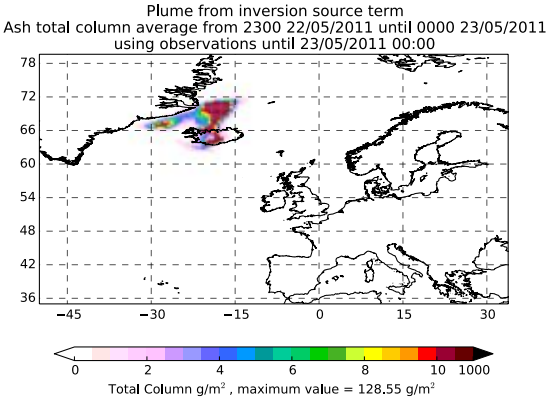

(b) plume using retrievals up to 00:00 UTC 23/05/2011

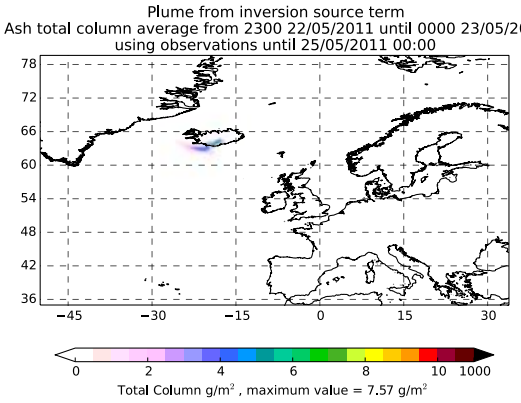

(c) plume using retrievals up to 00:00 UTC 25/05/2011

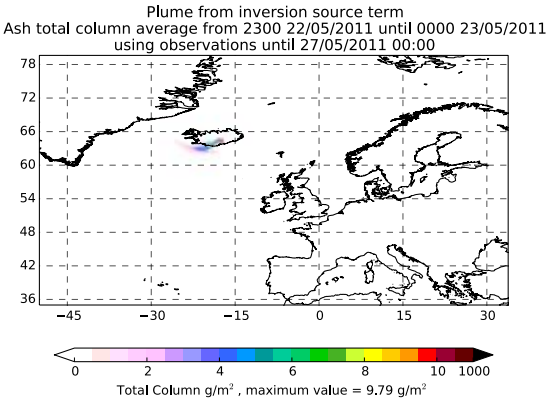

(d) plume using retrievals up to 00:00 UTC 27/05/2011

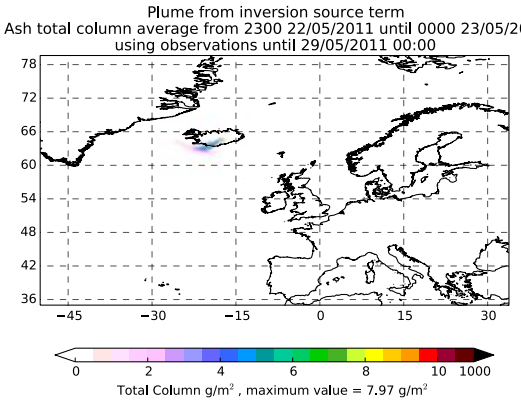

(e) plume using retrievals up to 00:00 UTC 29/05/2011

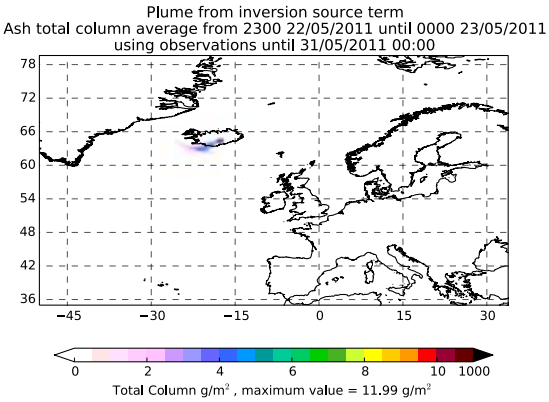

(f) plume using retrievals up to 00:00 UTC 31/05/2011

Figure 16: The Grímsvötn plume averaged between 23:00 UTC on 22/05/2011 and 00:00 UTC on 23/05/2011: (a) as observed by satellite (ash and clear skies, with clear skies shown in brown); and (b-f) as predicted by NAME with emissions determined using both ash and clear sky satellite observations and inversion code with pre-calculation of the cost function coefficients.

function. The source is similar to that determined using the original Pelley et al. [5] code (cf. figure 9), although there are some differences which may be due to incomplete convergence of the simulated annealing solver. As in the Grímsvötn case, the value of the cost function ($J(\mathbf{e})$) for the best fit emissions ($\mathbf{e}$) obtained using the restructured code differs from that determined using the original Pelley et al. [5] code (see table 3 below).

Figure 18 shows the modelled plume between 17:00 UTC and 18:00 UTC on 06/05/2010 using the *a posteriori* emission profiles in figure 17, together with the ash observations from the satellite retrieval valid at the same time. The predicted plumes are very similar to those obtained with the original Pelley et al. [5] code (cf. figure 10) but some subtle differences do exist (see, for example, the quoted maximum total column values).

Table 3 shows the run time of the restructured code using all available ash-only satellite observations until 00:00 UTC on 29/05/2010. In this case the restructured code, pre-calculating the coefficients of the cost function, is less efficient than the original Pelley et al. [5] code, taking over 3 times as long to perform the inversion.

Code modifications	Run-time	Normalised cost function
Pelley et al. [5] code	3 hr 20 min 54.451 sec	0.07551
Pre-calculating cost function coefficients	10 hr 20 min 50.69 sec	0.07538
Lawson and Hanson [3] NNLS solver	3 min 6.653 sec	0.06437
Lawson and Hanson [3] NNLS solver with *a priori* cross correlations	5 min 4.900 sec	Not comparable

Table 3: The inversion run time and the normalised cost function (normalised with number of observations) for the determined solution using 40047 ash-only satellite observations until 00:00 UTC on 29/05/2010 from the 2010 Eyjafjallajökull eruption.

3.2.2 Ash and clear sky observations

Figure 19 shows the *a posteriori* source determined using both ash and clear sky satellite observations until the dates given and using the restructured inversion code which pre-calculates the cost function coefficients. The determined emissions agree well with those obtained with the original Pelley et al. [5] code (cf. figure 11), although there are some minor differences. The value of the cost function for the best fit emissions is also similar to, but slightly different from, that obtained using the original Pelley et al. [5] code (see table 4 below).

Figure 20 shows the modelled plume between 17:00 UTC and 18:00 UTC on 06/05/2010 using the *a posteriori* source in figure 19, together with the satellite observations valid at the same time, for comparison. Again there is good agreement with the results from the Pelley et al. [5] code (cf. figure 12), although there are some significant differences using data up to 21/05/2010, presumably

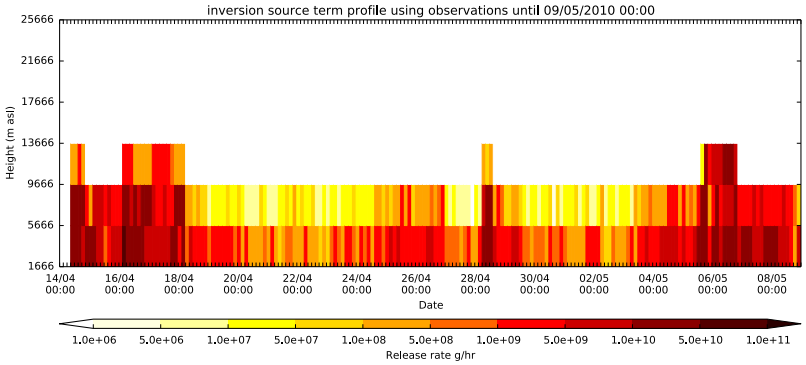

(a) emissions using satellite retrievals up to 00:00 UTC 09/05/2010

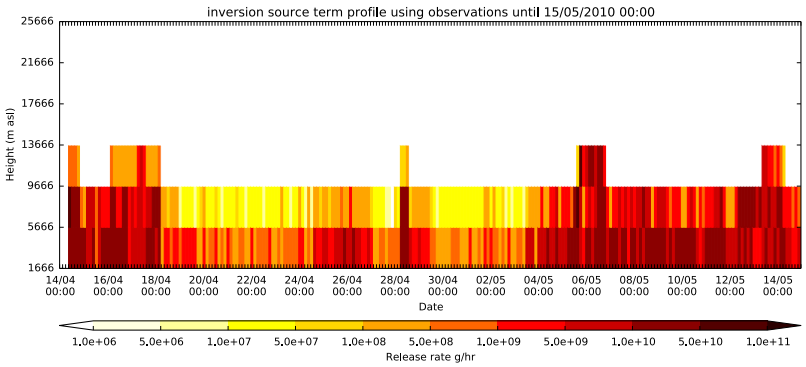

(b) emissions using satellite retrievals up to 00:00 UTC 15/05/2010

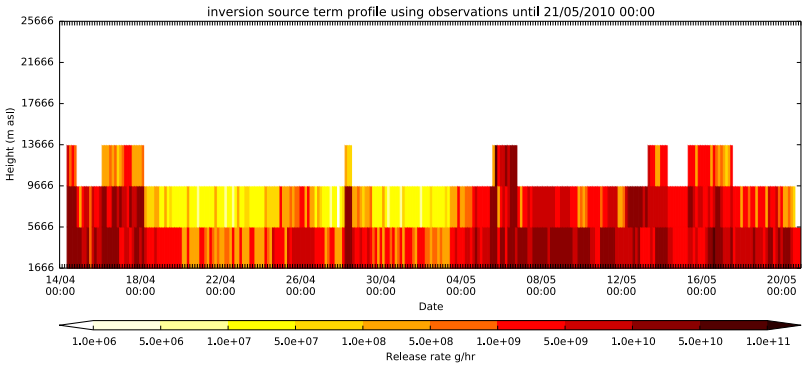

(c) emissions using satellite retrievals up to 00:00 UTC 21/05/2010

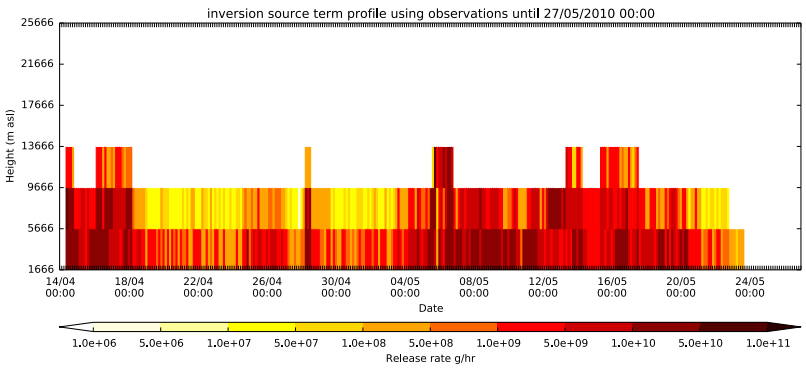

(d) emissions using satellite retrievals up to 00:00 UTC 27/05/2010

Figure 17: The best fit emission profile for the eruption of Eyjafjallajökull using ash-only satellite observations and inversion code with pre-calculation of the cost function coefficients. (Note the different scales used along the time axis.)

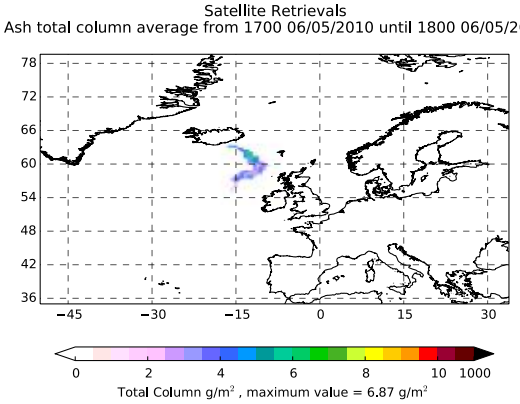

(a) ash-only satellite retrievals

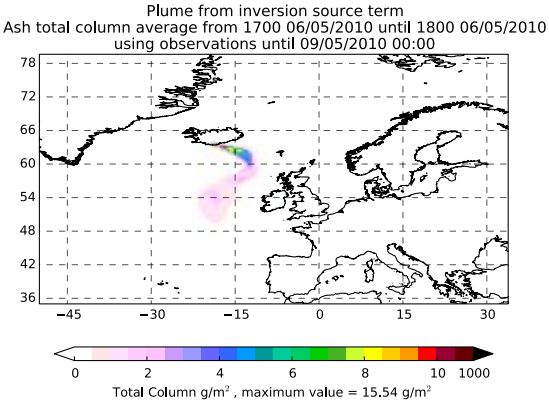

(b) plume using retrievals up to 00:00 UTC 09/05/2010

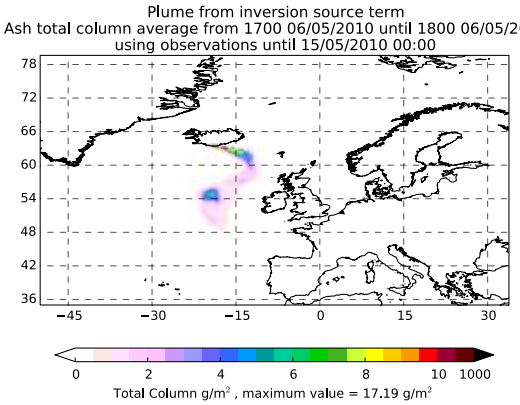

(c) plume using retrievals up to 00:00 UTC 15/05/2010

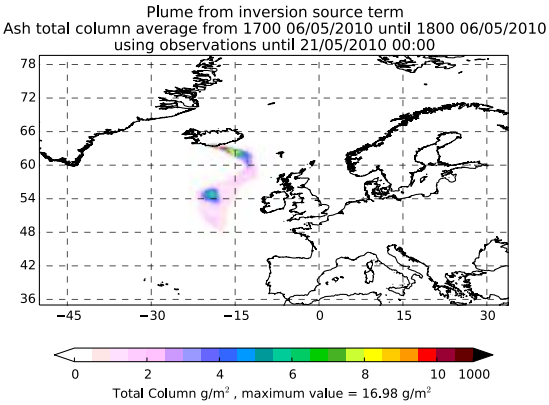

(d) plume using retrievals up to 00:00 UTC 21/05/2010

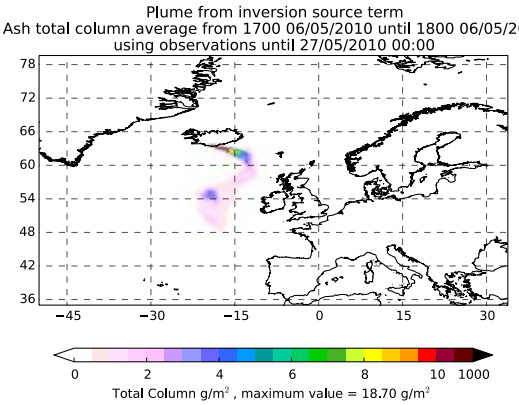

(e) plume using retrievals up to 00:00 UTC 27/05/2010

Figure 18: The Eyjafjallajökull plume averaged between 17:00 UTC and 18:00 UTC on 06/05/2010: (a) as observed by satellite (ash only); and (b-e) as predicted by NAME with emissions determined using ash-only satellite observations and inversion code with pre-calculation of the cost function coefficients.

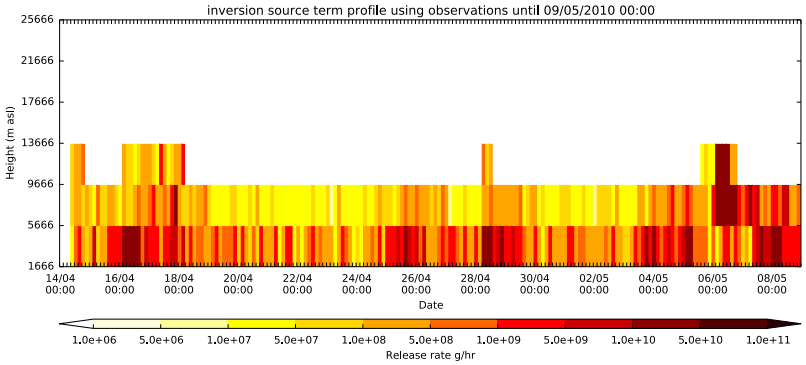

(a) emissions using satellite retrievals up to 00:00 UTC 09/05/2010

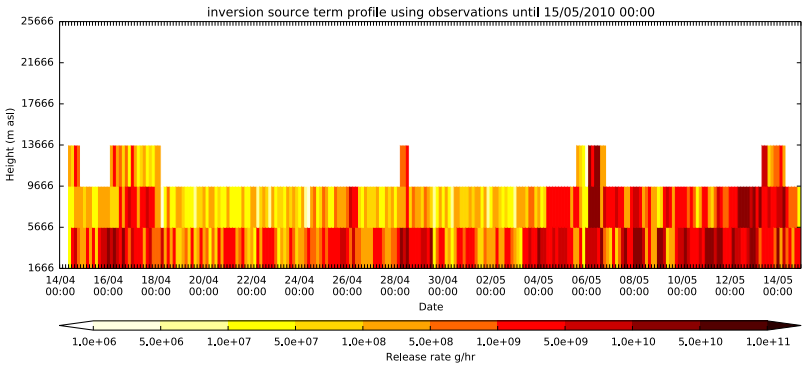

(b) emissions using satellite retrievals up to 00:00 UTC 15/05/2010

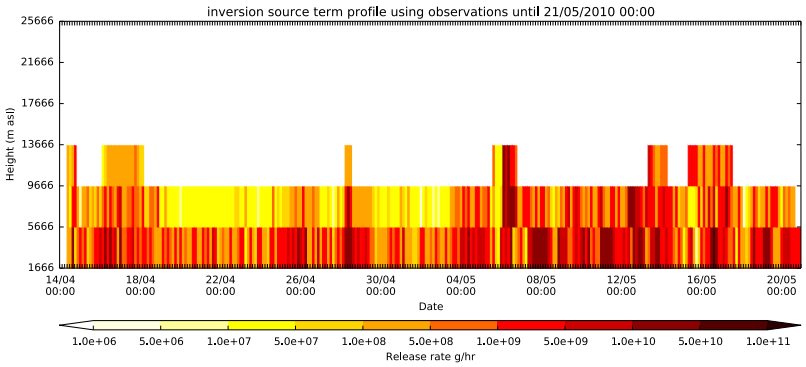

(c) emissions using satellite retrievals up to 00:00 UTC 21/05/2010

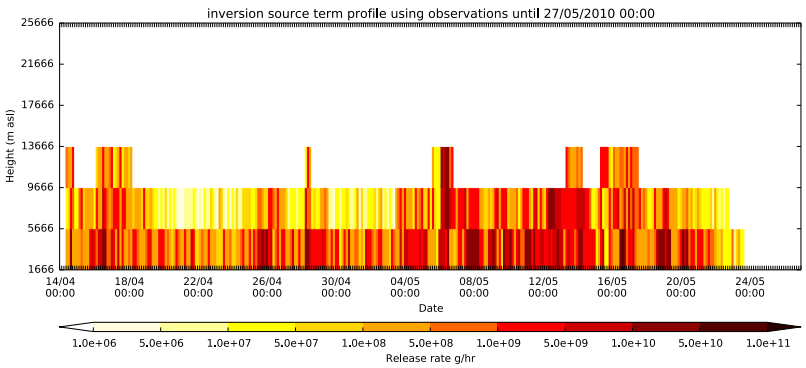

(d) emissions using satellite retrievals up to 00:00 UTC 27/05/2010

Figure 19: The best fit emission profile for the eruption of Eyjafjallajökull using both ash and clear sky satellite observations and inversion code with pre-calculation of the cost function coefficients. (Note the different scales used along the time axis.)

associated with the lack of complete convergence in the simulated annealing.

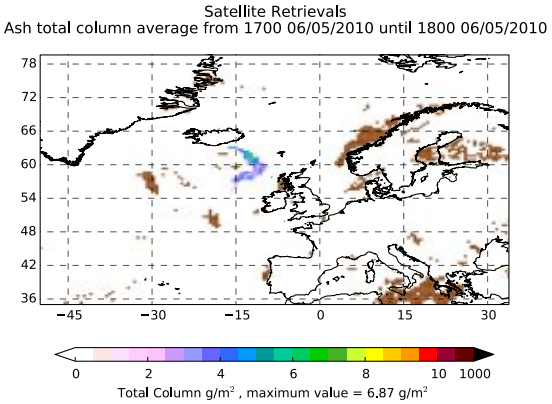

(a) ash and clear sky satellite retrievals

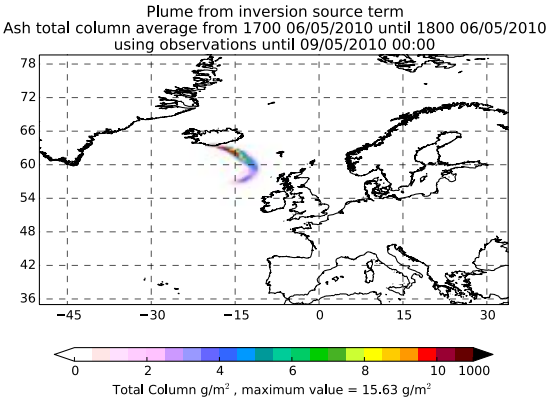

(b) plume using retrievals up to 00:00 UTC 09/05/2010

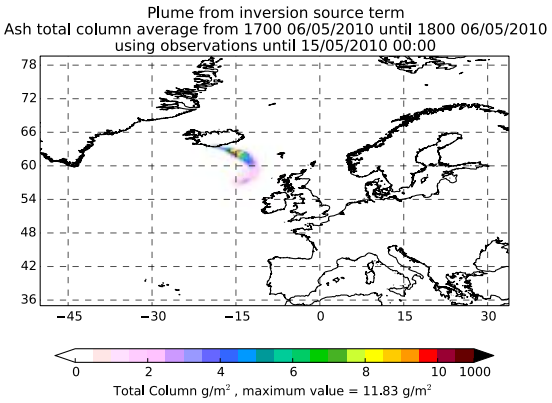

(c) plume using retrievals up to 00:00 UTC 15/05/2010

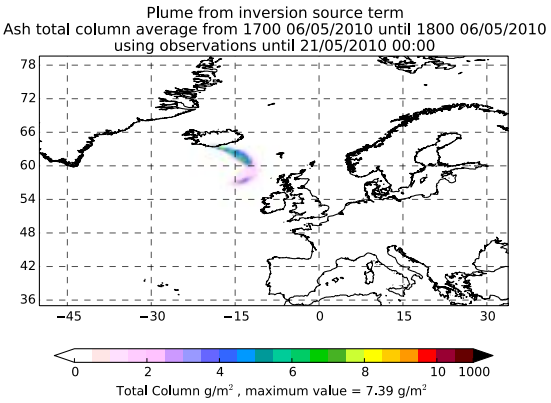

(d) plume using retrievals up to 00:00 UTC 21/05/2010

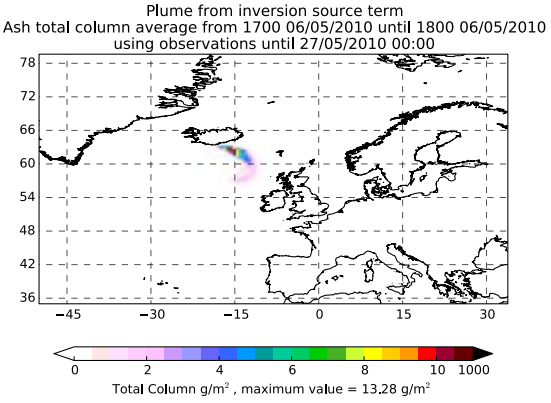

(e) plume using retrievals up to 00:00 UTC 27/05/2010

Figure 20: The Eyjafjallajökull plume averaged between 17:00 UTC and 18:00 UTC on 06/05/2010: (a) as observed by satellite (ash and clear skies, with clear skies shown in brown); and (b-e) as predicted by NAME with emissions determined using both ash and clear sky satellite observations and inversion code with pre-calculation of the cost function coefficients.

Table 4 assesses the run time of the restructured inversion code using all satellite observations (both ash and clear skies) from the 2010 eruption of Eyjafjallajökull until 00:00 UTC on 29/05/2010.

As was seen for the 2011 Grímsvötn example, pre-calculating the cost function coefficients has much benefit with the relatively large number of observations used when clear skies are included. An inversion calculation of the 2010 Eyjafjallajökull eruption which took over 27 hours using the original Pelley et al. [5] code can be completed in just over 8 hours, giving a speed up of about a factor of 3. This is a smaller speed up than seen for the 2011 Grímsvötn example. This may be because the original approach, which uses sparse matrices, obtains more benefit from sparseness for the Eyjafjallajökull eruption than for the Grímsvötn eruption.

Code modifications	Run-time	Normalised cost function
Pelley et al. [5] code	27 hr 35 min 54.234 sec	0.005237
Pre-calculating cost function coefficients	8 hr 13 min 29.097 sec	0.005278
Lawson and Hanson [3] NNLS solver	10 min 49.212 sec	0.004820
Lawson and Hanson [3] NNLS solver with *a priori* cross correlations	13 min 10.664 sec	Not comparable

Table 4: The inversion run time and the normalised cost function (normalised with number of observations) for the determined solution using 689492 satellite observations (both ash and clear sky) until 00:00 UTC on 29/05/2010 from the 2010 Eyjafjallajökull eruption.

4 Using the Lawson and Hanson method for solving the non-negative least squares (NNLS) problem

The simulated annealing solver benefits from being able to find the true minimum rather than getting stuck in the region around a local minimum. The cost function here is, however, quadratic and therefore only has one local minimum (which is also the global minimum). This minimum may lie in a non-feasible region (for example, negative emissions here) but one can deduce that, even if this is the case, there is a single point which takes a local minimum value within the feasible regime. This benefit of the simulated annealing solver is not, therefore, exploited here. Furthermore, as was seen in section 2.3, the simulated annealing converges slowly, possibly due to the restriction to positive emissions. In addition, other solvers may be much faster, particularly since we have a simple minimisation problem.

The method developed by Lawson and Hanson [3] for minimising the Euclidean norm of

$$\mathbf{Pe} - \mathbf{q}, \tag{3}$$

subject to the constraint that $\mathbf{e} \geq \mathbf{0}$, is coded in Fortran and available from http://www.netlib.org. This could be used directly if we were simply finding a least squares fit to the satellite retrievals. However to use the NNLS algorithm for our problem, we need to translate the cost function in equation (2) into the form of the Euclidean norm of equation (3). The Euclidean norm of $\mathbf{Pe}-\mathbf{q}$ can be expressed as

$$||\mathbf{Pe} - \mathbf{q}||_2 \; = \; (\mathbf{Pe} - \mathbf{q})^T (\mathbf{Pe} - \mathbf{q}) \, . \tag{4}$$

Expanding equation (4) and comparing with the cost function in equation (2), we deduce that, in order for $||\mathbf{Pe} - \mathbf{q}||_2$ to match our cost function to within an additive constant, we require

$$\mathbf{P}^T\mathbf{P} \;=\; \mathbf{A}^{-1} \;=\; \mathbf{M}^T\mathbf{R}^{-1}\mathbf{M} + \mathbf{B}^{-1}, \tag{5}$$

$$\mathbf{P}^T\mathbf{q} \;=\; -\frac{1}{2}\mathbf{c}^T \;=\; \left(\mathbf{o}_a^T\mathbf{R}^{-1}\mathbf{M} + \mathbf{e}_{ap}^T\mathbf{B}^{-1}\right)^T. \tag{6}$$

$\mathbf{P}$ can be found from equation (5) by performing a Cholesky decomposition on $\mathbf{A}^{-1}$. Note that $\mathbf{P}$ is an upper triangular matrix. Equation (6) can then be solved easily by iteration to find $\mathbf{q}$ (exploiting the fact that $\mathbf{P}^T$ is a lower triangular matrix). Here we make use of the DTRTRS routine for solving triangular systems of the form found in equation (6) and which comes as part of the linear algebra package LAPACK [1]. With $\mathbf{P}$ and $\mathbf{q}$ determined, the minimum, subject to the non-negative constraint $\mathbf{e} \geq \mathbf{0}$, can now be found using the NNLS algorithm.

4.1 Grímsvötn 2011

4.1.1 Ash-only observations

Figure 21 shows the *a posteriori* source determined using ash-only observations until the dates given and using the inversion code with the Lawson and Hanson NNLS solver [3]. The permittance of zero sources by the Lawson and Hanson NNLS solver results in the best fit emission profile having, at certain times, zero emissions at a particular height but non-zero emissions at heights both above and below. This gives the emission profile a noisy appearance which may not actually be unphysical if the eruption has varied over the source resolution time scale of three hours. Comparing figure 21 with the emissions obtained using ash-only satellite observations and simulated annealing (figures 3 and 13) one sees that, despite noticeable differences (in particular, some zero emissions with the Lawson and Hanson NNLS solver and strictly non-zero emissions with simulated annealing), the main ash emissions occur at the same heights and times.

Figure 22 shows the modelled plume between 23:00 UTC on 22/05/2011 and 00:00 UTC on 23/05/2011 using the *a posteriori* emission profiles in figure 21, together with the ash observations from the satellite retrieval valid at the same time. Despite some subtle differences, the modelled ash plumes using the Lawson and Hanson NNLS solver are similar to those obtained using simulated annealing (cf. figures 4 and 14). Table 1 compares the value of the cost function for the best fit emission profile obtained using different solvers and observations until 00:00 UTC on 31/05/2011. The Lawson and Hanson NNLS solver finds a solution with a lower value of the cost function than the solutions obtained using simulated annealing. This further supports our opinion (see section 2.3) that the simulated annealing technique gets close, but not very close, to the true solution. We also see from table 1 that the Lawson and Hanson NNLS solver is much faster than simulated annealing, taking just over 11 seconds to perform an inversion of the Grímsvötn 2011 eruption (in comparison to around 4 minutes for the simulated annealing technique). This equates to a speed up of about a factor of 20.

We note that both figures 21 and 22 show less change as the data cut-off time increases than was the case for the annealing solutions (cf. figures 3, 4, 13 and 14). This probably reflects the better convergence of the NNLS method and suggests that some of the changes seen with the annealing method as the cut-off time increases may well be due to the lack of convergence rather than due to the information added by the later observations. The same behaviour is found using ash and clear sky satellite data and for the Eyjafjallajökull eruption (see below).

4.1.2 Ash and clear sky observations

Figure 23 shows the *a posteriori* source determined using both ash and clear sky satellite observations until the dates given and using the inversion code with the Lawson and Hanson NNLS solver [3]. Comparing figure 23 with the emission profiles obtained using both ash and clear sky satellite observations and simulated annealing (figures 5 and 15) one sees again that, although the main

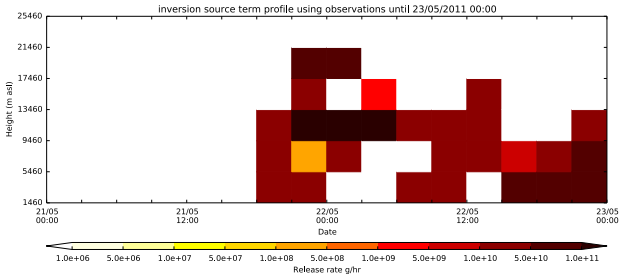

(a) emissions using satellite retrievals up to 00:00 UTC 23/05/2011

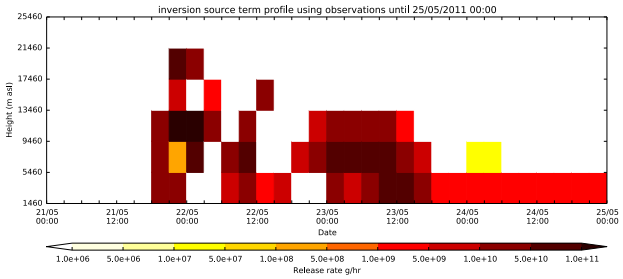

(b) emissions using satellite retrievals up to 00:00 UTC 25/05/2011

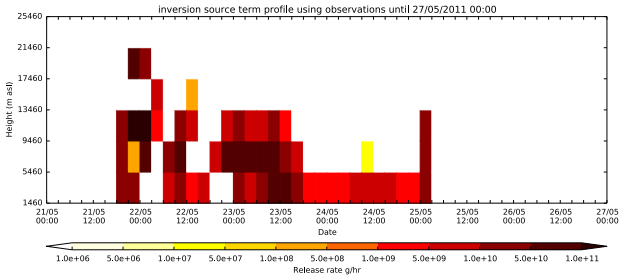

(c) emissions using satellite retrievals up to 00:00 UTC 27/05/2011

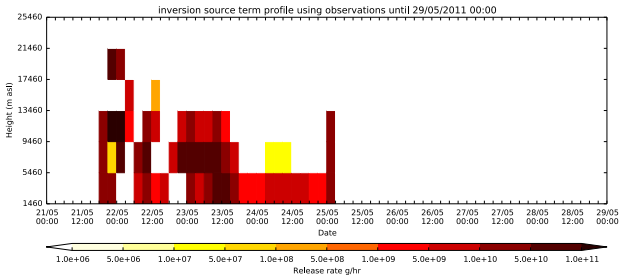

(d) emissions using satellite retrievals up to 00:00 UTC 29/05/2011

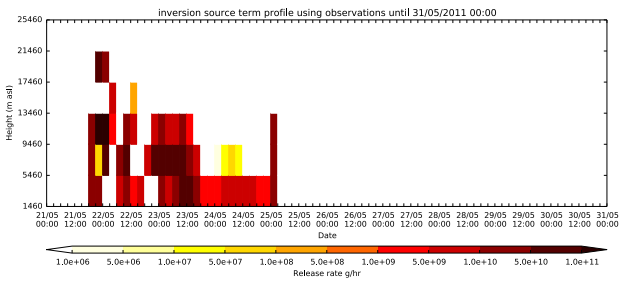

(e) emissions using satellite retrievals up to 00:00 UTC 31/05/2011

Figure 21: The best fit emission profile for the eruption of Grímsvötn using ash-only satellite observations and inversion code with the NNLS solver. (Note the different scales used along the time axis.)

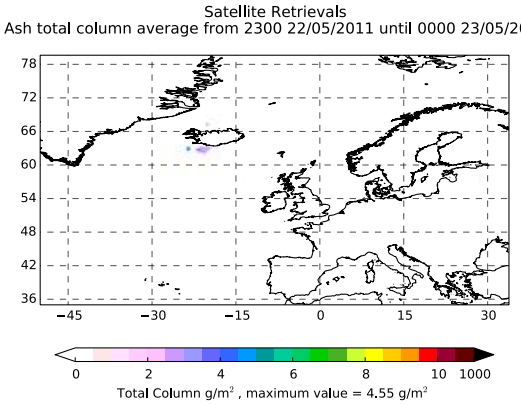

(a) ash-only satellite retrievals

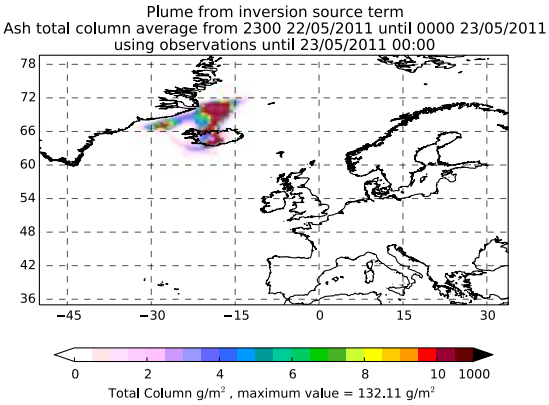

(b) plume using retrievals up to 00:00 UTC 23/05/2011

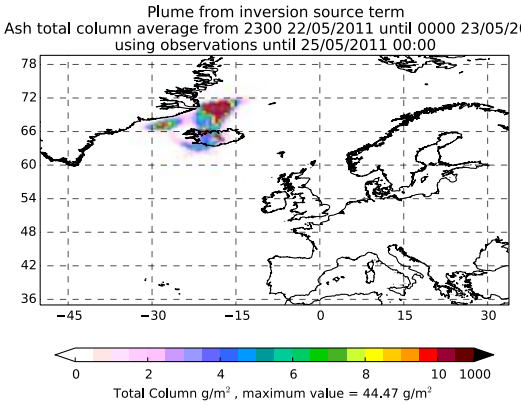

(c) plume using retrievals up to 00:00 UTC 25/05/2011

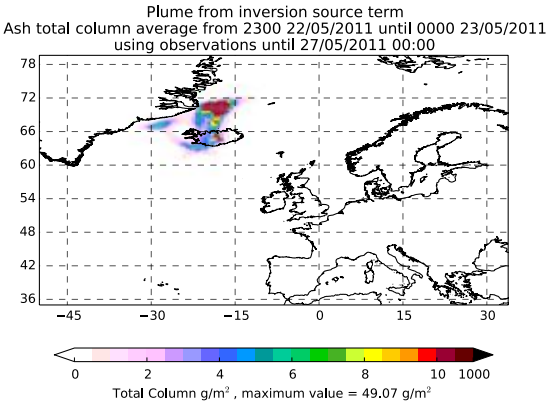

(d) plume using retrievals up to 00:00 UTC 27/05/2011

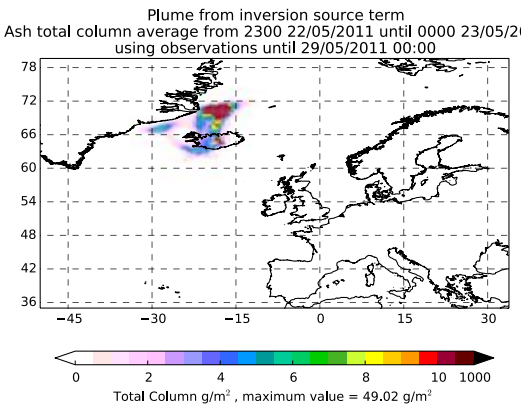

(e) plume using retrievals up to 00:00 UTC 29/05/2011

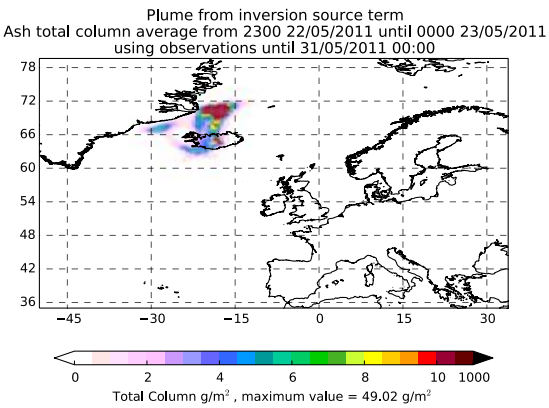

(f) plume using retrievals up to 00:00 UTC 31/05/2011

Figure 22: The Grímsvötn plume averaged between 23:00 UTC on 22/05/2011 and 00:00 UTC on 23/05/2011: (a) as observed by satellite (ash only); and (b-f) as predicted by NAME with emissions determined using ash-only satellite observations and inversion code with the NNLS solver.

ash emissions obtained using the Lawson and Hanson solver occur at the same heights and times as those obtained using simulated annealing, there are many zero emission components in the Lawson and Hanson solution.

Figure 24 shows the modelled plume between 23:00 UTC on 22/05/2011 and 00:00 UTC on 23/05/2011 using the *a posteriori* source in figure 23, together with the satellite observations valid at the same time, for comparison. There is good agreement with the simulated annealing results (cf. figures 6 and 16). As seen with the ash-only observations, the value of the cost function for the solution obtained using the Lawson and Hanson solver is less than the value obtained using simulated annealing (table 2), indicating that the simulated annealing technique isn't reaching the actual minimum. Table 2 also assesses the run time of the Lawson and Hanson method, giving a speed up of about a factor of 4, in addition to the large speed up seen when the cost function coefficients were pre-calculated.

4.2 Eyjafjallajökull 2010

4.2.1 Ash-only observations

Figure 25 shows the *a posteriori* source determined for the Eyjafjallajökull eruption in 2010 using ash-only observations until the dates given and using the inversion code with the Lawson and Hanson NNLS solver [3]. As in the case of the Grímsvötn 2011 example, the permittance of zero sources by the Lawson and Hanson NNLS solver results in the solution having zero emissions at particular heights and times, but the main ash emissions occur at the same heights and times as in the *a posteriori* source obtained using simulated annealing (cf. figures 9 and 17).

Figure 26 shows the modelled plume between 17:00 UTC and 18:00 UTC on 06/05/2010 using the *a posteriori* source in figure 25, together with the ash observations from the satellite retrieval valid at the same time. The ash plumes obtained using the Lawson and Hanson NNLS solver are similar to those obtained using simulated annealing (cf. figures 10 and 18), although the concentrations are somewhat larger with NNLS. The differences seen are perhaps not surprising given the substantial cost function differences (see table 3). Table 3 compares the value of the cost function for the solutions obtained using different solvers and observations until 00:00 UTC on 29/05/2010. As before, the Lawson and Hanson NNLS solver finds a solution with a lower value of the cost function than the solutions obtained using simulated annealing. Furthermore the Lawson and Hanson NNLS solver is again much faster than simulated annealing, taking just over 3 minutes to perform an inversion of the Eyjafjallajökull eruption (in comparison to over 3 hours for the original Pelley et al. [5] code and over 10 hours for the restructured code with pre-calculation of cost functions). This equates to a speed up of about a factor of 65 on the original code [5].

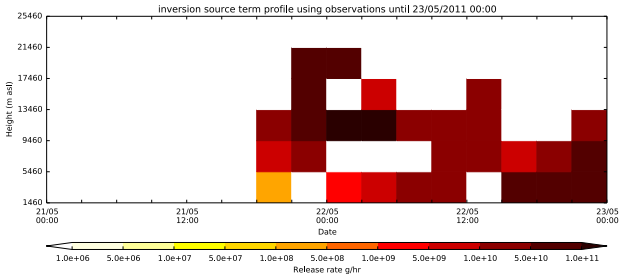

(a) emissions using satellite retrievals up to 00:00 UTC 23/05/2011

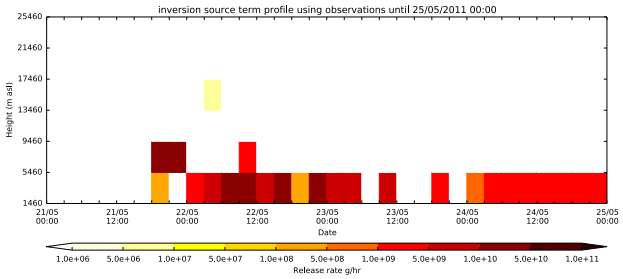

(b) emissions using satellite retrievals up to 00:00 UTC 25/05/2011

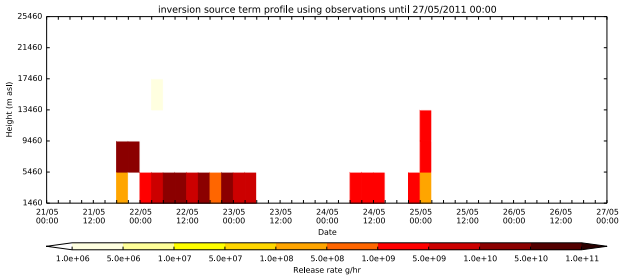

(c) emissions using satellite retrievals up to 00:00 UTC 27/05/2011

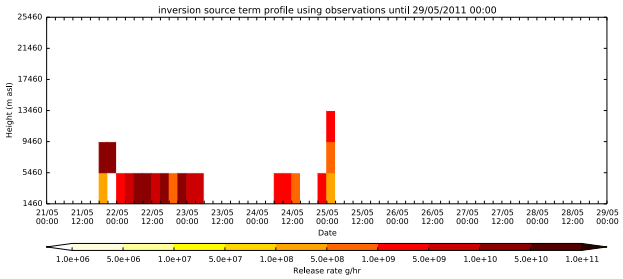

(d) emissions using satellite retrievals up to 00:00 UTC 29/05/2011

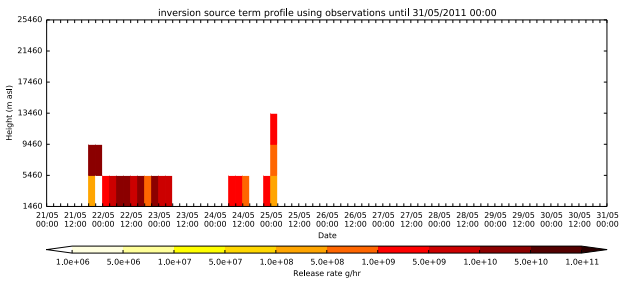

(e) emissions using satellite retrievals up to 00:00 UTC 31/05/2011

Figure 23: The best fit emission profile for the eruption of Grímsvötn using both ash and clear sky satellite observations and inversion code with the NNLS solver. (Note the different scales used along the time axis.)

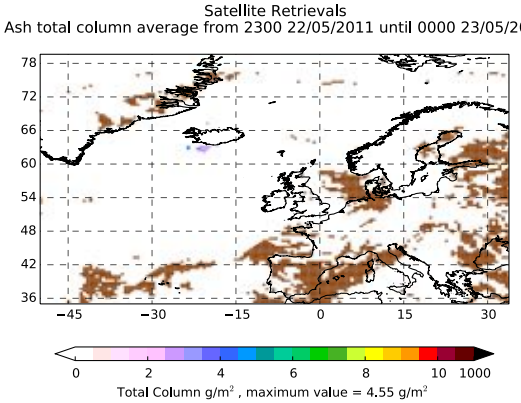

(a) ash and clear sky satellite retrievals

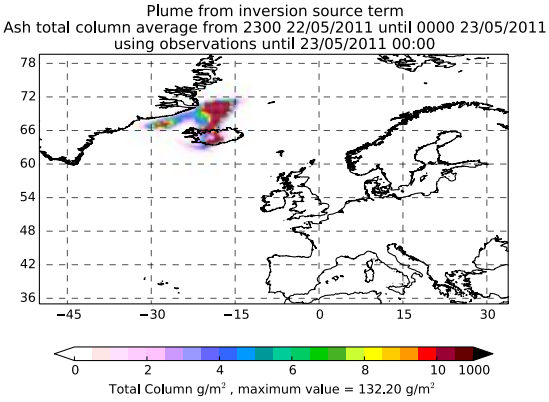

(b) plume using retrievals up to 00:00 UTC 23/05/2011

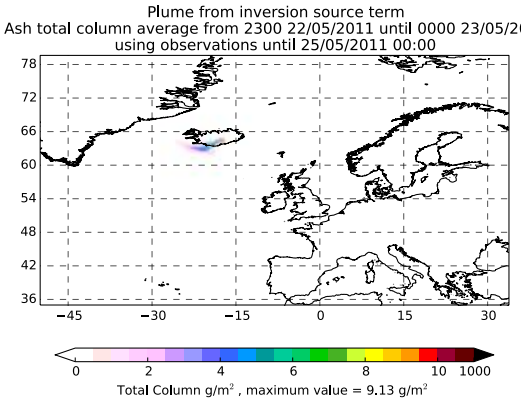

(c) plume using retrievals up to 00:00 UTC 25/05/2011

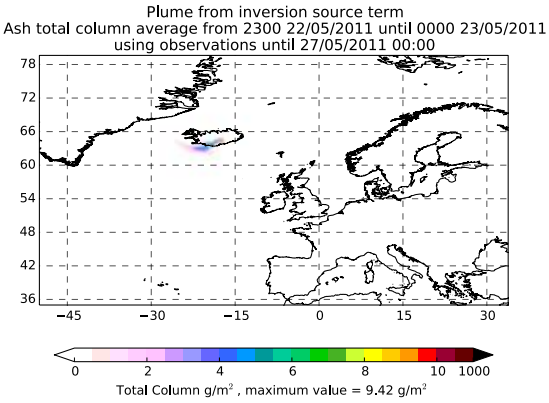

(d) plume using retrievals up to 00:00 UTC 27/05/2011

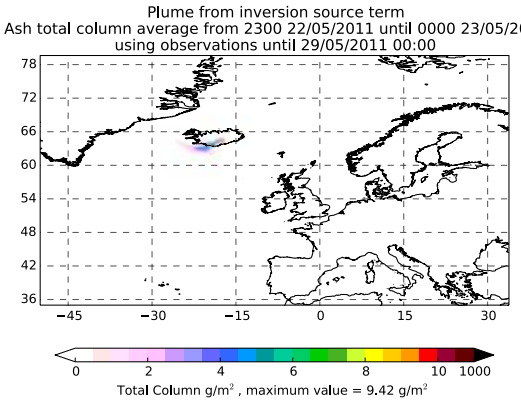

(e) plume using retrievals up to 00:00 UTC 29/05/2011

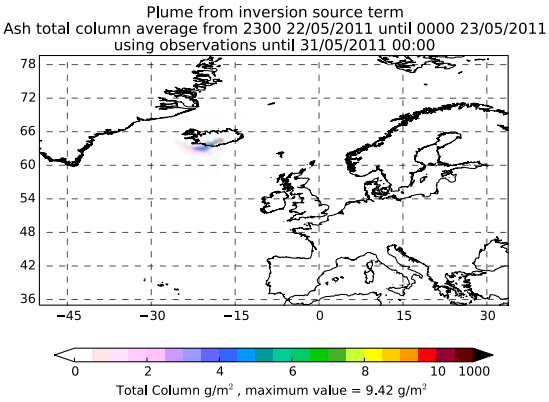

(f) plume using retrievals up to 00:00 UTC 31/05/2011

Figure 24: The Grímsvötn plume averaged between 23:00 UTC on 22/05/2011 and 00:00 UTC on 23/05/2011: (a) as observed by satellite (ash and clear skies, with clear skies shown in brown); and (b-f) as predicted by NAME with emissions determined using both ash and clear sky satellite observations and inversion code with the NNLS solver.

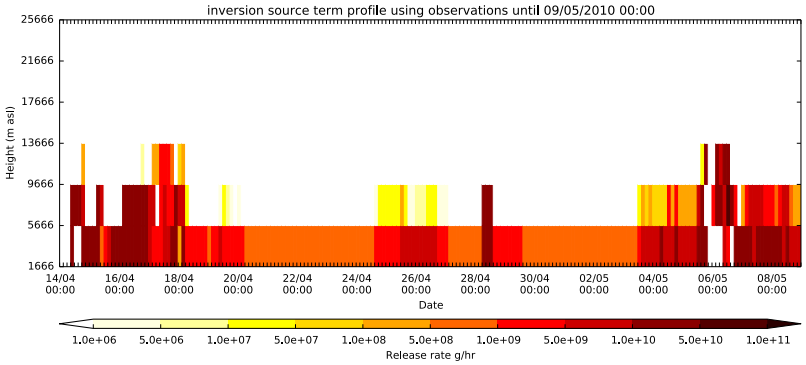

(a) emissions using satellite retrievals up to 00:00 UTC 09/05/2010

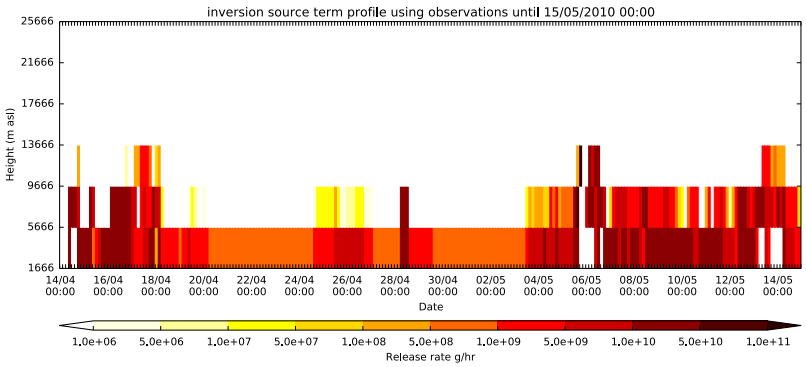

(b) emissions using satellite retrievals up to 00:00 UTC 15/05/2010

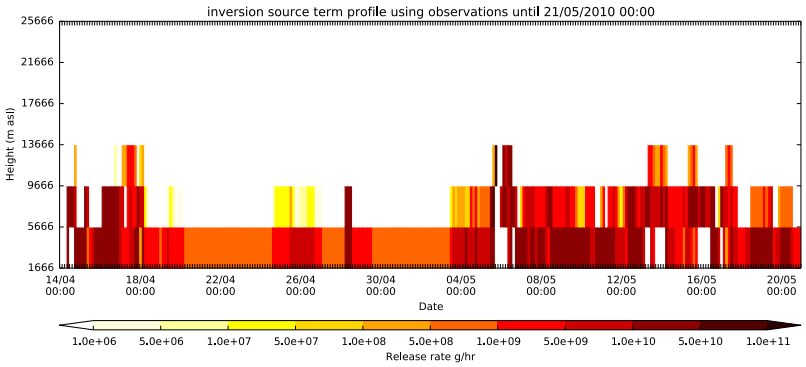

(c) emissions using satellite retrievals up to 00:00 UTC 21/05/2010

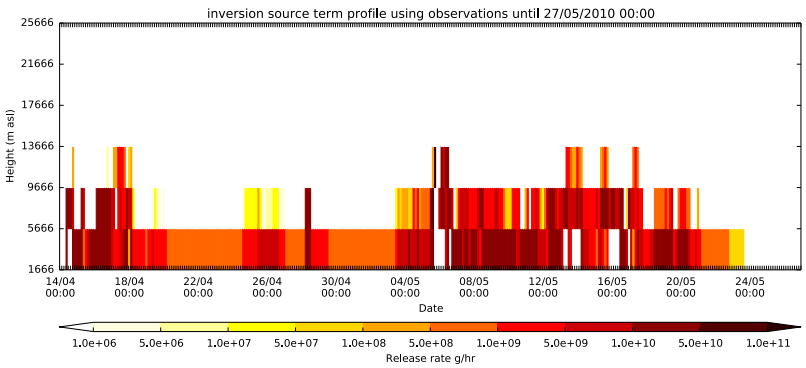

(d) emissions using satellite retrievals up to 00:00 UTC 27/05/2010

Figure 25: The best fit emission profile for the eruption of Eyjafjallajökull using ash-only satellite observations and inversion code with the NNLS solver. (Note the different scales used along the time axis.)

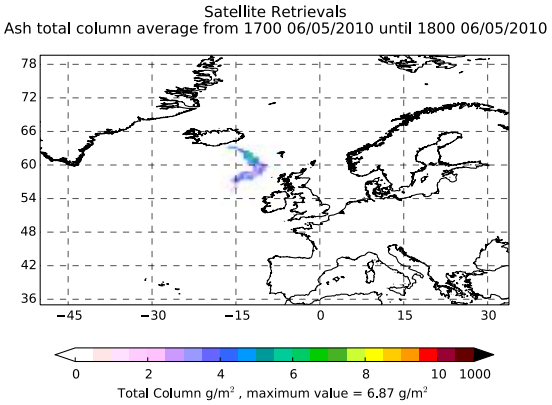

(a) ash-only satellite retrievals

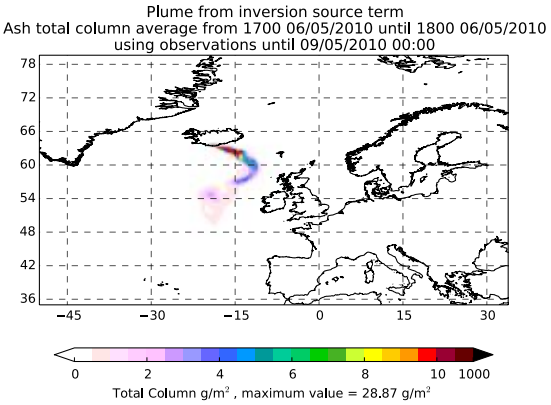

(b) plume using retrievals up to 00:00 UTC 09/05/2010

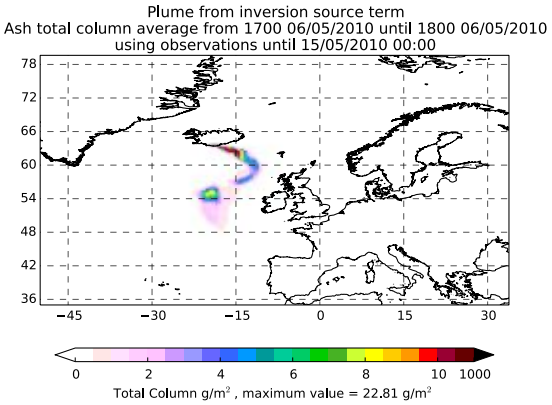

(c) plume using retrievals up to 00:00 UTC 15/05/2010

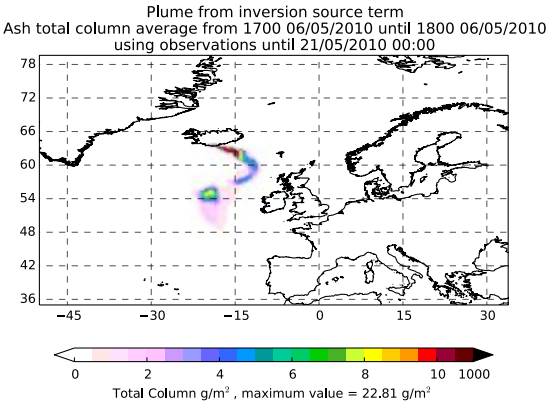

(d) plume using retrievals up to 00:00 UTC 21/05/2010

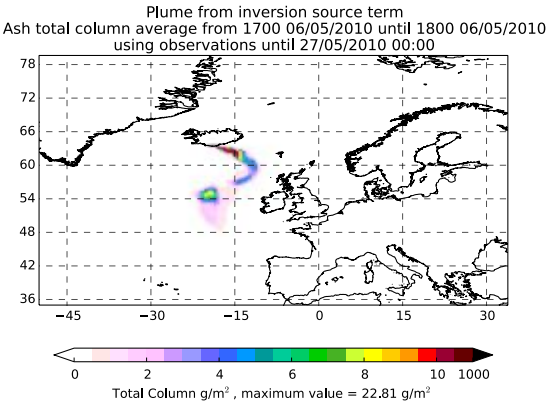

(e) plume using retrievals up to 00:00 UTC 27/05/2010

Figure 26: The Eyjafjallajökull plume averaged between 17:00 UTC and 18:00 UTC on 06/05/2010: (a) as observed by satellite (ash only); and (b-e) as predicted by NAME with emissions determined using ash-only satellite observations and inversion code with the NNLS solver.

4.2.2 Ash and clear sky observations

Figure 27 shows the *a posteriori* source determined using both ash and clear sky satellite observations until the dates given and using inversion code with the Lawson and Hanson NNLS solver [3]. Comparing figure 27 with the source obtained using simulated annealing (figures 11 and 19), one sees again that, although the main ash emissions obtained using the Lawson and Hanson solver occur at the same heights and times as those obtained using simulated annealing, there are many zero emission components in the Lawson and Hanson solution.

Figure 28 shows the modelled plume between 17:00 UTC and 18:00 UTC on 06/05/2010 using the *a posteriori* source in figure 27, together with the satellite observations valid at the same time, for comparison. There are some subtle differences in the predicted ash concentrations within the plume but, in general, there is good agreement with the simulated annealing results (cf. figures 12 and 20). As seen with the ash-only observations, the value of the cost function for the solution obtained using the Lawson and Hanson solver is less than the value obtained using simulated annealing (table 4), indicating that the simulated annealing technique is not reaching the actual minimum. Table 4 also assesses the run time of the Lawson and Hanson method, giving here a further speed up of about a factor of 45 on the restructured code, which, when taken in conjunction with the speed up seen when the cost function coefficients were pre-calculated, gives a speed up of about a factor of 150 over the original Pelley et al. [5] code.

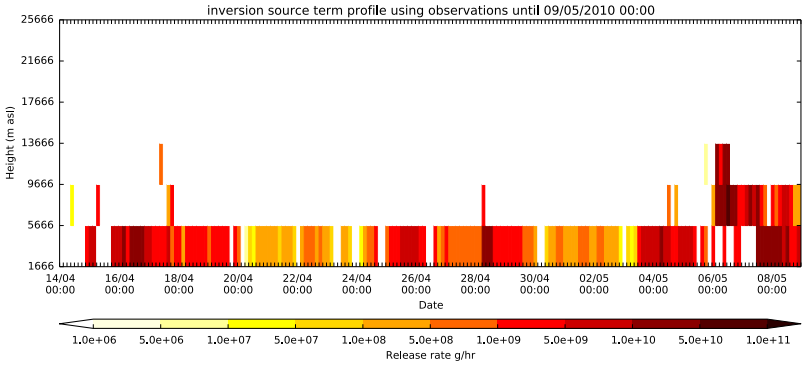

(a) emissions using satellite retrievals up to 00:00 UTC 09/05/2010

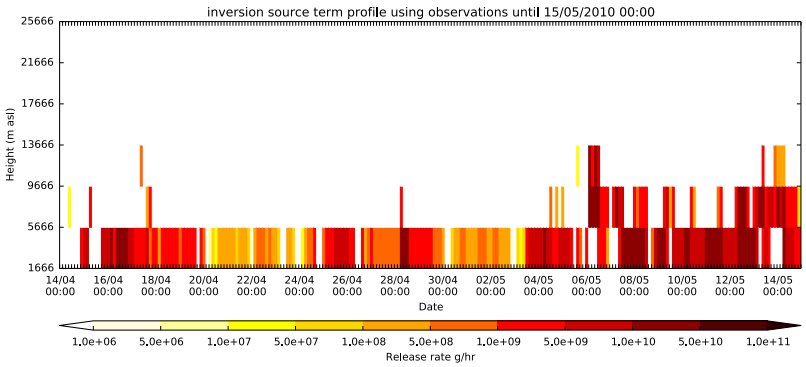

(b) emissions using satellite retrievals up to 00:00 UTC 15/05/2010

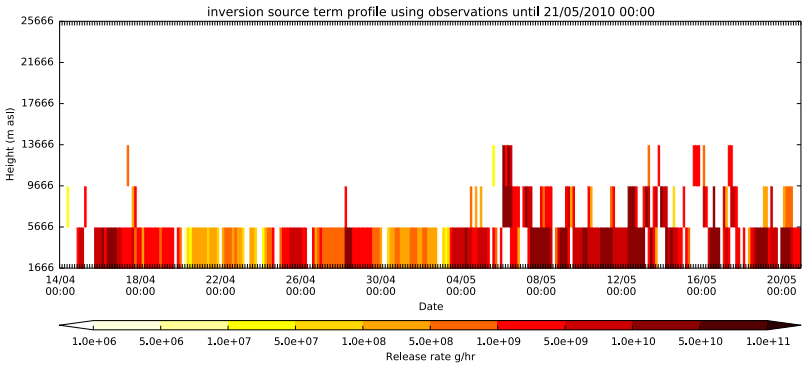

(c) emissions using satellite retrievals up to 00:00 UTC 21/05/2010

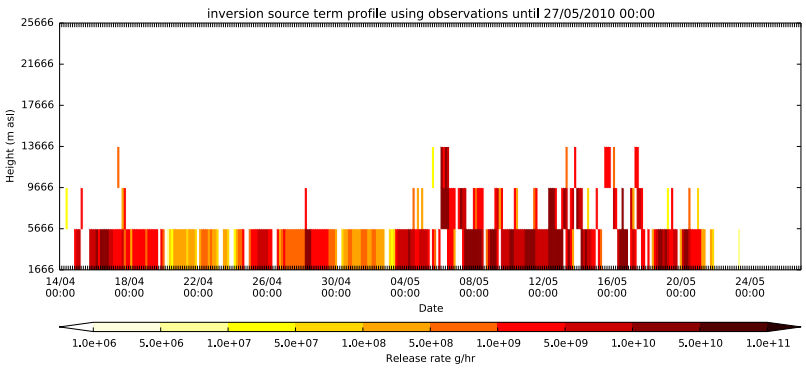

(d) emissions using satellite retrievals up to 00:00 UTC 27/05/2010

Figure 27: The best fit emission profile for the eruption of Eyjafjallajökull using both ash and clear sky satellite observations and inversion code with the NNLS solver. (Note the different scales used along the time axis.)

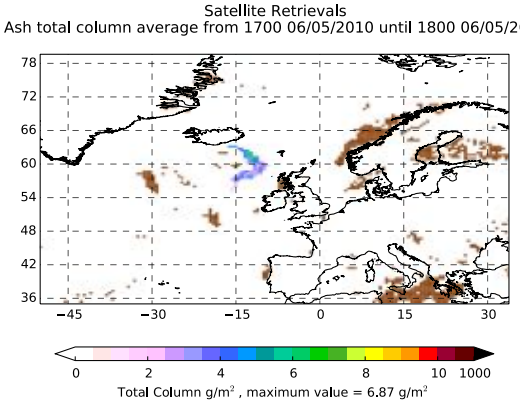

(a) ash and clear sky satellite retrievals

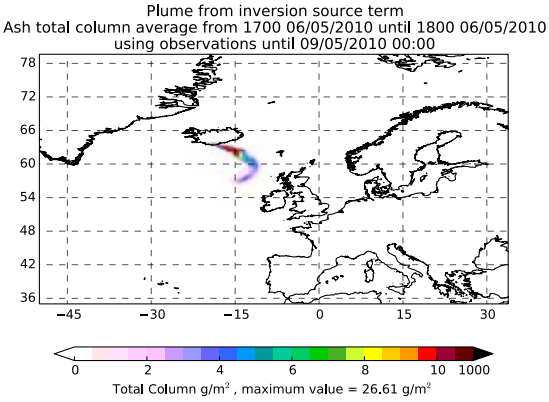

(b) plume using retrievals up to 00:00 UTC 09/05/2010

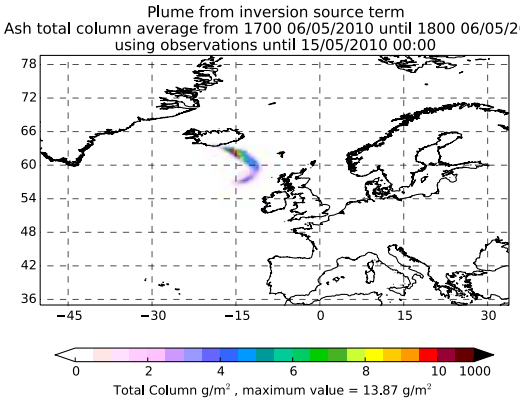

(c) plume using retrievals up to 00:00 UTC 15/05/2010

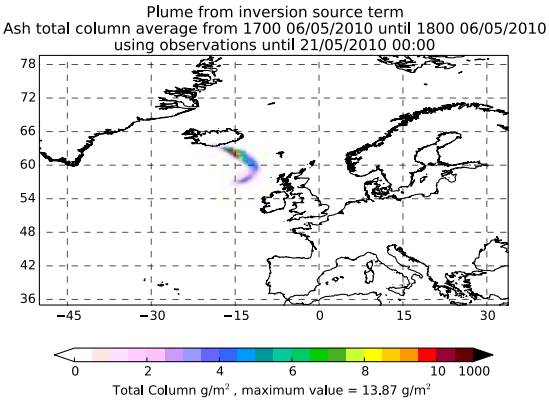

(d) plume using retrievals up to 00:00 UTC 21/05/2010

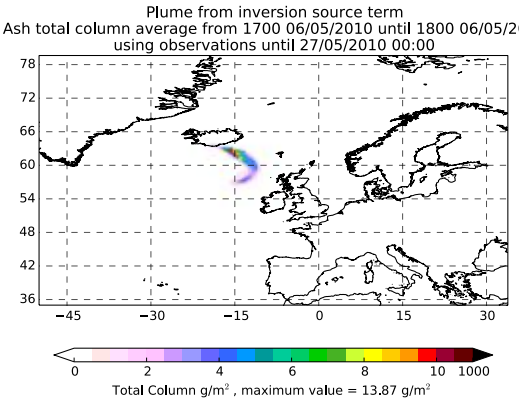

(e) plume using retrievals up to 00:00 UTC 27/05/2010

Figure 28: The Eyjafjallajökull plume averaged between 17:00 UTC and 18:00 UTC on 06/05/2010: (a) as observed by satellite (ash and clear skies, with clear skies shown in brown); and (b-e) as predicted by NAME with emissions determined using both ash and clear sky satellite observations and inversion code with the NNLS solver.

5 Including cross correlations in the *a priori* error covariance matrix

It is likely that cross correlations exist between the errors in individual *a priori* source elements, either at different heights or at different times. In reality correlations may be introduced by variations in the plume rise height from the reported eruption height, by variations in the mass release rate from the assumed mass-to-eruption-height relationship and by variations in the vertical distribution of mass from the assumed uniform distribution. In this section we show the effect of including cross correlations in the *a priori* error covariance matrix $\mathbf{B}$ (i.e. including non-zero off diagonal components) using the approach set out in the companion report [7]. We also use the approach in [7] for the *a priori* mean emissions; this gives slightly different results to [5] because of the way it accounts for errors in the plume rise height. For simplicity, in the following we often present the differences between the results in this section and in section 4 as being due to the cross correlations; however the fact that the *a priori* mean emissions have changed too should be kept in mind.

In the model for $\mathbf{B}$ given in [7] there are a number of adjustable parameters: T_H – the timescale for errors in the plume rise height; σ_r and T_r – the standard deviation and timescale for errors in the mass release rate for a given plume rise height; and σ_q, T_q and L_q – the standard deviation, timescale and lengthscale for variations in the shape of the vertical profile. Note σ_r and σ_q are defined relative to the mean and L_q is relative to the plume rise height. Hence these quantities are dimensionless. Here we choose the following parameter values: $T_H = 12$ hours, $\sigma_r = 1$, $T_r = 12$ hours, $\sigma_q = 1$, $T_q = 3$ hours and $L_q = 0.3$. Some indication of the sensitivity of the inversion results to the parameter choices is given in appendix B.

The greater efficiency of the NNLS solver allows us to be able to consider increasing the spatial and temporal resolution of the source. We have explored this using the inversion code with the new *a priori* model [7] and the NNLS solver in appendix C.

Some tests of the statistical consistency of the inversion are presented in section 6 and some comparisons against independent data in section 7.

5.1 Grímsvötn 2011

Figure 29 shows the *a priori* mean effective source profile based on observations of the eruption plume height, on the Mastin relationship between eruption plume height and mass eruption rate [4], and on the assumption of a 5% distal fine ash fraction as before, but now using the approach in [7]. This approach calculates the mean value over a range of plausible eruption heights (given a potential error in the observed plume height). The result is, in the main, similar to the *a priori* source in figure 1. However, there are now some emissions above the estimated plume rise height, albeit in relatively low quantities, reflecting the possibility of the plume reaching these heights. Also the emissions near but below the mean rise height are reduced, reflecting the possibility that the

plume won't reach these heights. The modelled plume between 23:00 UTC on 22/05/2011 and 00:00 UTC on 23/05/2011 (figure 30), obtained using the *a priori* source in figure 29, is very similar to the predicted plume in figure 2.

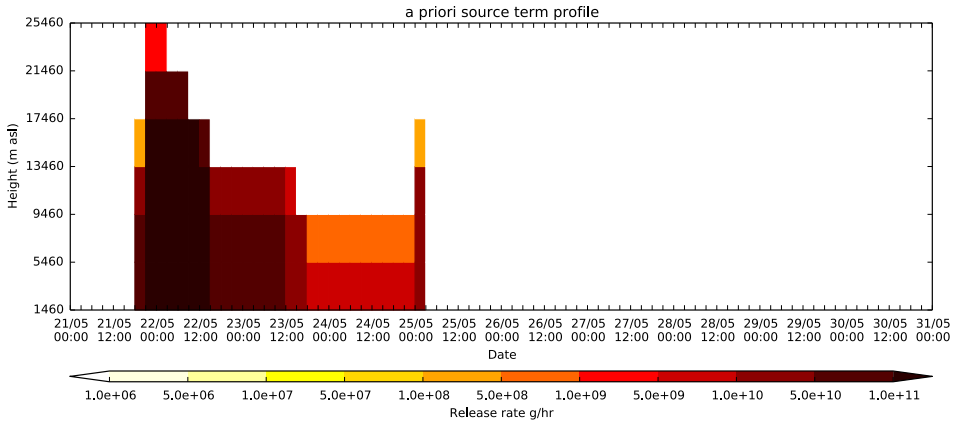

Figure 29: The *a priori* mean emission profile for the eruption of Grímsvötn in May 2011, obtained using the new *a priori* model [7].

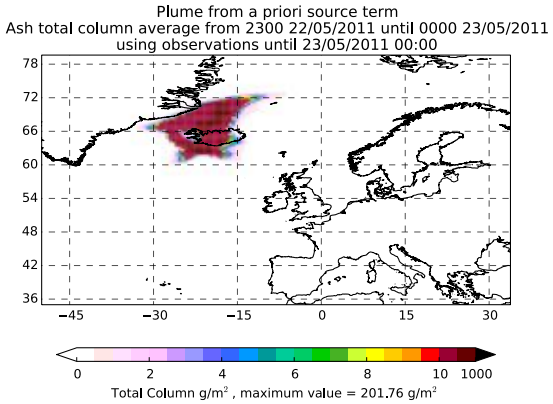

Figure 30: The NAME plume averaged between 23:00 UTC on 22/05/2011 and 00:00 UTC on 23/05/2011 for the 2011 Grímsvötn eruption, obtained using the *a priori* mean emission profile in figure 29.

5.1.1 Ash-only observations

Figure 31 shows the *a posteriori* source determined using ash-only observations until the dates given and using the inversion code with the new *a priori* model [7] and the NNLS solver. There are some differences compared to the *a posteriori* source determined using the previous *a priori* source described in [5] (cf. figure 21). These differences are, to some degree due to the different *a priori* mean source. However, there is evidence that the inclusion of cross correlations enables the *a posteriori* source to adjust quicker from the *a priori* since a small number of observations can influence a larger number of source components.

There is little change from the *a priori* mean emissions after 18:00 UTC on 23/05/2016. This may be because the emissions in this period are predicted by NAME to affect a much smaller number of the available observations than the earlier emissions. Also, in the bulk of this period, the estimated plume rise height is low and hence emissions are likely to be low and any satellite ash detections are likely to have a poor signal to noise ratio. Under these circumstances, differences from the *a priori* mean are expected to be small. However the differences from the *a priori* mean are smaller than were seen previously in figures 3, 13 and 21. This is probably due to a combination of the incomplete convergence of the simulated annealing in figures 3 and 13 and the reduced tendency to "over-fit" to the observations in figure 31 as a result of the introduction of the *a priori* cross correlations.

Figure 32 shows the modelled plume between 23:00 UTC on 22/05/2011 and 00:00 UTC on 23/05/2011 using the *a posteriori* sources in figure 31, together with the ash observations from the satellite retrieval valid at the same time. There are some noticeable differences from the plumes in figure 22 which do not consider cross correlations in the *a priori* error covariance matrix. In particular, the region of ash north-west of Iceland, which in figure 22 is reduced as the satellite data cut-off time is increased, has been removed almost completely from the predicted plume, even with an early satellite data cut-off time. In general, there is less atmospheric ash in the predicted plume when using the new *a priori* emissions model [7].

Table 1 shows that the cost of including cross correlations in the *a priori* error covariance matrix is minimal.

5.1.2 Ash and clear sky observations

Figure 33 shows the *a posteriori* source determined using both ash and clear sky satellite observations until the dates given, and using the inversion code with the new *a priori* model [7] and the NNLS solver. Again there are some differences evident when compared to the *a posteriori* source determined using the previous *a priori* source described in [5] (cf. figure 23). One can see, particularly in figure 33a and for the predicted emissions in the latter part of the eruption in figures 33c to 33e, that the predicted source tends to have less ash when using the new *a priori* emissions model [7].

Figure 34 shows the modelled plume between 23:00 UTC on 22/05/2011 and 00:00 UTC on 23/05/2011 using the *a posteriori* source in figure 33, together with the satellite observations valid at the same time. Comparing figure 34b with the corresponding predicted plume (figure 24b) obtained with no cross correlations in the *a priori* error covariance matrix, we see that the inclusion of cross correlations can have a significant effect on the predicted ash plume, with the ash to the north-west of Iceland almost completely removed and the ash to the north of Iceland reduced relative to the result without cross correlations. Together with the ash-only results in figure 32, this supports the idea that the cross correlations in the *a priori* error covariance matrix allow the observations to have a wider influence and to affect more source elements, thus enabling the predicted plume to adjust

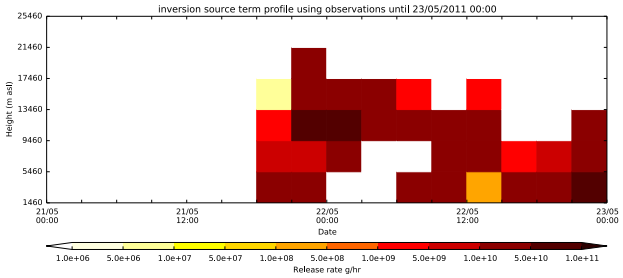

(a) emissions using satellite retrievals up to 00:00 UTC 23/05/2011

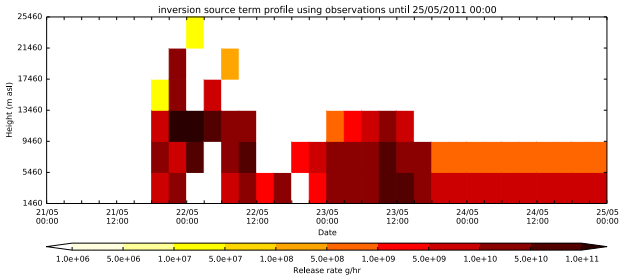

(b) emissions using satellite retrievals up to 00:00 UTC 25/05/2011

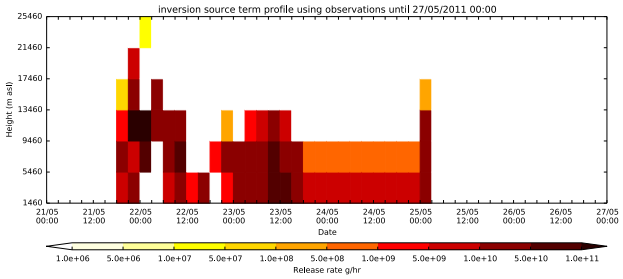

(c) emissions using satellite retrievals up to 00:00 UTC 27/05/2011

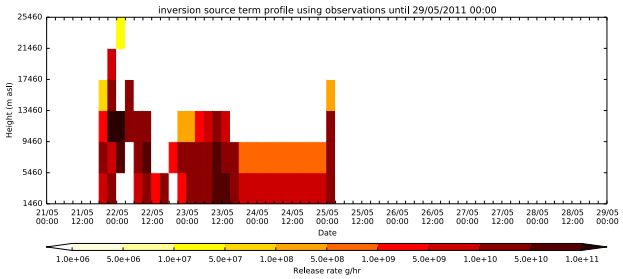

(d) emissions using satellite retrievals up to 00:00 UTC 29/05/2011

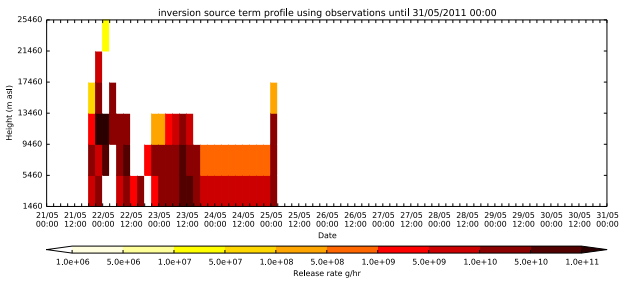

(e) emissions using satellite retrievals up to 00:00 UTC 31/05/2011

Figure 31: The best fit emission profile for the eruption of Grímsvötn using ash-only satellite observations and inversion code with the new *a priori* model [7] and the NNLS solver. (Note the different scales used along the time axis.)

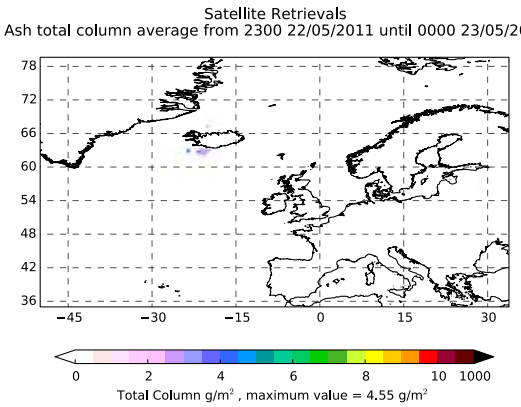

(a) ash-only satellite retrievals

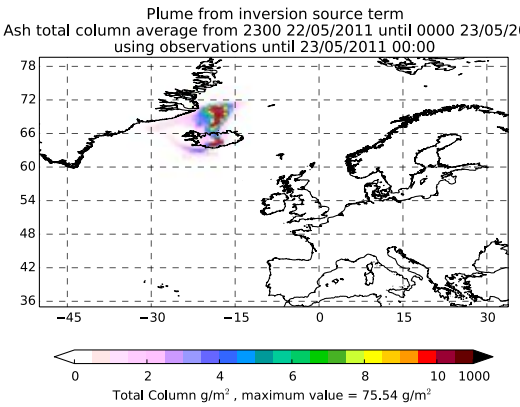

(b) plume using retrievals up to 00:00 UTC 23/05/2011

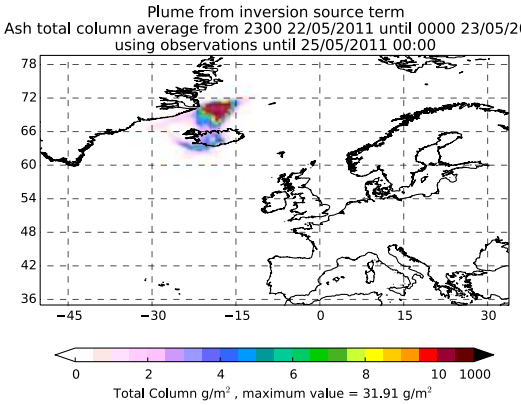

(c) plume using retrievals up to 00:00 UTC 25/05/2011

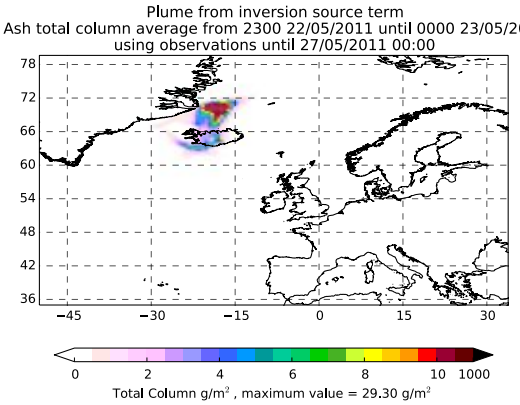

(d) plume using retrievals up to 00:00 UTC 27/05/2011

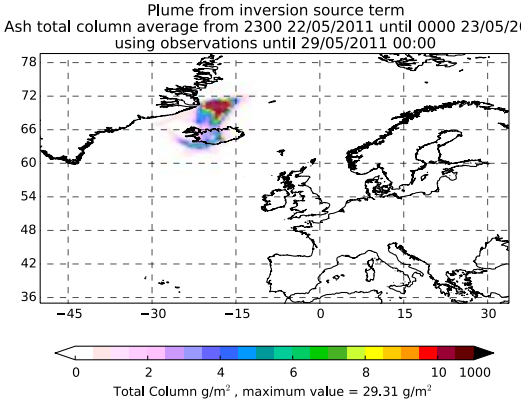

(e) plume using retrievals up to 00:00 UTC 29/05/2011

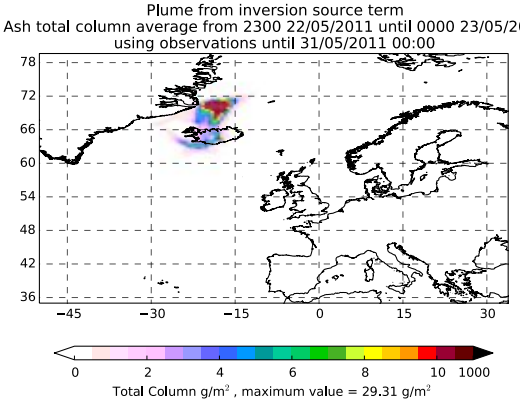

(f) plume using retrievals up to 00:00 UTC 31/05/2011

Figure 32: The Grímsvötn plume averaged between 23:00 UTC on 22/05/2011 and 00:00 UTC on 23/05/2011: (a) as observed by satellite (ash only); and (b-f) as predicted by NAME with emissions determined using ash-only satellite observations and inversion code with the new *a priori* model [7] and the NNLS solver.

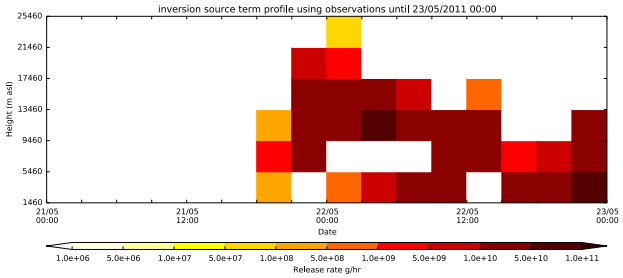

(a) emissions using satellite retrievals up to 00:00 UTC 23/05/2011

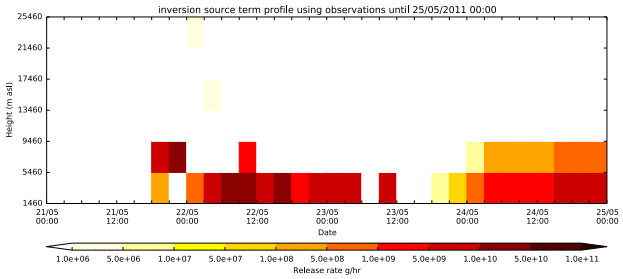

(b) emissions using satellite retrievals up to 00:00 UTC 25/05/2011

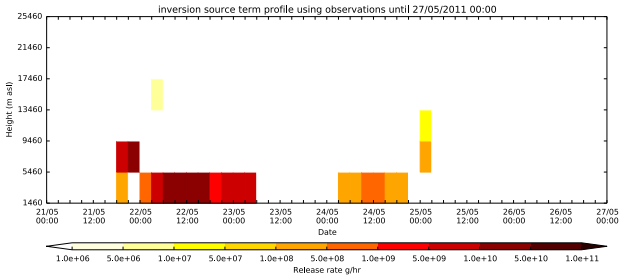

(c) emissions using satellite retrievals up to 00:00 UTC 27/05/2011

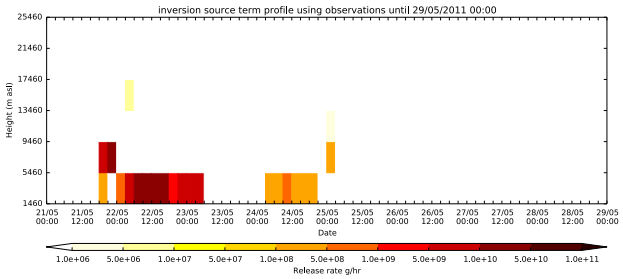

(d) emissions using satellite retrievals up to 00:00 UTC 29/05/2011

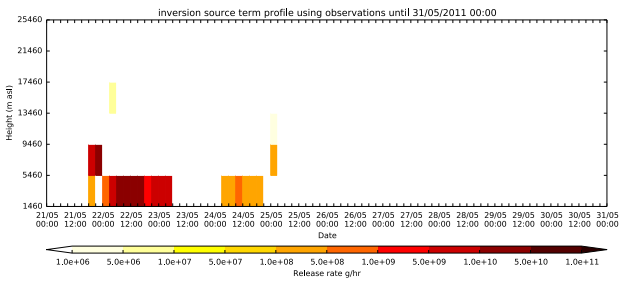

(e) emissions using satellite retrievals up to 00:00 UTC 31/05/2011

Figure 33: The best fit emission profile for the eruption of Grímsvötn using both ash and clear sky satellite observations and inversion code with the new *a priori* model [7] and the NNLS solver. (Note the different scales used along the time axis.)

away from the *a priori* quicker. The result here is to reduce the amount of ash predicted within the plume. When more observations from later times are included in the inversion process (see figures 34c to 34f), the predicted plumes with and without considering cross correlations in the *a priori* error covariance matrix agree well. This suggests that when there are a large number of observations constraining the solution, the result is not strongly influenced by cross correlations in the *a priori* error covariance matrix.

As was seen for ash-only observations, table 2 shows that the run-time cost of including cross correlations in the *a priori* error covariance matrix is minimal.

5.2 Eyjafjallajökull 2010

Figure 35 shows the *a priori* mean effective source profile based on observations of the eruption plume height, on the Mastin relationship between eruption plume height and mass eruption rate [4], and on the assumption of a 5% distal fine ash fraction, using the approach in [7]. As seen for the 2011 Grímsvötn eruption example, this is, in the main, similar to the *a priori* source in figure 7 but with some changes near the plume rise height reflecting the uncertainty in the plume rise height. The modelled plume between 17:00 UTC and 18:00 UTC on 06/05/2010 (figure 36), obtained using the *a priori* mean source in figure 35, is very similar to the predicted plume in figure 8.

5.2.1 Ash-only observations

Figure 37 shows the *a posteriori* source determined for the Eyjafjallajökull eruption in 2010 using ash-only observations until the dates given, and using the inversion code with the new *a priori* model [7] and the NNLS solver. Again, there are some differences compared to the *a posteriori* source determined without considering cross correlations in the error covariance matrix for the *a priori* source (cf. figure 25). The inclusion of cross correlations can both increase the emissions in the *a posteriori* source (see, for example, the increases to the relatively low emissions around 22/04/2010 and 01/05/2010) and decrease emissions in the *a posteriori* source (see the initial stages of the eruption).

Figure 38 shows the modelled plume between 23:00 UTC on 22/05/2011 and 00:00 UTC on 23/05/2011 using the *a posteriori* source in figure 37, together with the ash observations from the satellite retrieval valid at the same time. The predicted ash plumes look very similar to those in figure 26 which do not consider cross correlations in the *a priori* error covariance matrix. There are, however, some small differences. For example, there is less ash predicted in the region around 54°N, 20°W when cross correlations are considered.

Table 3 shows that the increased cost of including cross correlations in the *a priori* error covariance matrix is greater for the Eyjafjallajökull 2010 test case than seen for the Grímsvötn 2011 test case. The inclusion of cross correlations adds approximately 60% to the run-time of the inversion calculation. However, the time taken by the inversion calculation is not large and is significantly

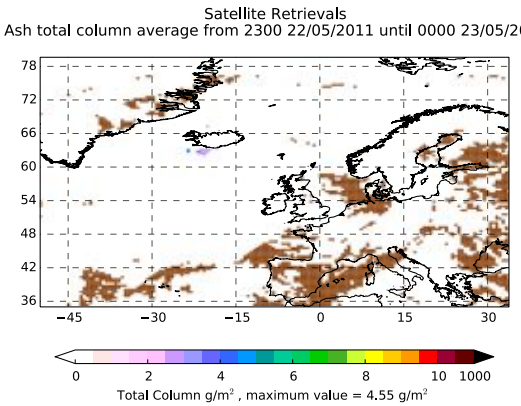

(a) ash and clear sky satellite retrievals

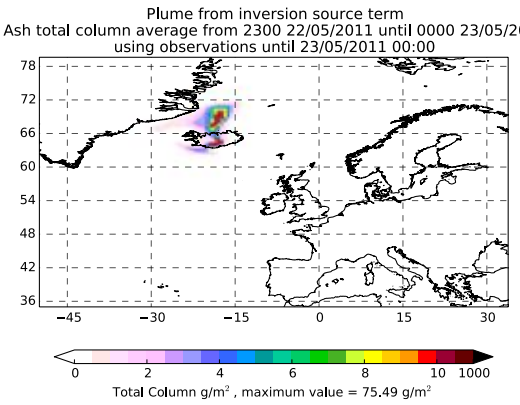

(b) plume using retrievals up to 00:00 UTC 23/05/2011

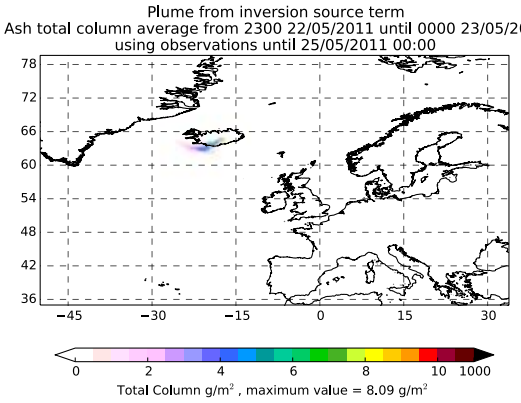

(c) plume using retrievals up to 00:00 UTC 25/05/2011

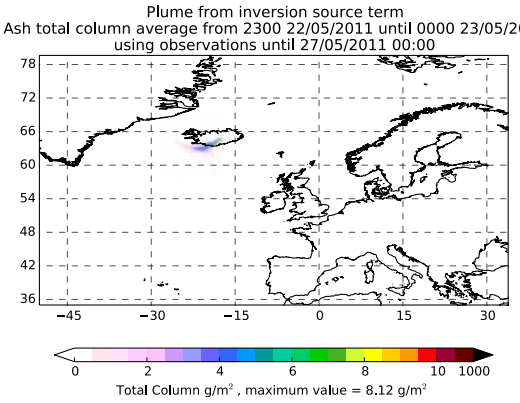

(d) plume using retrievals up to 00:00 UTC 27/05/2011

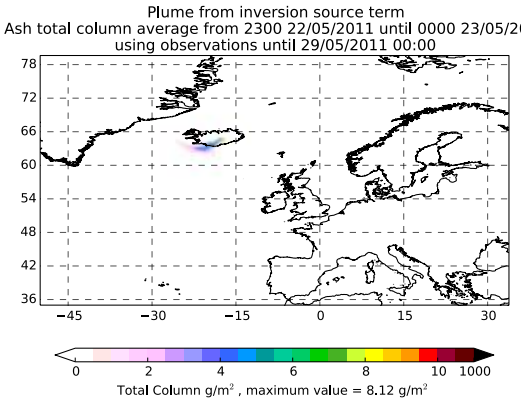

(e) plume using retrievals up to 00:00 UTC 29/05/2011

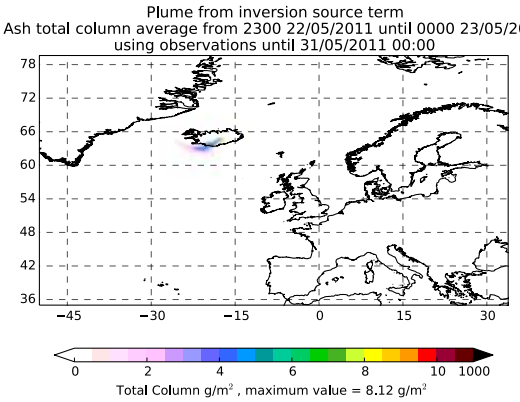

(f) plume using retrievals up to 00:00 UTC 31/05/2011

Figure 34: The Grímsvötn plume averaged between 23:00 UTC on 22/05/2011 and 00:00 UTC on 23/05/2011: (a) as observed by satellite (ash and clear skies, with clear skies shown in brown); and (b-f) as predicted by NAME with emissions determined using both ash and clear sky satellite observations and inversion code with the new *a priori* model [7] and the NNLS solver.

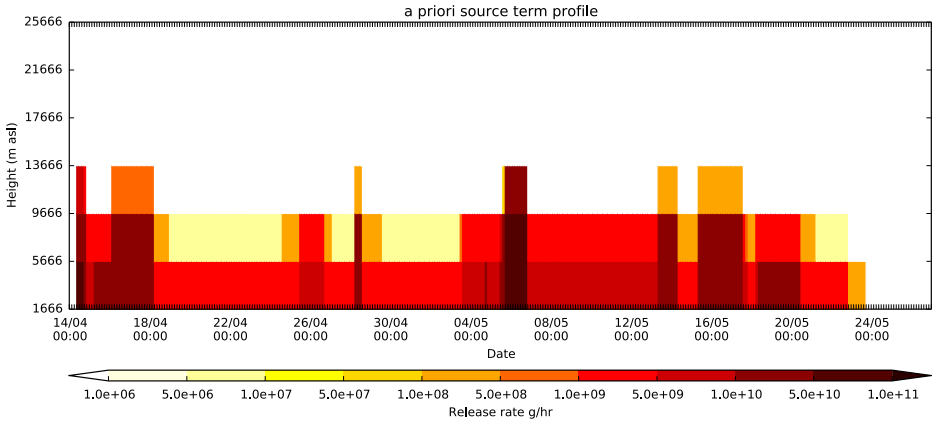

Figure 35: The *a priori* mean emission profile for the eruption of Eyjafjallajökull in 2010, obtained using the new *a priori* model [7].

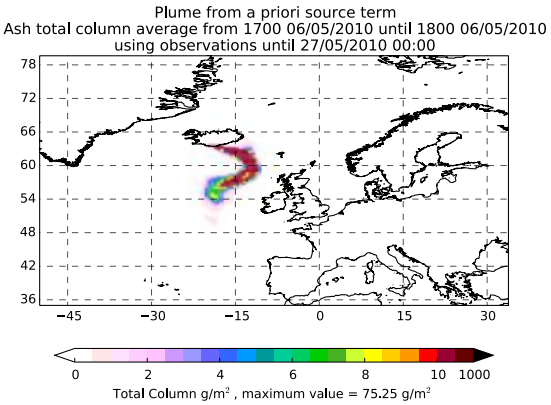

Figure 36: The NAME plume averaged between 17:00 UTC and 18:00 UTC on 06/05/2010 for the 2010 Eyjafjallajökull eruption, obtained using the *a priori* mean emission profile in figure 35.

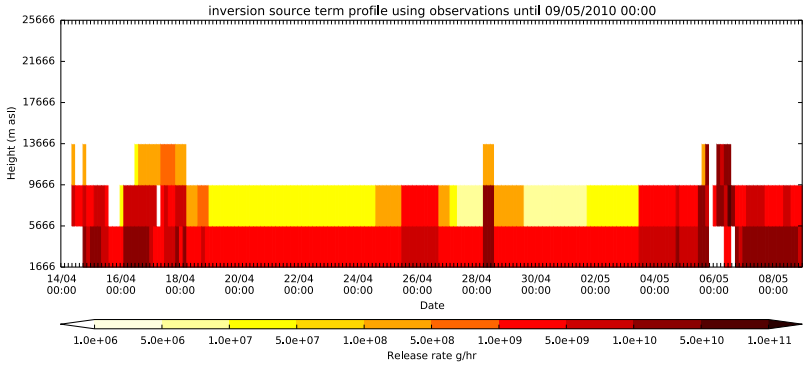

(a) emissions using satellite retrievals up to 00:00 UTC 09/05/2010

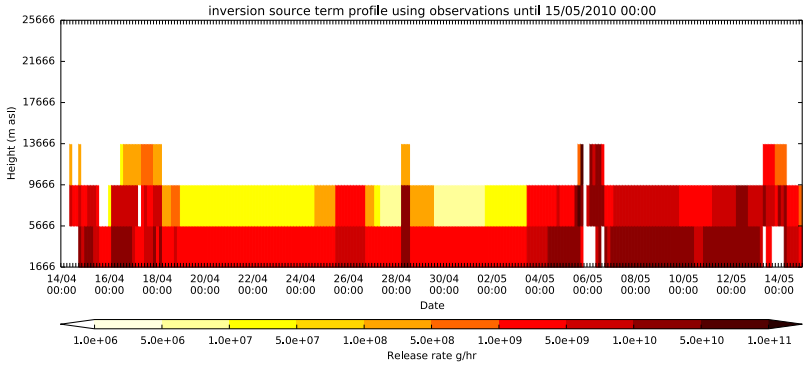

(b) emissions using satellite retrievals up to 00:00 UTC 15/05/2010

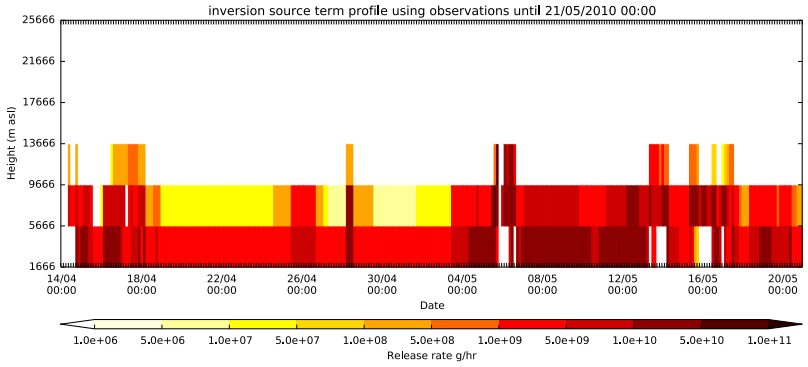

(c) emissions using satellite retrievals up to 00:00 UTC 21/05/2010

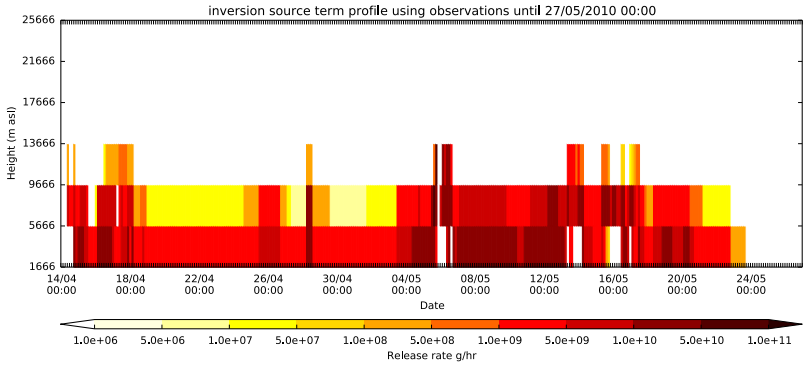

(d) emissions using satellite retrievals up to 00:00 UTC 27/05/2010

Figure 37: The best fit emission profile for the eruption of Eyjafjallajökull using ash-only satellite observations and inversion code with the new *a priori* model [7] and the NNLS solver. (Note the different scales used along the time axis.)

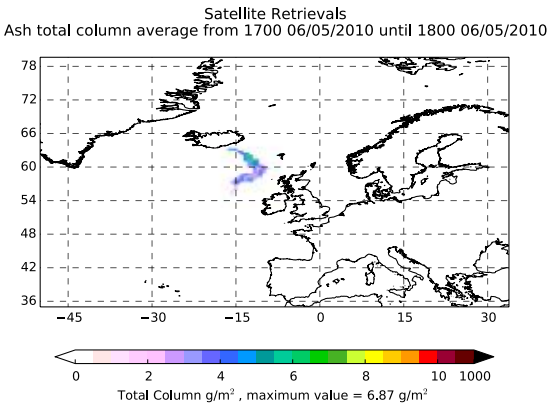

(a) ash-only satellite retrievals

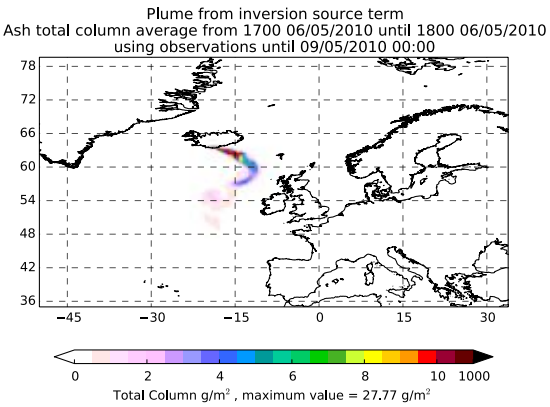

(b) plume using retrievals up to 00:00 UTC 09/05/2010

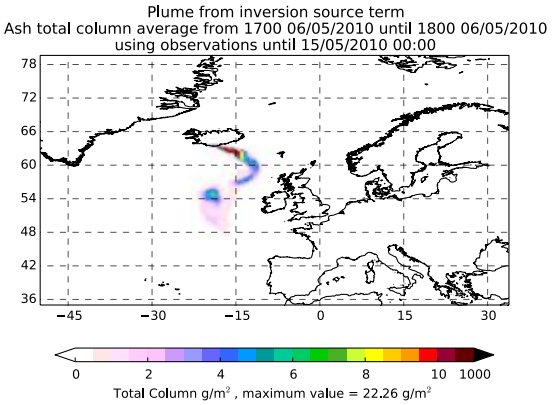

(c) plume using retrievals up to 00:00 UTC 15/05/2010

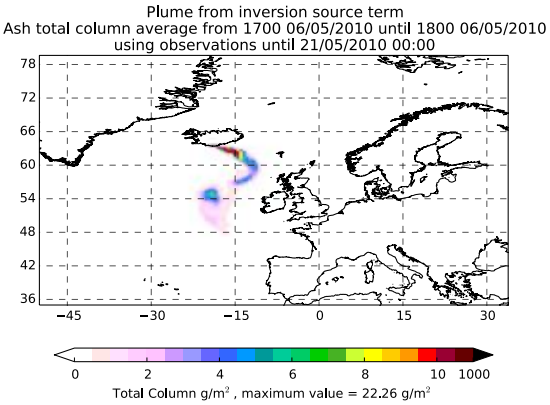

(d) plume using retrievals up to 00:00 UTC 21/05/2010

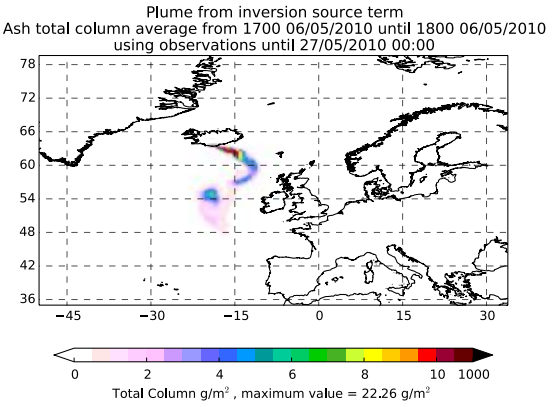

(e) plume using retrievals up to 00:00 UTC 27/05/2010

Figure 38: The Eyjafjallajökull plume averaged between 17:00 UTC and 18:00 UTC on 06/05/2010: (a) as observed by satellite (ash only); and (b-e) as predicted by NAME with emissions determined using ash-only satellite observations and inversion code with the new *a priori* model [7] and the NNLS solver.

less than for the original code. Although we have not investigated the increase in cost in detail, it seems plausible that this is due to the cost of calculating the *a priori* correlations which scales as the square of the number of source elements.

5.2.2 Ash and clear sky observations

Figure 39 shows the *a posteriori* source determined using both ash and clear sky satellite observations until the dates given, and using the inversion code with the new *a priori* model [7] and the NNLS solver. Again there are some differences evident when compared to the *a posteriori* source determined with no cross correlations in the *a priori* error covariance matrix (cf. figure 27). In particular, the inclusion of cross correlations in the *a priori* error covariance matrix results in a smoother *a posteriori* source profile with fewer periods of zero emissions.

Figure 40 shows the modelled plume between 17:00 UTC and 18:00 UTC on 06/05/2010 using the *a posteriori* source in figure 39, together with the satellite observations valid at the same time. The predicted plumes look very similar to those in figure 28, obtained with no cross correlations in the *a priori* error covariance matrix. This supports the view that a sufficiently large number of observations (more easily achieved when clear sky satellite observations are included) can constrain the problem well and the solution is then not as strongly influenced by the cross correlations in the *a priori* error covariance matrix.

As seen for the ash-only observations case, the additional cost of including cross correlations in the *a priori* error covariance matrix is greater in the Eyjafjallajökull 2010 example than in the Grímsvötn 2011 example (see table 4). That said, the increase in cost is relatively small, with the inversion run-time a small fraction of that of the original code.

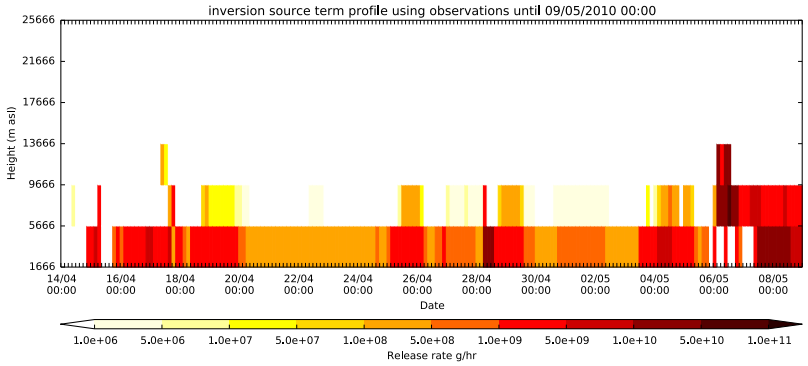

(a) emissions using satellite retrievals up to 00:00 UTC 09/05/2010

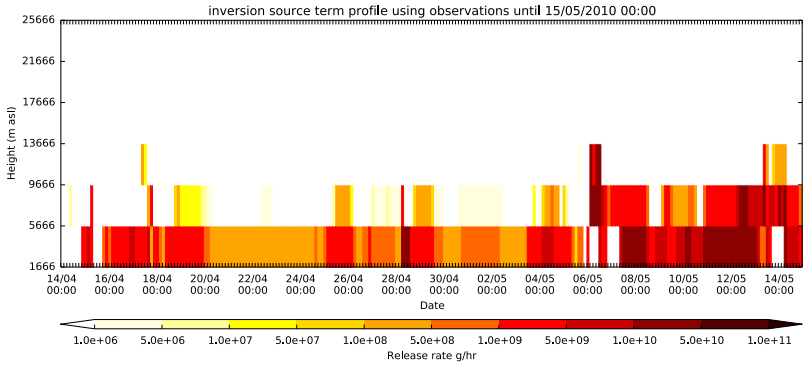

(b) emissions using satellite retrievals up to 00:00 UTC 15/05/2010

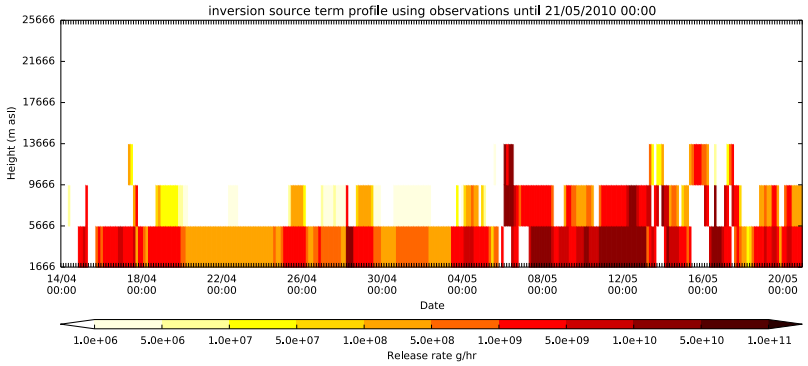

(c) emissions using satellite retrievals up to 00:00 UTC 21/05/2010

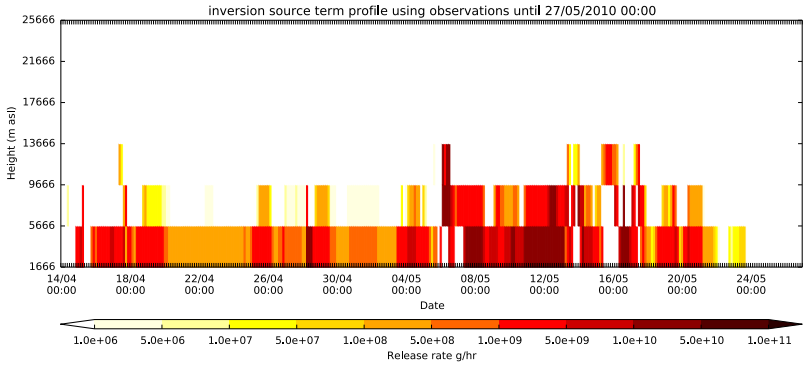

(d) emissions using satellite retrievals up to 00:00 UTC 27/05/2010

Figure 39: The best fit emission profile for the eruption of Eyjafjallajökull using both ash and clear sky satellite observations and inversion code with the new *a priori* model [7] and the NNLS solver. (Note the different scales used along the time axis.)

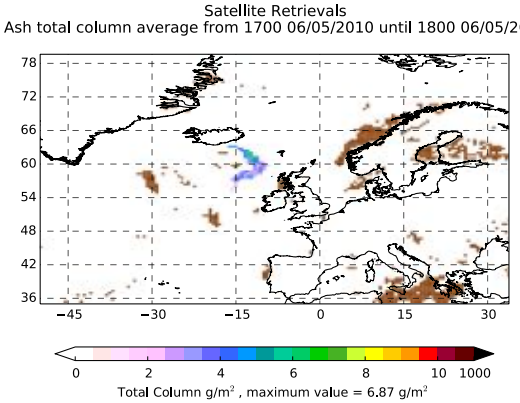

(a) ash and clear sky satellite retrievals

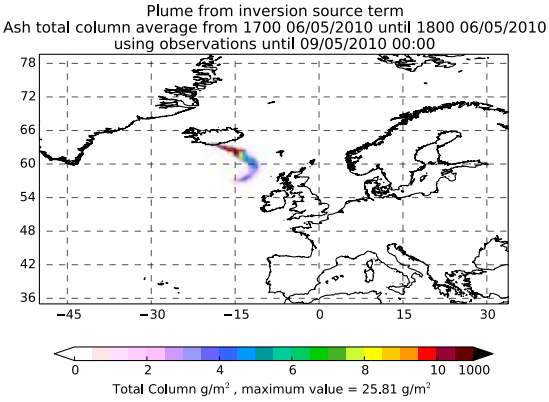

(b) plume using retrievals up to 00:00 UTC 09/05/2010

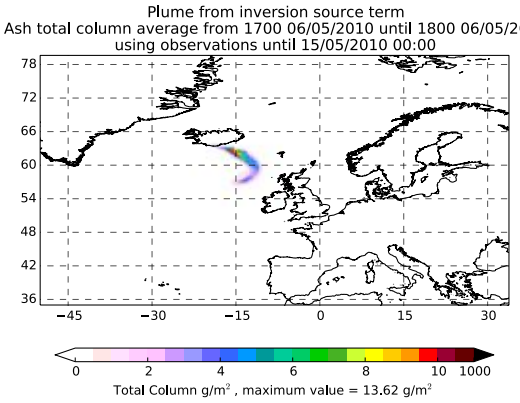

(c) plume using retrievals up to 00:00 UTC 15/05/2010

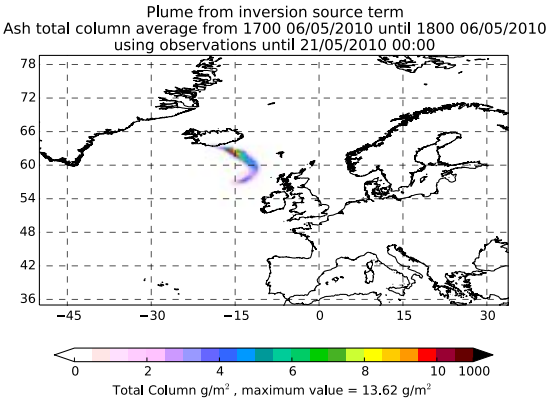

(d) plume using retrievals up to 00:00 UTC 21/05/2010

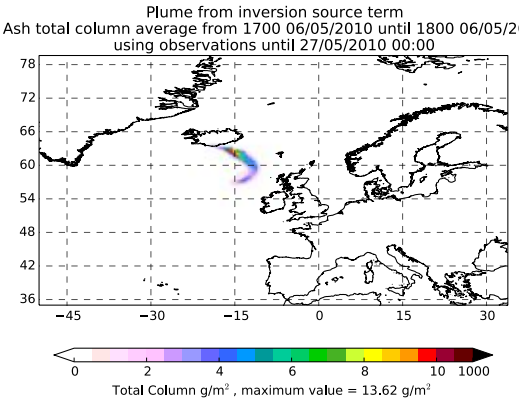

(e) plume using retrievals up to 00:00 UTC 27/05/2010

Figure 40: The Eyjafjallajökull plume averaged between 17:00 UTC and 18:00 UTC on 06/05/2010: (a) as observed by satellite (ash and clear skies, with clear skies shown in brown); and (b-e) as predicted by NAME with emissions determined using both ash and clear sky satellite observations and inversion code with the new *a priori* model [7] and the NNLS solver.

6 Statistical consistency of the inversion

It is useful to test whether the statistical framework for the inversion is consistent with the data available. For example, the *a posteriori* emissions should not be too far outside the range of uncertainty in the *a priori*. If they are, it is likely that the *a priori* errors were significantly underestimated. Similarly the (*a posteriori*) error range obtained from the inversion using certain satellite observations should be consistent with the emission estimates made using more data. For example one can compare estimates made at one time with estimates made later when more data is available, or one can compare estimates made using ash-only observations with estimates made using ash and clear sky observations.

In figures 41 to 45 we present the results for the total daily emission on each of the 5 days of the Grímsvötn eruption. Results are shown using the observations which are available up to a range of cut-off times and using either ash-only or both ash and clear sky observations. The NNLS solution algorithm is used with both the original and new *a priori* models, using the inversions presented in sections 4.1 and 5.1 above. Error bars on the total emissions show plus/minus one standard deviation, computed as the square root of the sum of the relevant components of the analysis error covariance matrix $\mathbf{A}$. The number of 'observation uses' is also presented. This is computed by considering the number of observations which influence each source element estimate as a result of $\mathbf{M}$ having a non-zero entry linking the source and observation, with the results being summed over the source elements which contribute to the day's emissions. Note that for the new *a priori* model with cross correlations, observations can also influence source elements indirectly via cross correlations with another source element. These indirect influences aren't included.

The results have to be interpreted carefully. For example, because the range of emissions is significant we have plotted emissions on a log scale. This means that the lower extent of the error bar can be quite sensitive to the standard deviation when the standard deviation is comparable to the mean estimate. Also of course one should expect a significant probability (32% for a Gaussian distribution) of being more than one standard deviation from the mean. The results with the new *a priori* model seem reasonably consistent and better than the results with the old model. The improvement in consistency is most noticeable on 22/05/2011 and 23/05/2011, with the *a priori* errors in the old model appearing too small and later emission estimates lying far outside these error bars. An improvement is also arguably present on 21/05/2011. However there is little difference in consistency on 24/05/2011 and 25/05/2011. We note that on these two dates the ash-only observations have little impact on the estimated emissions which remain close to the *a priori* estimates (see also the similar comments in connection with figure 31 above). In general the *a priori* standard deviations for the new model are noticeably larger, although this is exaggerated by the log scale. This is partly due to the inclusion of correlations – in the absence of correlations the daily total emissions will be relatively more constrained than the emissions from the individual source elements – but also because the individual source elements tend to have a lower *a priori* uncertainty in the old model as

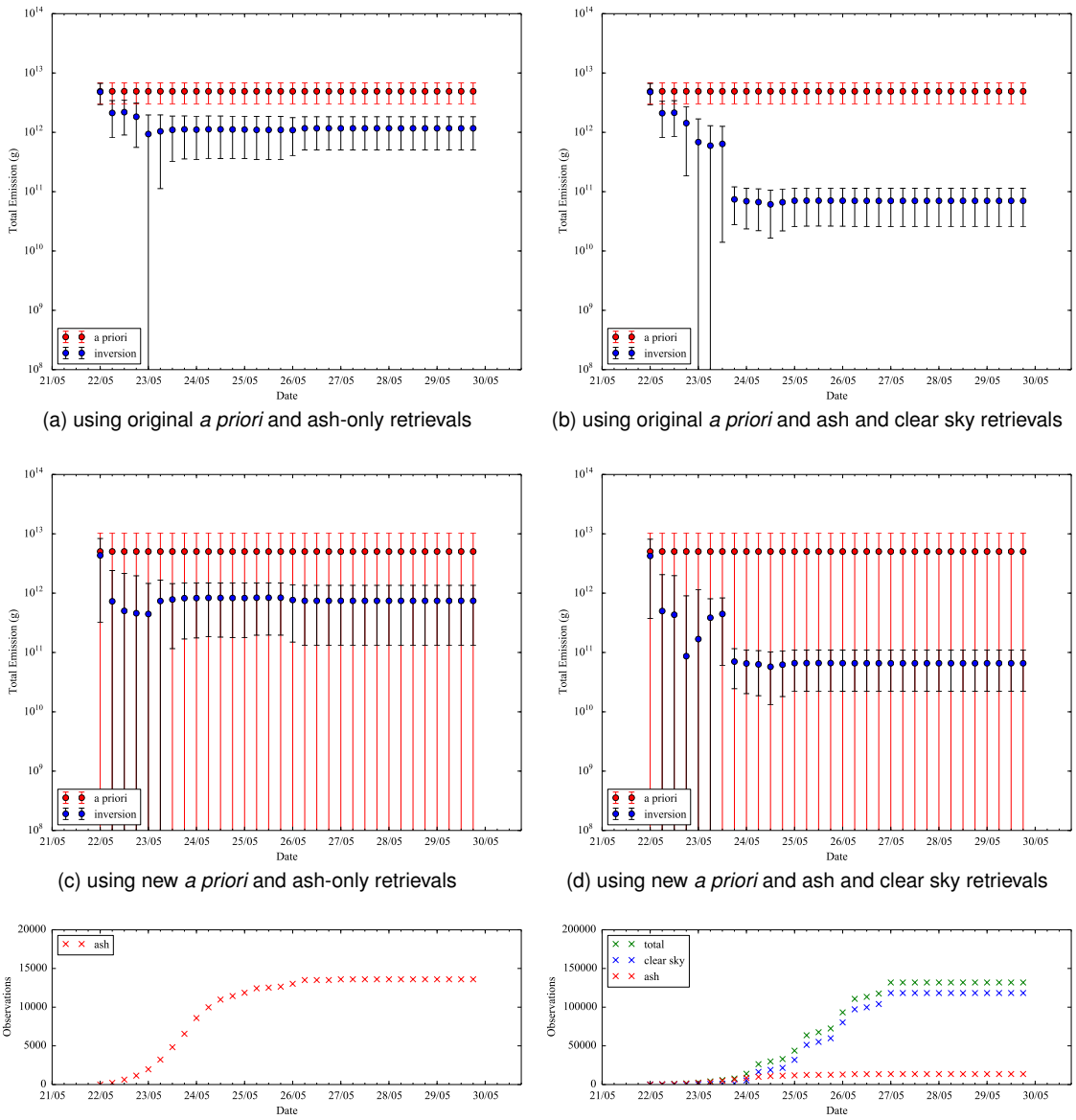

(a) using original *a priori* and ash-only retrievals

(b) using original *a priori* and ash and clear sky retrievals

(c) using new *a priori* and ash-only retrievals

(d) using new *a priori* and ash and clear sky retrievals

(e) cumulative number of ash-only observation uses

(f) cumulative number of observation uses

Figure 41: Estimated total emissions on 21/05/2011 for the Grímsvötn eruption, showing the changes in the estimates and their error bars as more observations become available over time. Results are shown using (a,b) the original and (c,d) the new *a priori* models and using (a,c) ash-only and (b,d) ash and clear sky satellite observations. (e) and (f) show the cumulative number of observation uses (see text for details of how this is defined). The NNLS solver is used throughout.

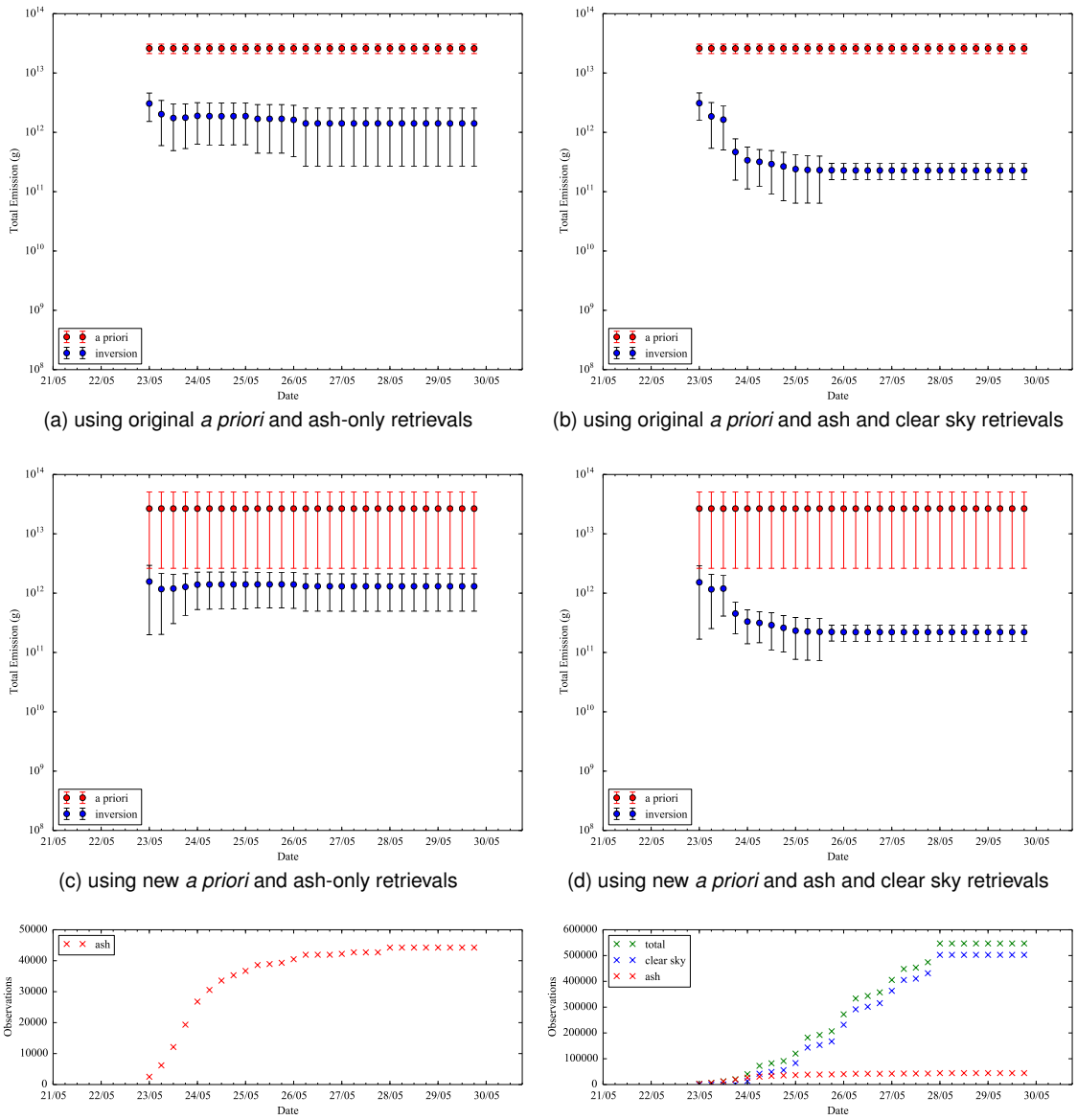

(a) using original *a priori* and ash-only retrievals

(b) using original *a priori* and ash and clear sky retrievals

(c) using new *a priori* and ash-only retrievals

(d) using new *a priori* and ash and clear sky retrievals

(e) cumulative number of ash-only observation uses

(f) cumulative number of observation uses

Figure 42: Estimated total emissions on 22/05/2011 for the Grímsvötn eruption, showing the changes in the estimates and their error bars as more observations become available over time. Results are shown using (a,b) the original and (c,d) the new *a priori* models and using (a,c) ash-only and (b,d) ash and clear sky satellite observations. (e) and (f) show the cumulative number of observation uses (see text for details of how this is defined). The NNLS solver is used throughout.

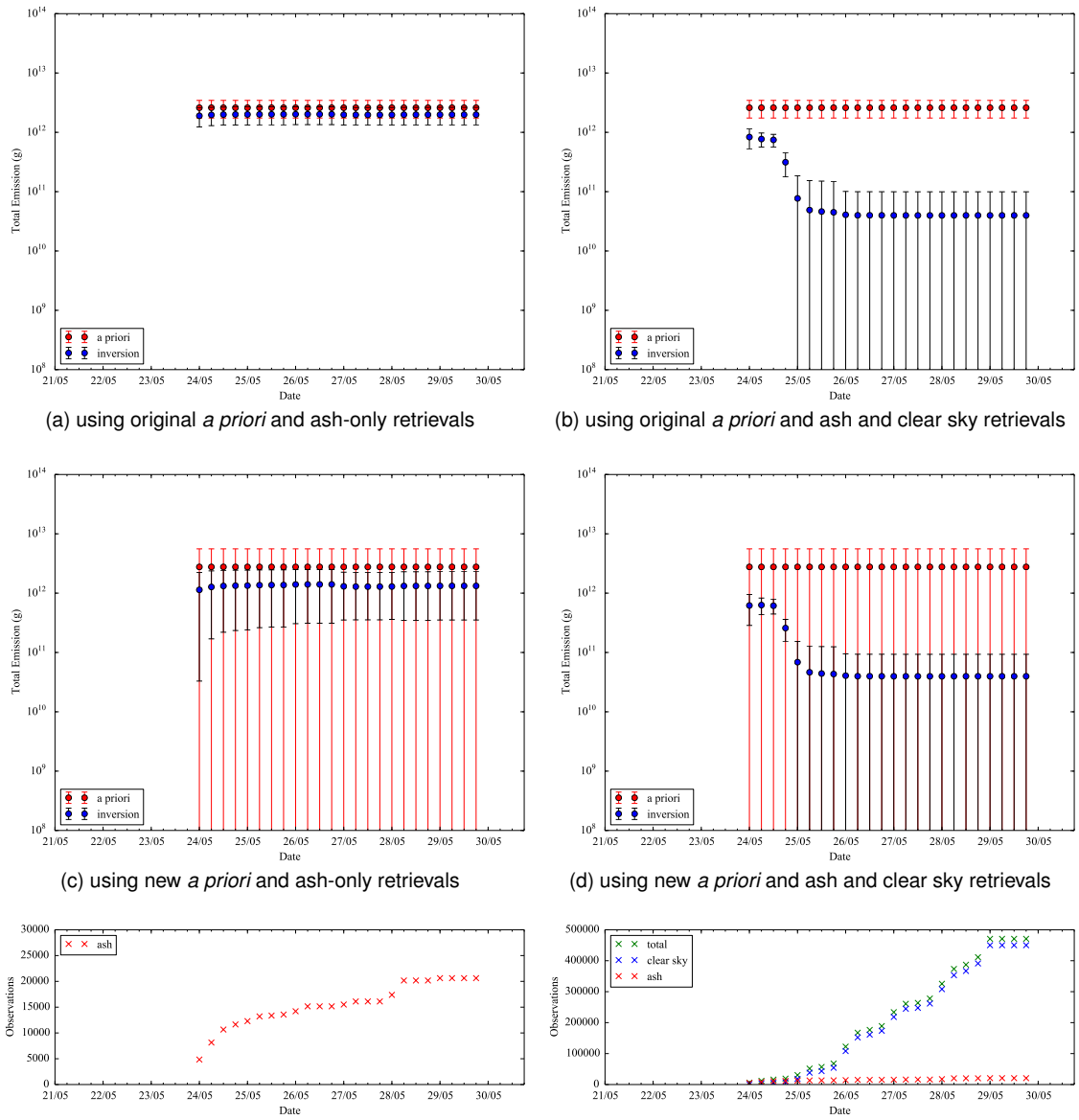

(a) using original *a priori* and ash-only retrievals

(b) using original *a priori* and ash and clear sky retrievals

(c) using new *a priori* and ash-only retrievals

(d) using new *a priori* and ash and clear sky retrievals

(e) cumulative number of ash-only observation uses

(f) cumulative number of observation uses

Figure 43: Estimated total emissions on 23/05/2011 for the Grímsvötn eruption, showing the changes in the estimates and their error bars as more observations become available over time. Results are shown using (a,b) the original and (c,d) the new *a priori* models and using (a,c) ash-only and (b,d) ash and clear sky satellite observations. (e) and (f) show the cumulative number of observation uses (see text for details of how this is defined). The NNLS solver is used throughout.

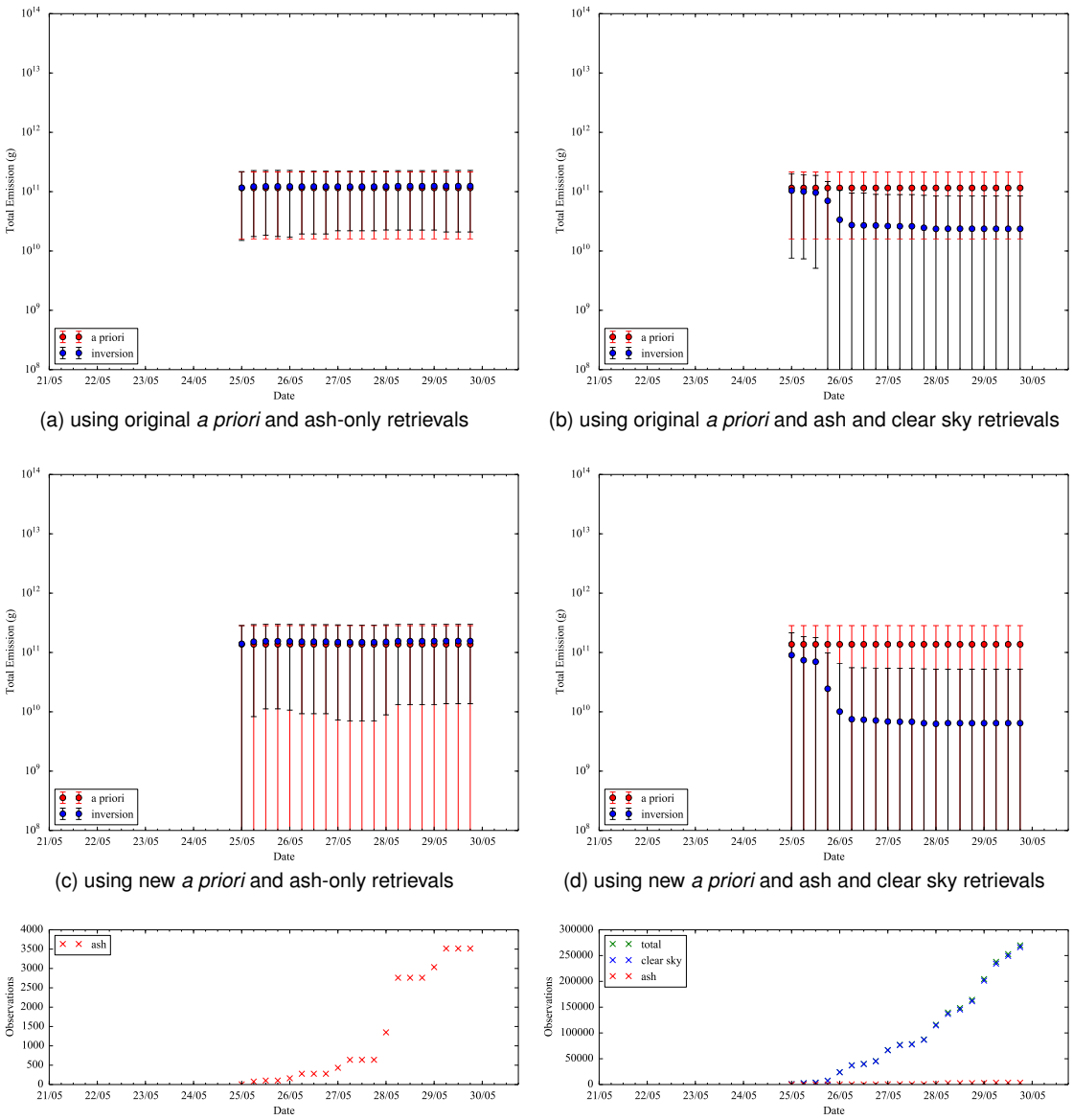

(a) using original *a priori* and ash-only retrievals

(b) using original *a priori* and ash and clear sky retrievals

(c) using new *a priori* and ash-only retrievals

(d) using new *a priori* and ash and clear sky retrievals

(e) cumulative number of ash-only observation uses

(f) cumulative number of observation uses

Figure 44: Estimated total emissions on 24/05/2011 for the Grímsvötn eruption, showing the changes in the estimates and their error bars as more observations become available over time. Results are shown using (a,b) the original and (c,d) the new *a priori* models and using (a,c) ash-only and (b,d) ash and clear sky satellite observations. (e) and (f) show the cumulative number of observation uses (see text for details of how this is defined). The NNLS solver is used throughout.

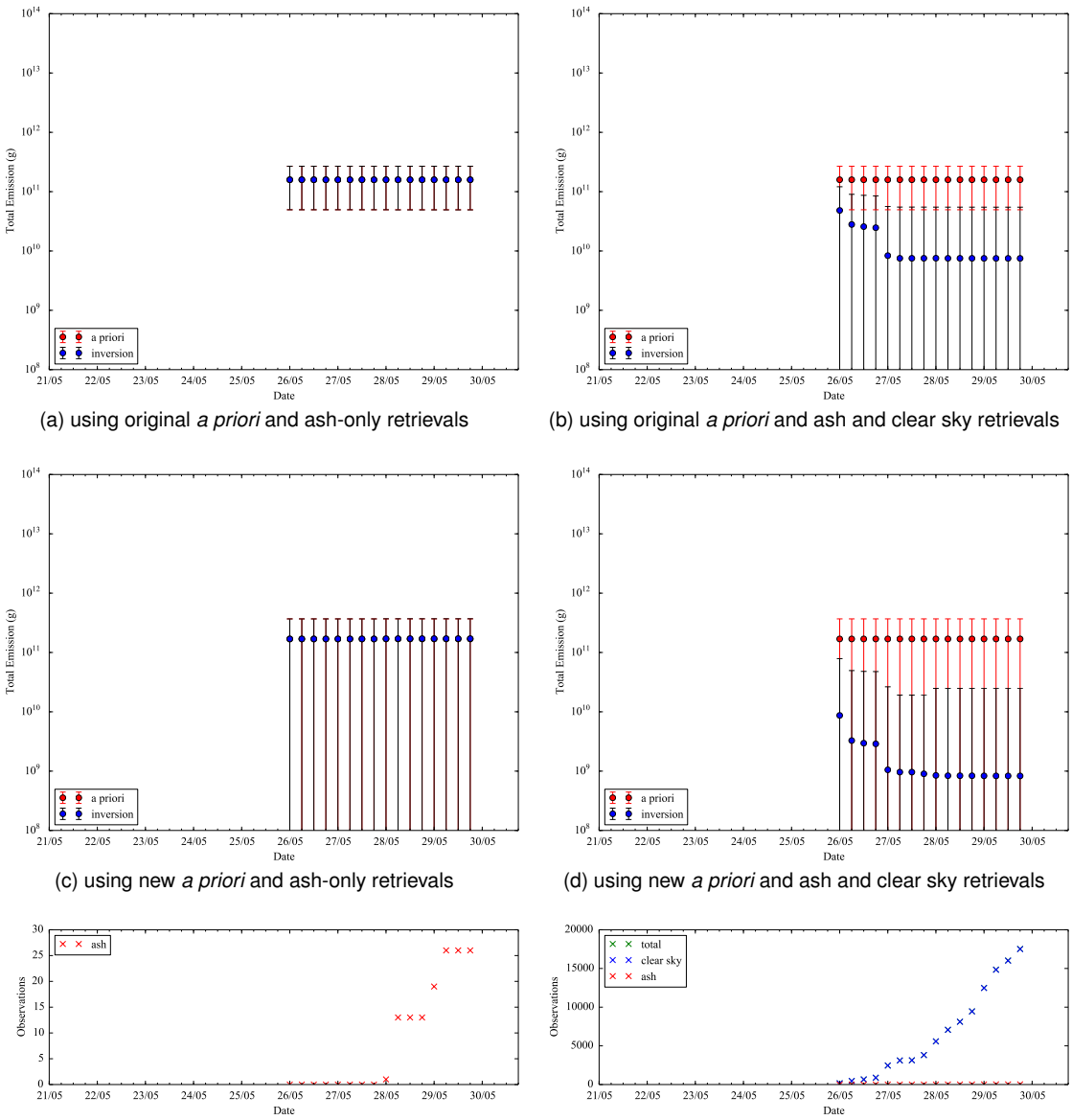

(a) using original *a priori* and ash-only retrievals

(b) using original *a priori* and ash and clear sky retrievals

(c) using new *a priori* and ash-only retrievals

(d) using new *a priori* and ash and clear sky retrievals

(e) cumulative number of ash-only observation uses

(f) cumulative number of observation uses

Figure 45: Estimated total emissions on 25/05/2011 for the Grímsvötn eruption, showing the changes in the estimates and their error bars as more observations become available over time. Results are shown using (a,b) the original and (c,d) the new *a priori* models and using (a,c) ash-only and (b,d) ash and clear sky satellite observations. (e) and (f) show the cumulative number of observation uses (see text for details of how this is defined). The NNLS solver is used throughout.

a consequence of the use of an extreme percentile (99.99%) in equation (13) of [5]. The parameters of the new model are no doubt not optimal but they appear to work reasonably well and there is little reason to try to tune them more precisely using just one or two eruptions.

7 Validation against observations of peak ash concentrations from the 2010 eruption of Eyjafjallajökull

A large number of observations were collected during the 2010 Eyjafjallajökull eruption and a subset of these were used by Webster et al. [8] to validate a method for predicting peak ash concentrations. The observations dataset used for validation consisted of ground-based measurements obtained using lidars and sunphotometers, airborne measurements from instrumentation on board research aircraft and a balloon ascent. The dataset was thought to represent local peak ash concentrations but has limitations and is acknowledged to be biased in it's sampling (space-time) locations (see [8] for a discussion of this). The ash concentration measurements were thought to be, in the main, within a factor of 2 of the true value. Various methods of forecasting peak ash concentrations were trialled by Webster et al. [8], including using model predicted ash concentrations over deep vertical layers (FL000 to FL200, FL200 to FL350 and FL350 to FL550, where FL indicates the flight level which is approximately equivalent to height in hundreds of feet but is defined in pressure), over thinner layers (of thickness 25FL) and a hybrid scheme which calculated the maximum of the predicted ash concentrations in the thin layers within the deep layers. It was assumed that 5% of the erupted volcanic ash consisted of fine ash particles that had diameters of less than 100 μm, that survived near source fall out, and that were transported into the distal ash cloud. A peak-to-mean factor was used to estimate peak ash concentrations from the mean ash concentrations predicted by the model. A peak-to-mean ratio of 20 was assumed for the deep layer case and 10 for the thin layer and hybrid cases. The percentage of model predictions within a factor of two of the observations were assessed to be "in agreement". An attempt was made to account for positional errors in the predicted ash cloud, which may be due to errors in the driving meteorological data, by considering the variability in the model ash concentrations over nearby output gridboxes. The variability across grid boxes up to two grid-boxes away in each horizontal direction (40 km resolution) and, for the 25FL layer scheme only, one grid-box up or down in the vertical direction (25FL resolution) was considered. Agreement is said to occur if the uncertainty ranges for the model prediction and the observation overlap. Webster et al. [8] assessed various source profiles, including a uniform source profile used operationally and a source profile derived by Kristiansen et al. [2] using an inversion method similar to that described here. For further information see Webster et al. [8].

NAME predictions of peak ash concentrations were obtained from the emission estimates presented in figures 37 and 39 (but with a slightly later data cut-off time of 06:00 UTC 31/05/2010). These emission estimates were derived using the InTEM inversion scheme with the NNLS solver and the new *a priori* model which includes cross correlations. The peak concentration predictions were obtained from the emissions using the same methods as used by Webster et al. [8] (the deep layer, 25FL layer and hybrid methods) with, in particular, the same assumed peak-to-mean ratios (20, 10 and 10 for the three methods). The results are validated against the same observation dataset as used by Webster et al. [8]. Note that these observations have not been used in the in-

version calculations. Figure 46 shows scatter plots of modelled versus observed values and table 5 shows the percentage of model values which are overpredicted, underpredicted and in agreement with the observations. Table 5 includes information on the geometric mean bias and the geometric standard deviation. These are defined as $\exp(\mu)$ and $\exp(\sigma)$ where μ and σ are the mean and standard deviation of the error in $\log_e(\max(\text{concentration}, 20\ \mu\text{g/m}^3))$. The limiting value of 20 μg/m^3 is used following [8] to avoid problems with noise at low concentrations.

Observations used in inversion	Model scheme	% in agreement	% of over predictions	% of under predictions	Geometric mean bias	Geometric s.d.
Ash only	Deep layer	47* 68†	31* 17†	22* 15†	1.06	3.77
	25FL layer	43* 79†	25* 3†	32* 18†	0.82	3.96
	Hybrid	40* 69†	38* 18†	23* 13†	1.17	3.82
Ash and clear sky	Deep layer	44* 58†	8* 4†	48* 38†	0.51	3.44
	25FL layer	36* 61†	7* 1†	57* 38†	0.44	3.55
	Hybrid	44* 61†	13* 6†	43* 33†	0.59	3.61

Table 5: Statistical comparison between modelled and observed peak concentrations with the model values calculated using emissions obtained using the inversion code with the new *a priori* model [7] and the NNLS solver. * indicates agreement assessed using a factor of 2 uncertainty in the observations but no model uncertainty. † indicates agreement assessed using uncertainty in both the observations and in the model predictions. The considered uncertainty in the model predictions is that due to positional errors in the ash cloud and is assessed as in [8]. Results are shown with model values calculated using emissions derived from ash-only observations and emissions derived from both ash and clear sky observations, and using the deep layer, 25FL layer and hybrid schemes.

We first discuss the results obtained using ash-only observations. If we do not try to account for errors in plume position, then the percentage of values 'in agreement' is substantially improved relative to that found by Webster et al. [8, figure 5 and table 3] without using an inversion model. The deep layer and 25FL layer methods show an improvement in bias with there now being less tendency to underpredict, while the hybrid method shows little change in this regard. There is also an improvement in scatter (for all three methods). This is not especially obvious from figure 46 because of the large scatter, but it is reflected in table 5 in the geometric mean bias being now closer to 1 (except for the hybrid method which shows little change) and the geometric standard deviations being smaller. This can also be seen from the dot-dashed lines in the figures. The general improvement in bias and the reduction in the tendency to underpredict could of course also have been obtained by increasing the peak-to-mean ratio assumed. However the large peak-to-mean ratio adopted in [8] is likely to be partly due to the model ash being too widely spread as a result of the ash being released with a wide spread in the vertical at the source. This vertical

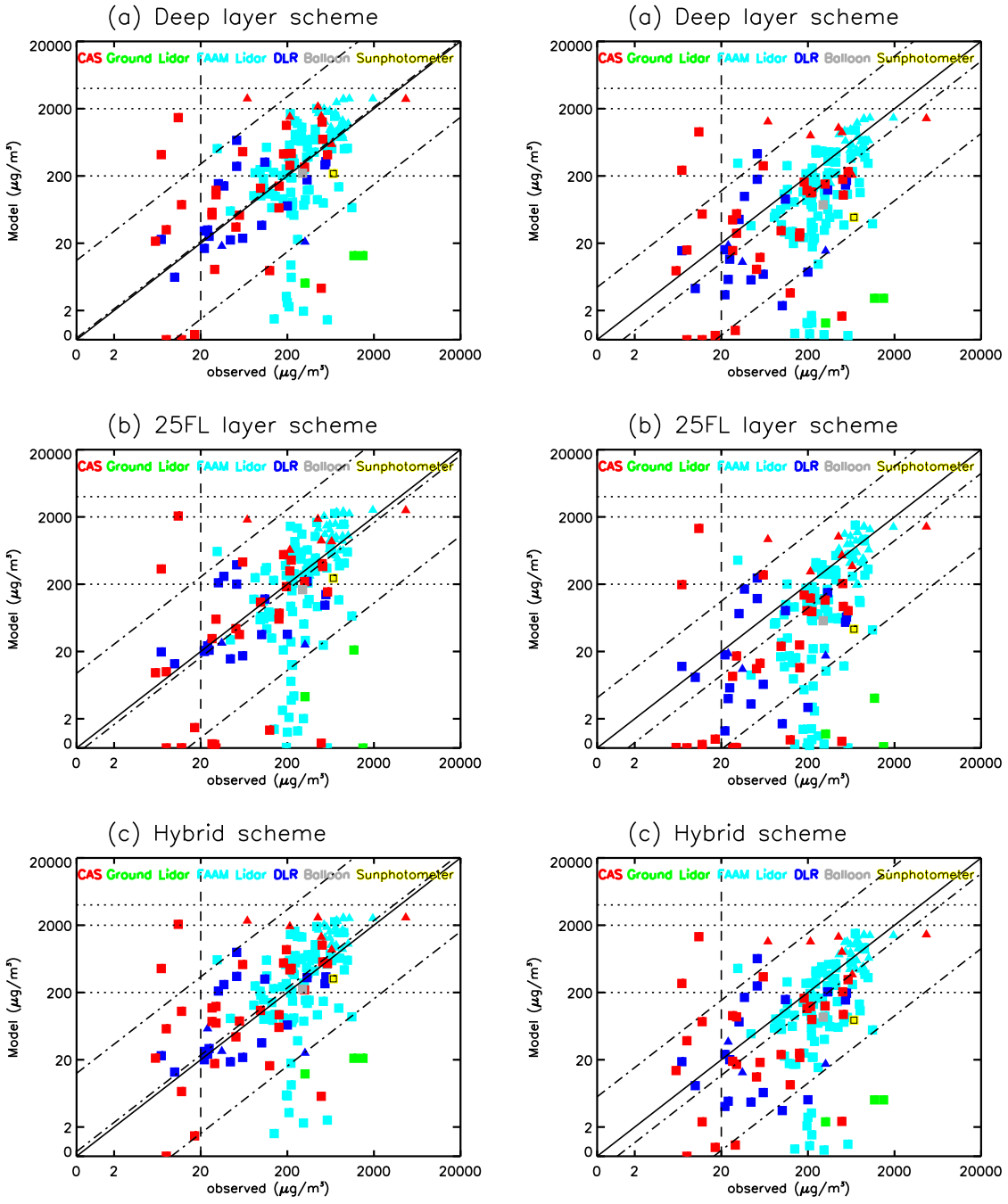

(i) ash-only observations

(ii) ash and clear skies observations

Figure 46: Modelled peak concentrations versus observed peak concentrations, with the model values calculated using emissions obtained using the inversion code with the new *a priori* model [7] and the NNLS solver. The shape of the symbol denotes observations at different heights (squares denote observations below flight level (FL) 200 and triangles denote observations between FL200 and FL350) and the colour denotes the observation type. Results are shown with model values calculated using (i) emissions derived from ash-only observations and (ii) emissions derived from both ash and clear sky observations, and using the (a) deep layer, (b) 25FL layer and (c) hybrid schemes. The vertical dashed line shows the value below which confidence in the CAS observations is low, the horizontal dotted lines show certain concentration thresholds used by aviation, and the diagonal dot-dashed lines show the geometric mean bias and the geometric mean bias plus or minus two standard deviations. These plots follow the format used in [8] and are described in more detail there.

spread at the source both dilutes the ash at the source and interacts with changes in wind direction with height to increase the subsequent ash cloud spread in the horizontal. Hence the fact that the inversion improves the tendency to underpredict without increasing the peak-to-mean ratio is a good thing. In fact the *a posteriori* estimate of the total emitted (effective) mass for the whole eruption, 1.12×10^{13} g, has decreased significantly from the *a priori* estimate, 1.85×10^{13} g (which is identical to the value used in the figure 5 and table 3 results of [8]). The combination of the reduction in mass emitted and the reduction in the tendency to underpredict suggests that the height-time distribution of the emissions has been improved by the inversion, with a tendency to focus the emissions at the right heights and times as well as adjusting the emission magnitudes. This is likely to have reduced any overpredictions outside the actual plume, but any such overpredictions and their reduction are unlikely to be fully reflected in the previous results of [8] and in the new results in figure 46 and table 5 because the measurement locations tend to be biased to be within the plume. When we include an allowance for errors in plume position, the percentage of values in agreement again improves relative to the percentage in agreement without using an inversion model [8, table 3].

We now consider the results obtained using both ash and clear sky observations. The geometric standard deviation decreases further, but the inversion results show quite a strong tendency to underpredict with a worse geometric mean bias than both the ash-only inversion results and the results without inversion modelling in [8, table 3]. The geometric error (calculated as $\exp(\sqrt{\sigma^2 + \mu^2})$) actually increases relative to the ash-only results (although it is lower than the value without inversion modelling calculated from [8, table 3]). While this bias could be corrected by increasing the assumed peak-to-mean factor, this seems a little undesirable because we expect that a more correct source shape should lead to a lower optimal peak-to-mean ratio as a result of the emitted ash being more focused in the correct regions. It seems possible that errors in the position of the modelled plume are leading to the plume intersecting more clear sky satellite observations than it should, with the result that the emissions are being reduced too much. The total emission using both ash and clear sky observations is estimated as 4.86×10^{12} g. While the reduction in the geometric standard deviation is encouraging, it is not clear on the basis of this set of data for just one eruption whether the use of clear sky observations in the way they have been used here will be beneficial in general. It seems likely however that benefits would be obtained if an approach to allow for errors in plume position (arising from errors in meteorology) was added to the inversion approach. This is a significant challenge but could perhaps be achieved by using ensembles of meteorological predictions and/or by adjusting the modelled concentration field (in addition to adjusting the source properties).

Although the above idea that the clear sky satellite data can interact with errors in plume position to remove too much material is very plausible, it is hard to give clear evidence for this. This is because the inclusion of a satellite observation in the inversion can affect the plume predictions at times and locations well away from the observation. However there is an example from the Grímsvötn eruption which provides some limited support. Figure 47a shows satellite retrievals of ash to the north of Norway and the north-west of Scotland, and figure 47b shows that the ash cloud

simulated with the *a priori* emissions transports ash to the vicinity of these observations. However the plumes near these locations are narrow and the modelled plumes are predicted to be a little to the north of the satellite retrievals of ash near Norway and a little to the south of the satellite retrievals of ash near Scotland. When the inversion is performed with ash-only retrievals (see figure 47c) the plume is present near both locations (although arguably too weak). However when the inversion uses both ash and clear sky retrievals (figure 47d) the plume to the north of Norway is all but completely removed and the plume to the north-west of Scotland is greatly weakened.

It seems possible that the simulated plume near Norway, being a little too far north, is intersecting the clear sky observations and so is being reduced too much. However, while this gives an apparently consistent picture, it is hard to have a lot of confidence in the retrievals near Norway because the satellite observations are so far north and the retrievals are from a geostationary satellite. In particular there is little sign of the ash in retrievals at other nearby times and it is possible that the ash near Norway in figure 47a is a false detection.

There are no clear sky retrievals near the plume near Scotland at the time plotted. However from about 08:00 UTC on 24/05/2011 the satellite retrievals show the ash moving from an area to the north of Scotland across the North Sea with clear skies to the south (see figure 47e). The *a priori* plume however remains slightly too far south and intersects the clear sky data (see figure 47f). It seems likely that this is why the plume from the inversion model is greatly weakened.

Scatter plots and statistics similar to those in figure 46 and table 5 were produced for a higher resolution source inversion, where the source resolution was 1 km in the vertical and 3 hours in time. Results were very similar to those presented here, with little sign of any improvement (or deterioration) in skill. While the lack of improvement is a little disappointing, there are many other possible causes of errors in the predictions which might be playing a more dominant role.

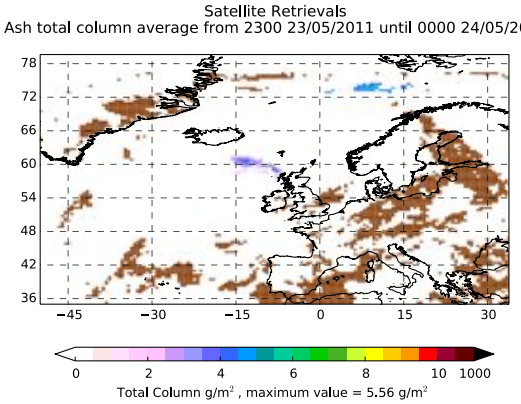

(a) ash and clear sky satellite retrievals
23:00 UTC 23/05/2011 to 00:00 UTC 24/05/2011

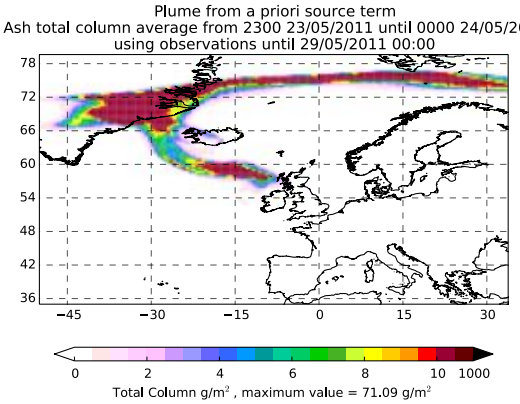

(b) *a priori* plume
23:00 UTC 23/05/2011 to 00:00 UTC 24/05/2011

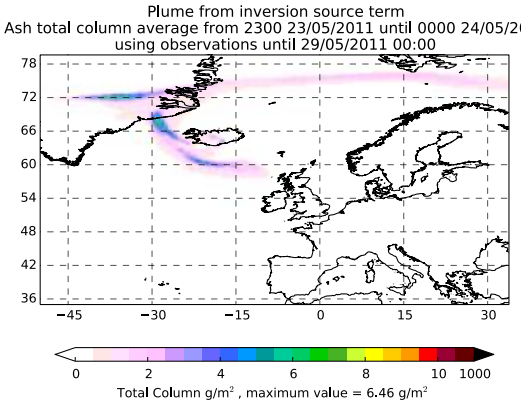

(c) *a posteriori* plume using ash-only retrievals
23:00 UTC 23/05/2011 to 00:00 UTC 24/05/2011

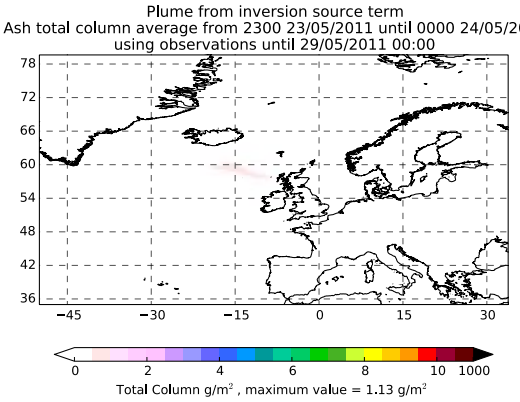

(d) *a posteriori* plume using ash and clear sky retrievals
23:00 UTC 23/05/2011 to 00:00 UTC 24/05/2011

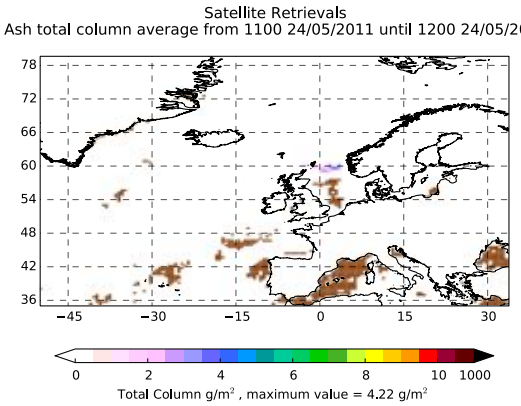

(e) ash and clear sky satellite retrievals
11:00 to 12:00 UTC 24/05/2011

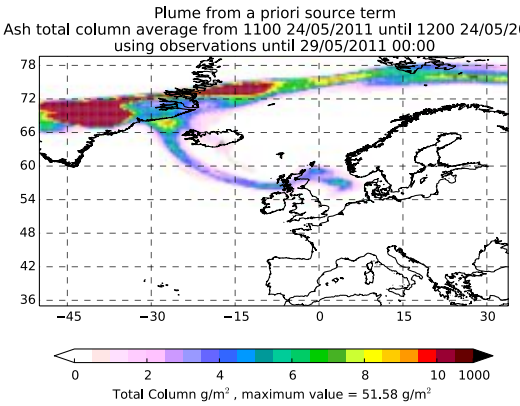

(f) *a priori* plume
11:00 to 12:00 UTC 24/05/2011

Figure 47: The Grímsvötn plume averaged between (a-d) 23:00 UTC on 23/05/2011 and 00:00 UTC on 24/05/2011 and (e-f) 11:00 and 12:00 UTC on 24/05/2011. (a,e) show the plume as observed by satellite (ash and clear skies, with clear skies shown in brown); (b,f) show the plume as predicted by NAME with *a priori* mean emissions from the new *a priori* model [7]; and (c-d) show the plume as predicted by NAME with emissions determined using (c) ash-only and (d) both ash and clear sky satellite observations, and using the inversion code with the new *a priori* model [7] and the NNLS solver. (c-d) use satellite retrievals up to 00:00 UTC 29/05/2011.

8 Conclusions

A series of tests have been conducted to assess the recent improvements which have been made to the inversion system for estimating emissions of volcanic ash. Results are obtained for the 2010 Eyjafjallajökull and 2011 Grímsvötn eruptions using (i) the method implemented in January 2015 using simulated annealing [5], (ii) a method which involved some pre-calculations before invoking the simulated annealing with the aim of reducing the cost of the calculations, (iii) a method using the Lawson and Hanson NNLS solver [3], and (iv) a method using NNLS but with a new *a priori* model for the eruption [7] which involves cross correlations between the *a priori* emissions from the various source elements. These tests all use an improved method of reducing the resolution of the satellite data to match the resolution of the NAME model.

The optimisation problems formulated in methods (i), (ii) and (iii) are mathematically equivalent. Hence the differences of interest concern the effectiveness of the algorithm in finding the true cost function minimum and the computational efficiency of the algorithm. The tests revealed that the simulated annealing approaches (methods (i) and (ii)) sometimes did not converge very closely to the true cost function minimum. This could result in significantly different results being obtained when there were minor inconsequential changes to the inputs to the optimisation problem. The use of the NNLS solver in method (iii) gives generally similar results to the simulated annealing methods, with any differences probably associated with the incomplete convergence of the simulated annealing. The most obvious difference is that where the simulated annealing gave small emissions the NNLS method often gives exactly zero. We believe this reflects the complete convergence which is possible with NNLS. Method (ii) shows some substantial differences in computational cost from method (i) but the effect can have either sign depending on the problem being addressed. The NNLS method (method (iii)) is however consistently faster than methods (i) and (ii), and often much faster.

Method (iv) introduces the new *a priori* model described in [7] with cross correlations between the emissions from the various source components. The differences from method (iii) are not large but there is some evidence that the inclusion of the cross correlations enables greater adjustments to the emissions to be made earlier when fewer observations are available. This is because a small number of observations can influence a larger number of source components. These early adjustments seem beneficial but it's hard to draw firm conclusions from data for just two eruptions. When more observations are available the differences are less marked. The introduction of cross correlations resulted in some increase in computational cost, but these increases were modest and the calculations were still much faster than methods (i) and (ii).

Method (iv) involves a number of parameters describing the errors in the *a priori* emissions, including the cross correlations between the emissions. Some tests of the sensitivity of the results to the values of these parameters have been carried out. The results show some significant sensitivity at early times when fewer observations are available but these differences get smaller as more

observations become available. The results do not provide any strong indications that could be used to tune the parameters and do not give us any reason to change the parameters from the defaults proposed.

Some tests of the statistical consistency between the assumptions and the available data were conducted. These consisted of looking at the estimated errors in the total emissions for each day of the Grímsvötn eruption and seeing if the estimates of emissions made using the observations available up to a certain time were broadly consistent with the earlier estimates (including *a priori* estimates) and their estimated errors. The results with the new *a priori* model showed an improvement in this type of consistency and were broadly consistent. It would be of interest to repeat these consistency tests for the Eyjafjallajökull eruption and also to consider emissions aggregated over different time and height ranges as well as the daily totals considered here. However to make definite conclusions would require data from many eruptions.

The predictions using the optimised emissions from method (iv) were validated by comparing the resulting plume predictions with a set of non-satellite measurements which had not been used in the inversion calculations. The measurements relate to the Eyjafjallajökull eruption and are described in [8]. Results using ash-only observations are encouraging and show some reduction in scatter. Also, despite the total emission being significantly reduced from the *a priori*, there is a reduction in the (slight) tendency to underpredict. This suggests that the emissions from the inversion calculation are more focused in the right parts of the time-height emission space. When clear sky observations are included the results are more mixed. Our measure of the scatter (the geometric standard deviation of the error) reduces further by a small amount, but there is an increased tendency to underpredict which may be due to removing too much ash, perhaps due to errors in the simulated plume position which lead to it intersecting the location of clear sky observations. While the reduction in scatter is encouraging it may be that a method of accounting for errors in the meteorology and/or dispersion is needed to enable the clear sky data to be used to best effect.

For method (iv), some limited tests of the effect of the source resolution were conducted. Emission profiles and plume predictions were examined for Grímsvötn 2011 with the resolution increased from 4 km in the vertical and 3 hours in time to 2 km and 1 hour. Some finer structure was seen in the source in response to the increased resolution, but, with the exception of some changes in maximum column loads, the overall effect on plume predictions was small. For Eyjafjallajökull 2010, the results obtained with an increase in source resolution from 4 km in the vertical and 3 hours in time to 1 km and 3 hours were validated against the measurements described in [8]. The change in source resolution made little difference to the results.

While the tests conducted here have been fairly comprehensive, there are a range of further tests that could be useful. For example, using different values for the (new) *a priori* model parameters in the consistency checks and in the validation study might be useful. This could include extreme choices which come close to eliminating (or strengthening) the cross correlations in order to increase understanding of the effect of the cross correlations. One could also extend the consis-

tency checks to quantities other than total daily emissions and further explore the effect of source resolution. However probably the most useful activity would be to test the scheme against a wider range of eruptions.

Appendices

A Convergence of the simulated annealing solver

Here we use the Grímsvötn 2011 eruption as an example to illustrate the incomplete convergence of the simulated annealing solver and to indicate the effect on the determined solution (the eruption emission profile). We compare two inversions using all satellite observations (both ash and clear skies) until 00:00 UTC on 31/05/2011 and until 06:00 UTC on 31/05/2011. There are no additional satellite observations used in the longer inversion and hence the determined solutions should be identical. All results presented here use the Pelley et al. [5] inversion code.

Figure 48 compares the source profiles from the two inversions. Despite many similarities, differences of two orders of magnitude do exist in places. The values of the cost function for the solutions are similar, but slightly different (see table 6).

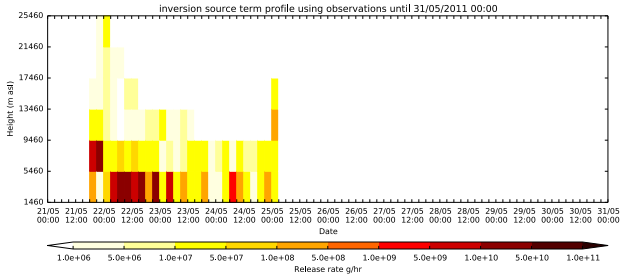

(a) emissions using satellite retrievals up to 00:00 UTC 31/05/2011

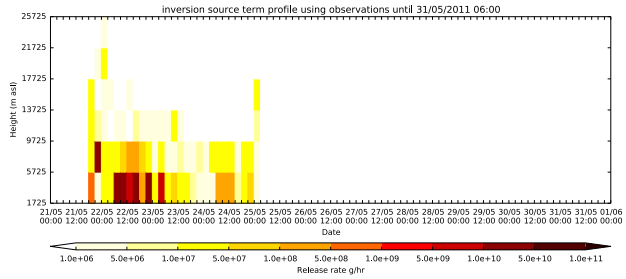

(b) emissions using satellite retrievals up to 06:00 UTC 31/05/2011

Figure 48: The best fit emission profile for the eruption of Grímsvötn using both ash and clear sky satellite observations. (Note the different scales used along the time axis.)

Last satellite observation time	Normalised cost function value
00:00 UTC 31/05/2011	0.00313428
06:00 UTC 31/05/2011	0.00313134

Table 6: The normalised cost function (normalised with number of observations) for the solutions determined using both ash and clear sky satellite observations until the time and date shown.

Figures 49a and 49b show the modelled plumes between 14:00 UTC and 15:00 UTC on 22/05/2011 using the source in figure 48, determined by the inversion scheme using satellite observations until 00:00 UTC and 06:00 UTC on 31/05/2011, respectively. Total ash column amounts over southern Iceland differ noticeably between the two plume predictions and this highlights the impact of the incomplete convergence of simulated annealing on the ash plume forecast.

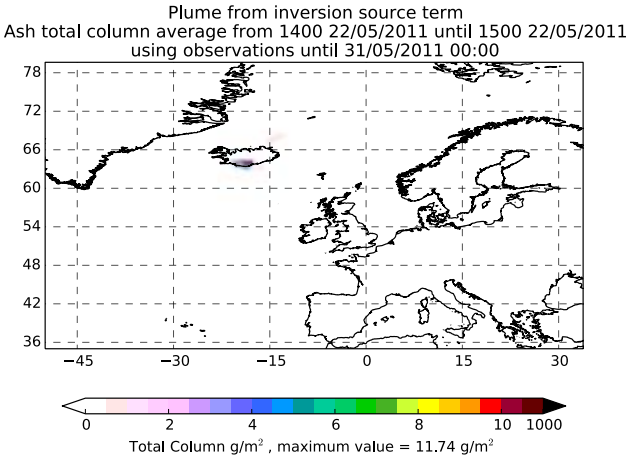

(a) plume using satellite retrievals up to 00:00 UTC 31/05/2011

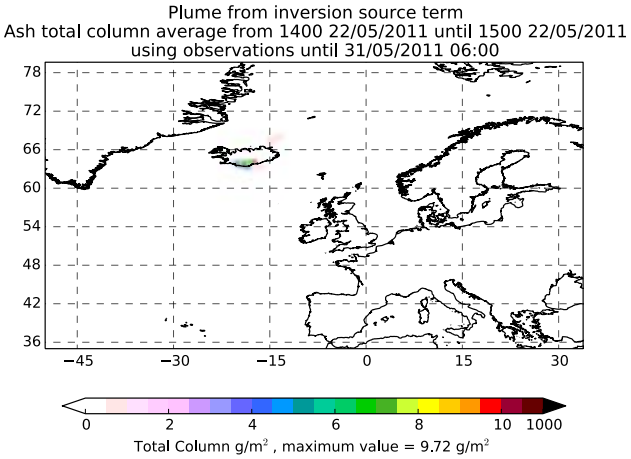

(b) plume using satellite retrievals up to 06:00 UTC 31/05/2011

Figure 49: The Grímsvötn plume averaged between 14:00 UTC and 15:00 UTC on 22/05/2011 as predicted by NAME with emissions determined using both ash and clear sky satellite observations.

B Sensitivity to the parameters affecting the *a priori* correlations in the *a priori* model

In the *a priori* model given in [7], there is considerable uncertainty in the parameters which govern the cross correlations between errors in the *a priori* source elements. Here we vary these parameters to illustrate the sensitivity of the inversion results to these parameters, using the Grímsvötn 2011 eruption as an example. All results presented here use this *a priori* model with the NNLS solver.

Figure 50 shows the *a priori* and *a posteriori* source profiles determined using ash-only observations until 12:00 UTC on 22/05/2011. The cross correlation parameters T_H, T_r, σ_r and T_q are varied from the default values of $T_H = T_r = 12$ hours, $\sigma_r = 1$ and $T_q = 3$ hours. The *a posteriori* source profiles are similar, although some subtle differences do exist for different cross correlation parameters. All the *a posteriori* source profiles are significantly different from the *a priori* mean source profile.

Figure 51 shows the modelled plumes between 05:00 and 06:00 UTC on 22/05/2011 obtained using the source profiles in figure 50, together with the corresponding satellite observations of ash for comparison. The predicted plumes obtained using the *a posteriori* source profiles are very similar to each other. However, the maximum value of the *a posteriori* ash column loads, presumably located at the volcano, varies within a factor of two. This variation is considerably less when later observations are included in the inversion (not shown) suggesting that the cross correlations have a greater impact when few observations are available. When the inversion problem is well constrained with a large number of observations, the cross correlations have less effect on the end result.

Figures 52 to 55 show the *a posteriori* source profiles and the corresponding modelled plumes between 23:00 UTC on 22/05/2011 and 00:00 UTC on 23/05/2011 using ash-only observations until 00:00 UTC on 23/05/2011 and until 00:00 UTC on 31/05/2011, for various choices of the cross correlation parameters. Note that these plots correspond to the Grímsvötn 2011 eruption examples presented in the main body of this technical note. In the main, the *a posteriori* source profiles and the predicted plumes for the various parameter values are similar but with a few subtle differences.

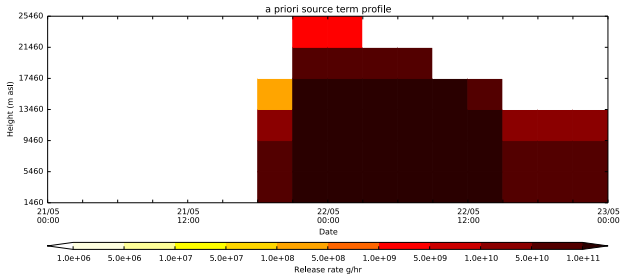

(a) *a priori*

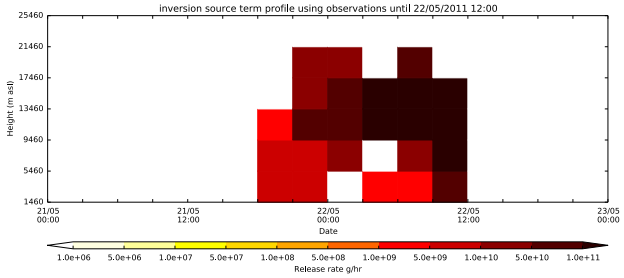

(b) *a posteriori*: $T_H = T_r = 12$ hrs, $\sigma_r = 1$, $T_q = 3$ hrs

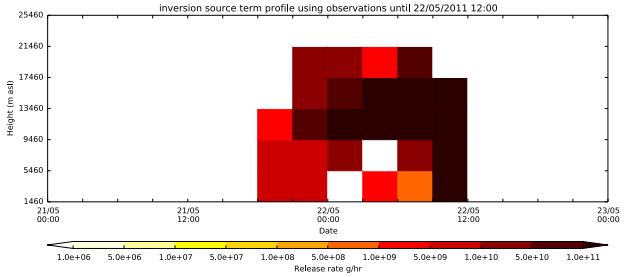

(c) *a posteriori*: $T_H = T_r = 3$ hrs, $\sigma_r = 1$, $T_q = 3$ hrs

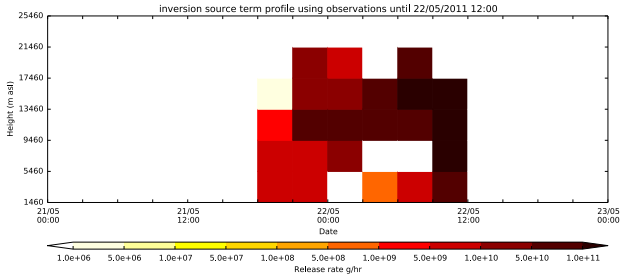

(d) *a posteriori*: $T_H = T_r = 12$ hrs, $\sigma_r = 2$, $T_q = 3$ hrs

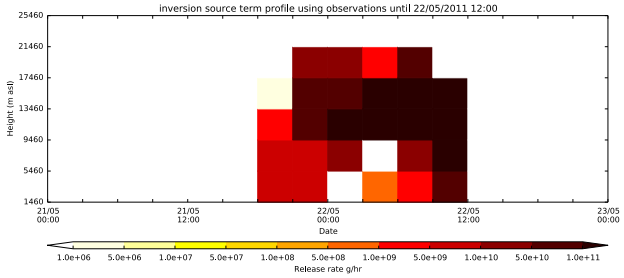

(e) *a posteriori*: $T_H = T_r = 12$ hrs, $\sigma_r = 1$, $T_q = 6$ hrs

Figure 50: The *a priori* emission profile for the Grímsvötn eruption and the *a posteriori* emission profiles obtained with various values for the cross correlation parameters T_H, T_r, σ_r and T_q. Ash-only satellite observations up to 12:00 UTC on 22/05/2011 are included in the inversions. Note the *a posteriori* emissions are not shown after the satellite data cut-off time of 12:00 UTC on 22/05/2011.

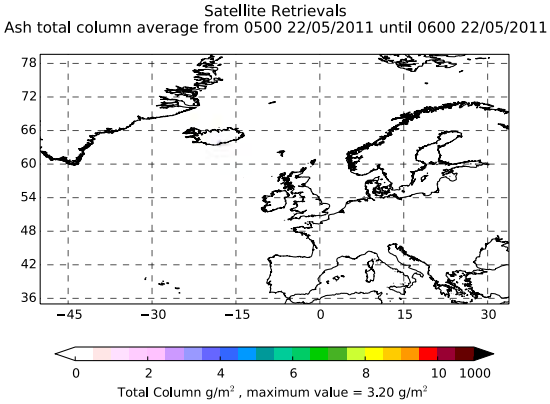

(a) ash-only satellite retrievals

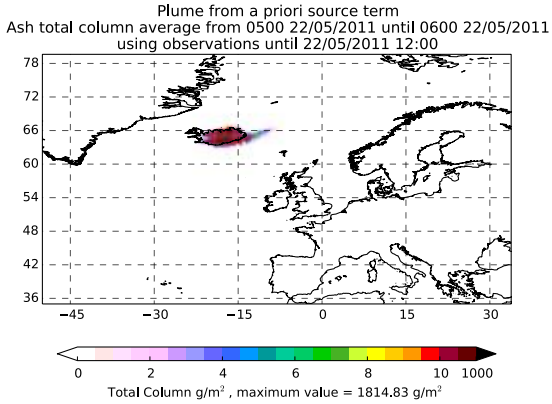

(b) *a priori*

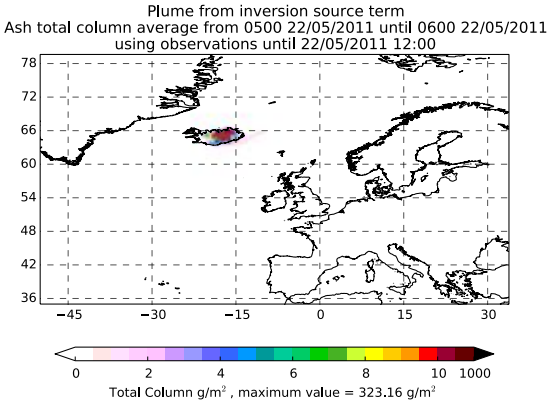

(c) *a posteriori*: $T_H = T_r = 12$ hrs, $\sigma_r = 1$, $T_q = 3$ hrs

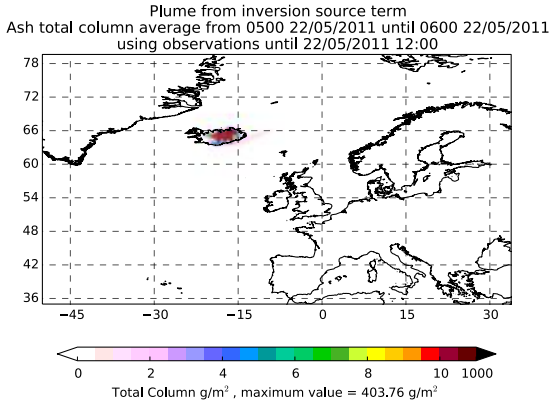

(d) *a posteriori*: $T_H = T_r = 3$ hrs, $\sigma_r = 1$, $T_q = 3$ hrs

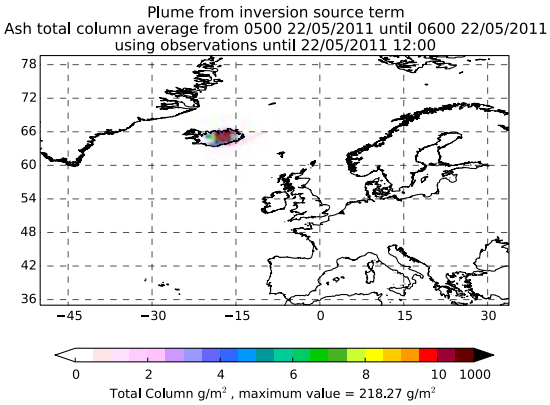

(e) *a posteriori*: $T_H = T_r = 12$ hrs, $\sigma_r = 2$, $T_q = 3$ hrs

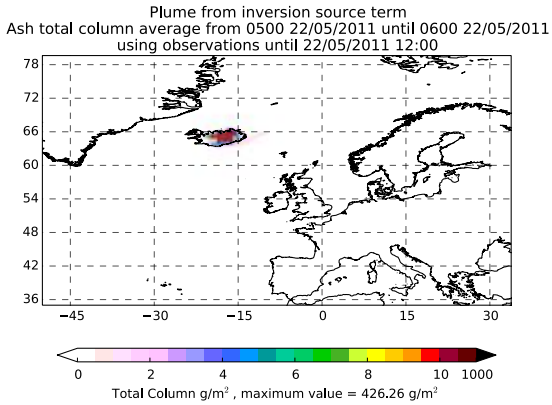

(f) *a posteriori*: $T_H = T_r = 12$ hrs, $\sigma_r = 1$, $T_q = 6$ hrs

Figure 51: The Grímsvötn plume averaged between 05:00 and 06:00 UTC on 22/05/2011: (a) as observed by satellite (ash only); (b) as predicted by NAME using the *a priori* emissions; and (c-f) as predicted by NAME using the *a posteriori* emissions obtained with various values for the cross correlation parameters T_H, T_r, σ_r and T_q. Ash-only satellite observations up to 12:00 UTC on 22/05/2011 are included in the inversions.

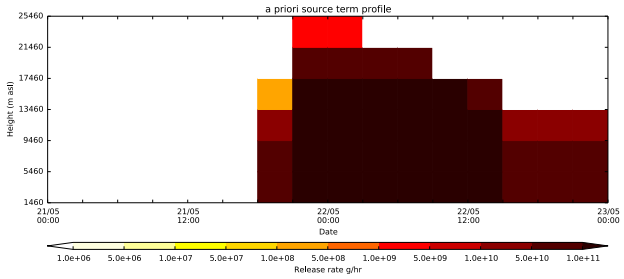

(a) *a priori*

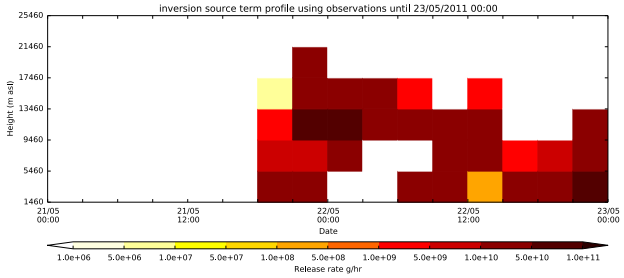

(b) *a posteriori*: $T_H = T_r = 12$ hrs, $\sigma_r = 1$, $T_q = 3$ hrs

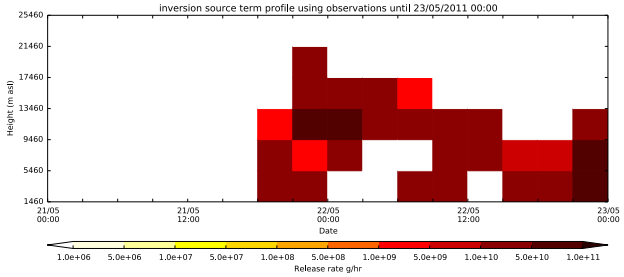

(c) *a posteriori*: $T_H = T_r = 3$ hrs, $\sigma_r = 1$, $T_q = 3$ hrs

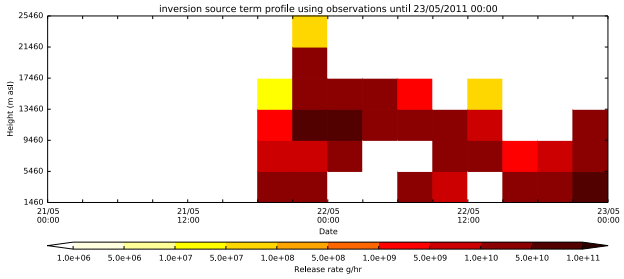

(d) *a posteriori*: $T_H = T_r = 12$ hrs, $\sigma_r = 2$, $T_q = 3$ hrs

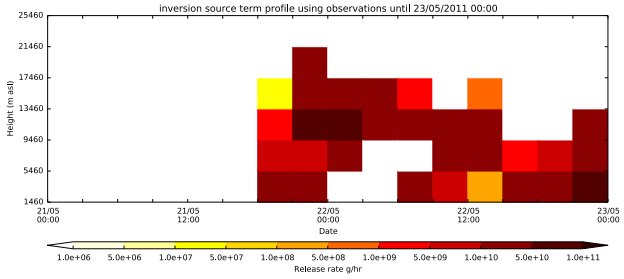

(e) *a posteriori*: $T_H = T_r = 12$ hrs, $\sigma_r = 1$, $T_q = 6$ hrs

Figure 52: The *a priori* emission profile for the Grímsvötn eruption and the *a posteriori* emission profiles obtained with various values for the cross correlation parameters T_H, T_r, σ_r and T_q. Ash-only satellite observations up to 00:00 UTC on 23/05/2011 are included in the inversions.

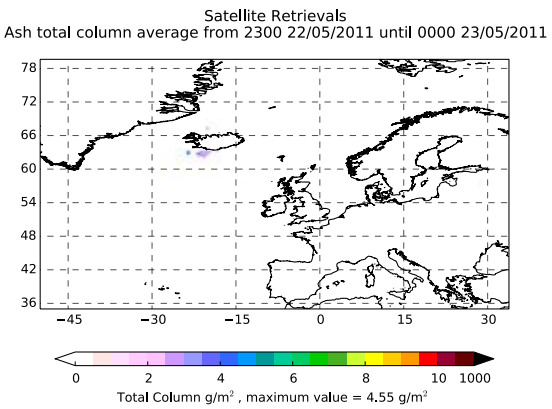

(a) ash-only satellite retrievals

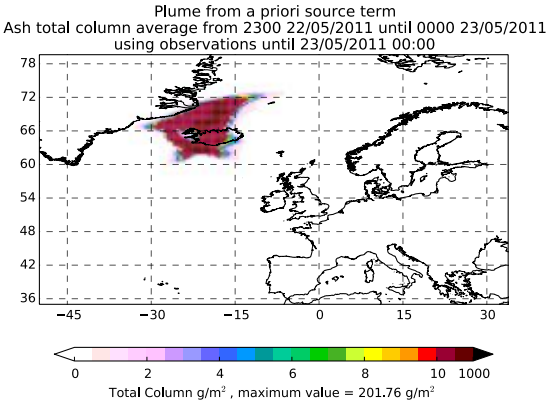

(b) *a priori*

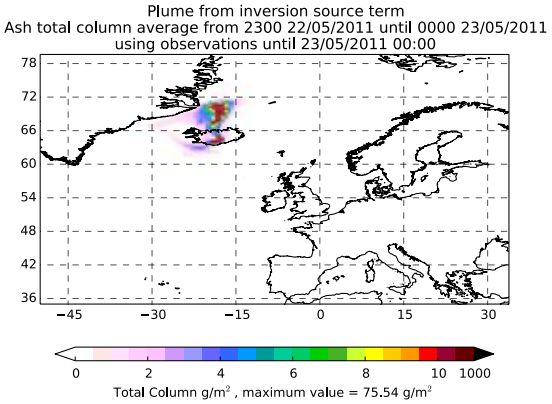

(c) *a posteriori*: $T_H = T_r = 12$ hrs, $\sigma_r = 1$, $T_q = 3$ hrs

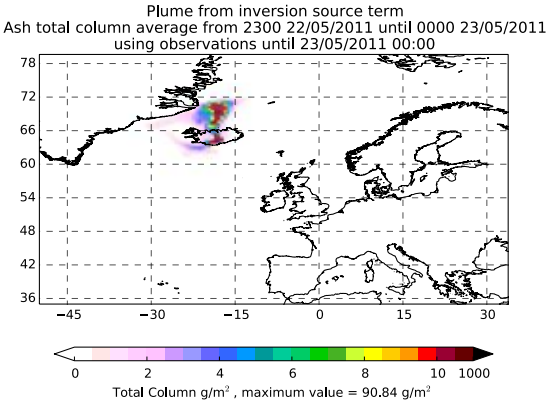

(d) *a posteriori*: $T_H = T_r = 3$ hrs, $\sigma_r = 1$, $T_q = 3$ hrs

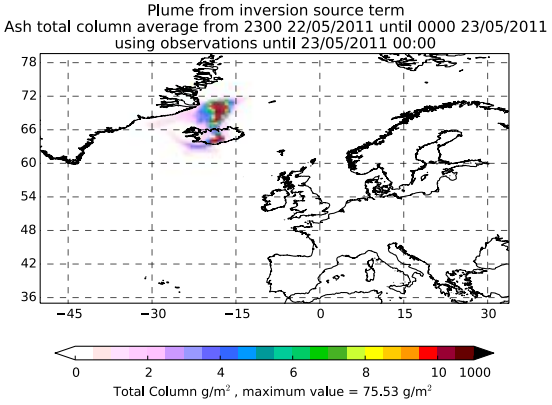

(e) *a posteriori*: $T_H = T_r = 12$ hrs, $\sigma_r = 2$, $T_q = 3$ hrs

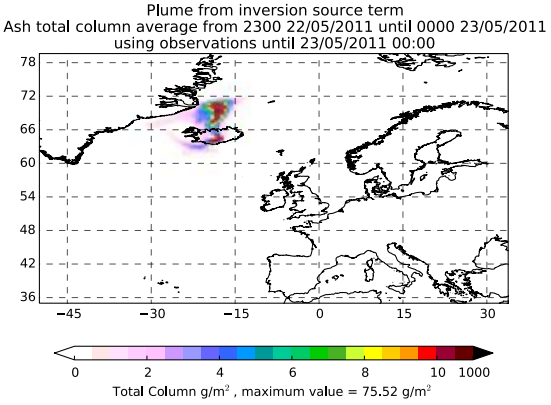

(f) *a posteriori*: $T_H = T_r = 12$ hrs, $\sigma_r = 1$, $T_q = 6$ hrs

Figure 53: The Grímsvötn plume averaged between 23:00 UTC on 22/05/2011 and 00:00 UTC on 23/05/2011: (a) as observed by satellite (ash only); (b) as predicted by NAME using the *a priori* emissions; and (c-f) as predicted by NAME using the *a posteriori* emissions obtained with various values for the cross correlation parameters T_H, T_r, σ_r and T_q. Ash-only satellite observations up to 00:00 UTC on 23/05/2011 are included in the inversions.

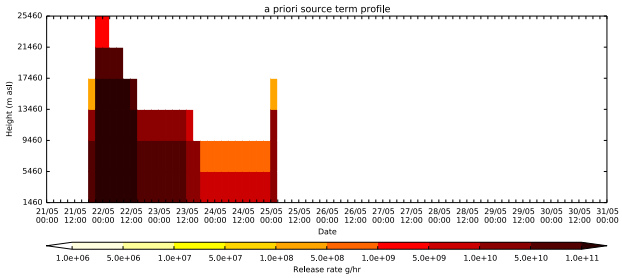

(a) *a priori*

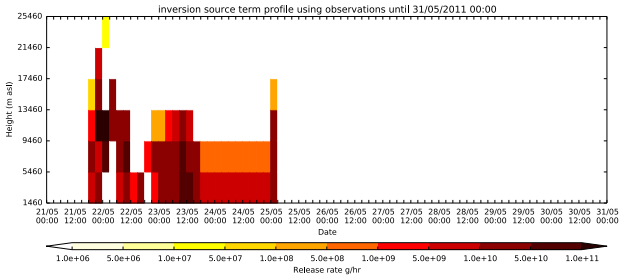

(b) *a posteriori*: $T_H = T_r = 12$ hrs, $\sigma_r = 1$, $T_q = 3$ hrs

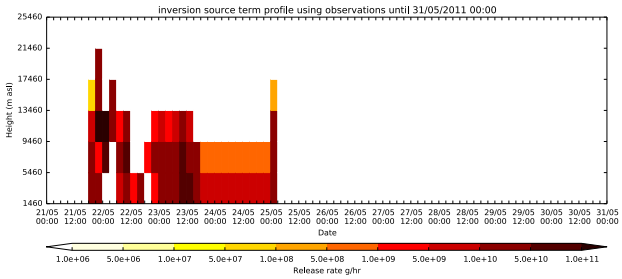

(c) *a posteriori*: $T_H = T_r = 3$ hrs, $\sigma_r = 1$, $T_q = 3$ hrs

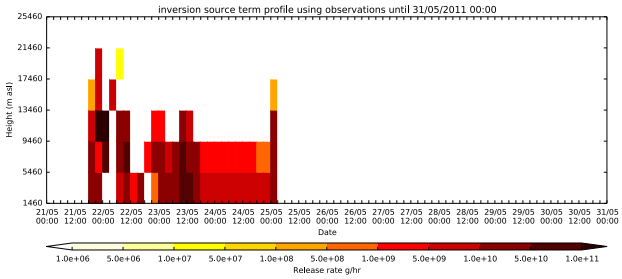

(d) *a posteriori*: $T_H = T_r = 12$ hrs, $\sigma_r = 2$, $T_q = 3$ hrs

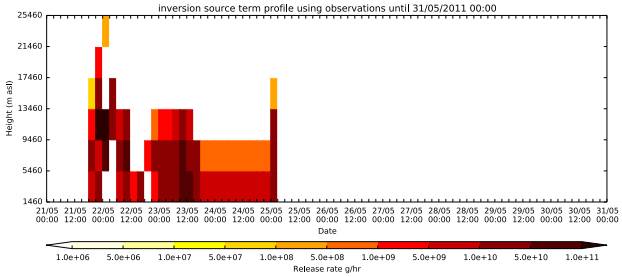

(e) *a posteriori*: $T_H = T_r = 12$ hrs, $\sigma_r = 1$, $T_q = 6$ hrs

Figure 54: As figure 52 but using ash-only satellite observations up to 00:00 UTC on 31/05/2011 in the inversion calculations.

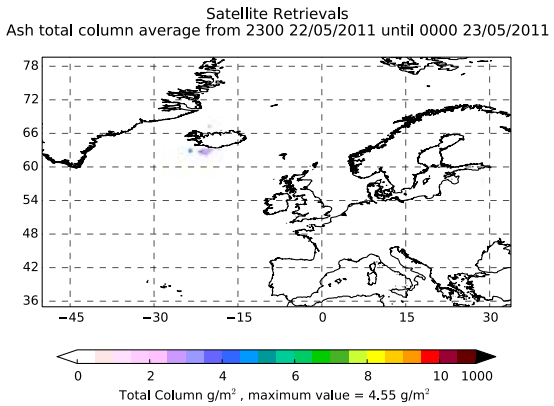

(a) ash-only satellite retrievals

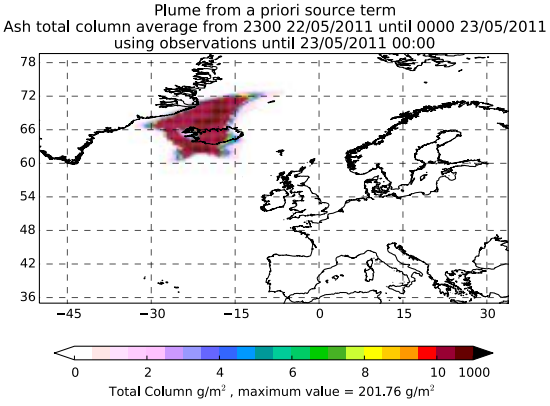

(b) *a priori*

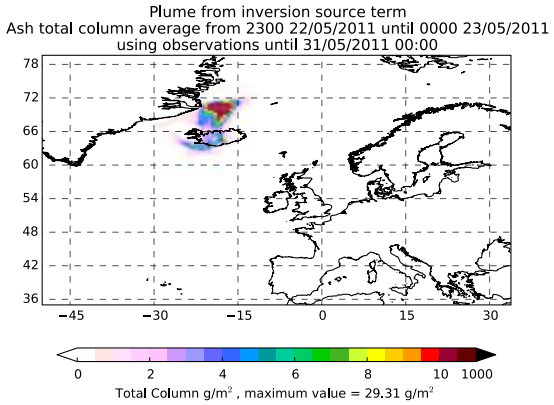

(c) *a posteriori*: $T_H = T_r = 12$ hrs, $\sigma_r = 1$, $T_q = 3$ hrs

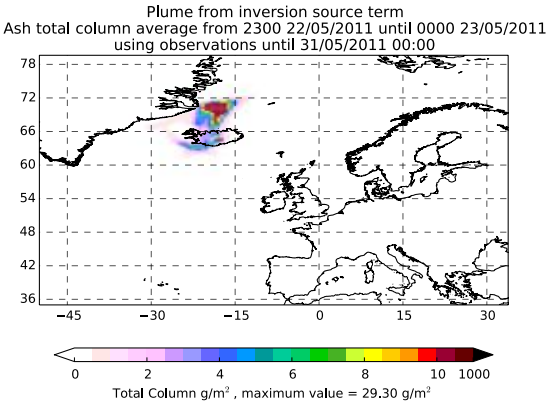

(d) *a posteriori*: $T_H = T_r = 3$ hrs, $\sigma_r = 1$, $T_q = 3$ hrs

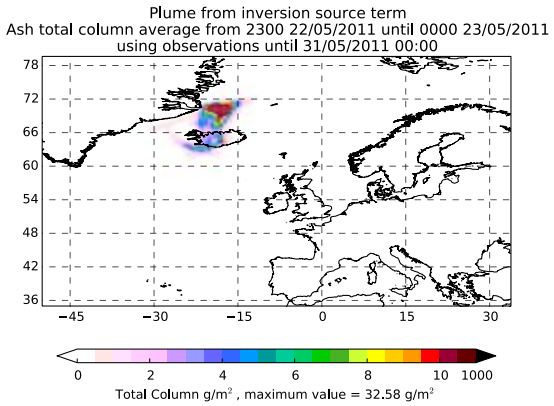

(e) *a posteriori*: $T_H = T_r = 12$ hrs, $\sigma_r = 2$, $T_q = 3$ hrs

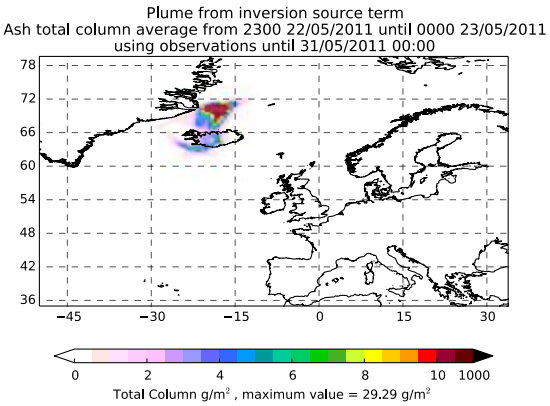

(f) *a posteriori*: $T_H = T_r = 12$ hrs, $\sigma_r = 1$, $T_q = 6$ hrs

Figure 55: As figure 53 but using ash-only satellite observations up to 00:00 UTC on 31/05/2011 in the inversion calculations.

C Increasing the inversion source term resolution

The speed-up in the run-time of the inversion code, obtained using the Lawson and Hanson NNLS solver [3], allows us to consider increasing the resolution of the source both spatially, i.e. in the vertical, and in time, from the default values of 4 km and 3 hours. The current vertical resolution of 4 km is coarse, particularly for small eruptions. Here we investigate increasing the resolution of the source to 2 km in the vertical and 1 hour in time. In performing the NAME runs to determine the transport matrix, $\mathbf{M}$, it was necessary to reduce the number of model particles released per source over one hour for computational memory reasons. This is also useful to keep the run time manageable. Choosing the number of model particles is clearly a balancing game, with enough required to adequately simulate dispersion from each source component but not so many that the run-time and memory requirements become prohibitive. The memory requirement problem could be solved of course by doing more separate runs, each with fewer sources, but this would require significant changes to the inversion software framework. All results presented here use the *a priori* model given in [7] with the NNLS solver.

Figure 56 shows the high resolution *a priori* mean emission profile for the 2011 Grímsvötn eruption. Comparing with the corresponding lower resolution profile in figure 29, one can see the additional detail allowed by the increase in resolution. Note that because we plot the source strength for each source in units of g/hr, we expect the values to be reduced by a factor of two relative to figure 29 because of the reduced source depth (in the parts of the plot where the source profile is well resolved). The plot is consistent with this, although it is not immediately obvious due to the wide dynamic range on the plot. Similar comments also apply to figures 58 and 60 below.

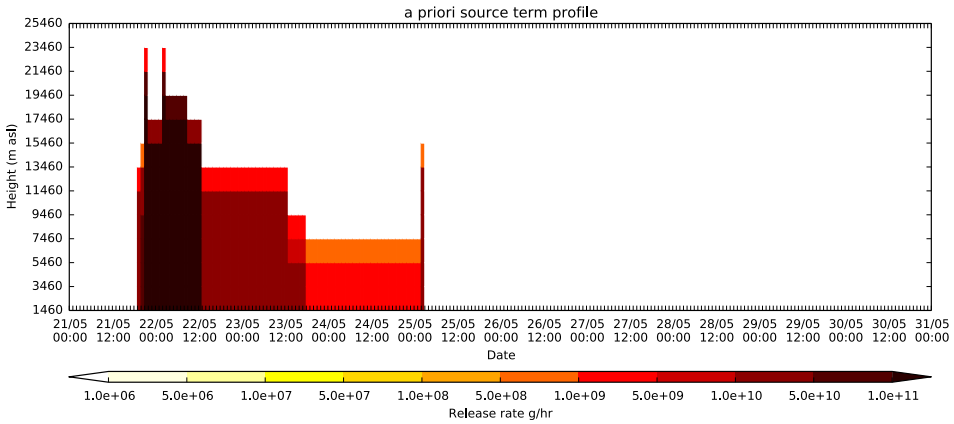

Figure 56: The high resolution *a priori* emission profile for the eruption of Grímsvötn in May 2011.

Figure 57 shows the modelled plume between 23:00 UTC on 22/05/2011 and 00:00 UTC on 23/05/2011, obtained using the high resolution *a priori* source in figure 56. The predicted plume is similar to that given by the lower resolution *a priori* source (see figure 30).

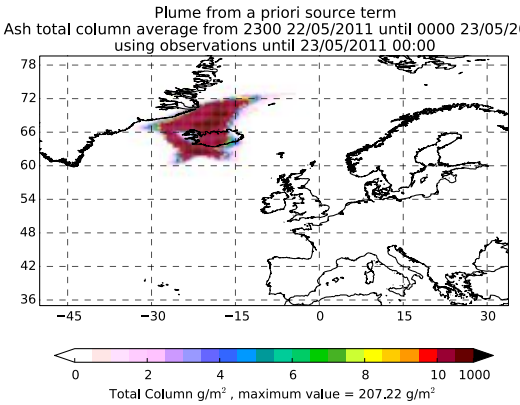

Figure 57: The NAME plume averaged between 23:00 UTC on 22/05/2011 and 00:00 UTC on 23/05/2011 for the 2011 Grímsvötn eruption, obtained using the high resolution *a priori* emission profile in figure 56.

C.1 Ash-only observations

Figure 58 shows the high resolution *a posteriori* source determined using ash-only observations until the dates given. Comparing with the lower resolution *a posteriori* emission profiles in figure 31, one can see the additional detail that the increase in resolution gives. We note, however, that the increase in temporal resolution does not yield any further detail to the *a posteriori* source on 24/05/2011. As discussed in section 5.1.1, on 24/05/2011 the inversion makes only small changes to the *a priori* mean emissions which themselves have little small scale structure.

Figure 59 shows the modelled plume between 23:00 UTC on 22/05/2011 and 00:00 UTC on 23/05/2011 using the high resolution *a posteriori* emission profiles in figure 58, together with the ash observations from the satellite retrieval valid at the same time. Comparing figure 59 with the modelled plume obtained using the lower resolution emission profiles (see figure 32) we see some small differences. In particular, the regions north of Iceland with high column loads cover a smaller area when the higher resolution emission profiles are used. There are also some significant differences in maximum column loads.

Table 7 compares the run-time of the inversion calculation for the higher resolution source to the corresponding run-time for the original, lower resolution, source. The resolution of the source has increased by a factor of 6 (a factor of 2 in the vertical and a factor of 3 in time). The run-time of the inversion calculation has, however, increased by a factor of more than 30.

Source resolution	Run-time
Low (4 km and 3-hourly)	0 min 12.860 sec
High (2 km and hourly)	7 min 45.808 sec

Table 7: The inversion run time for the determined solution using 3293 ash-only satellite observations until 00:00 UTC on 31/05/2011 from the 2011 Grímsvötn eruption.

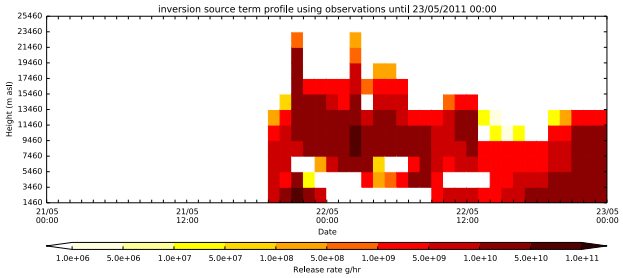

(a) emissions using satellite retrievals up to 00:00 UTC 23/05/2011

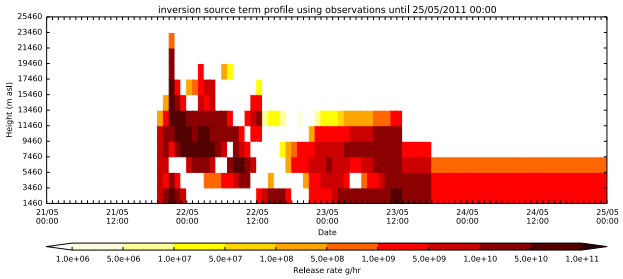

(b) emissions using satellite retrievals up to 00:00 UTC 25/05/2011

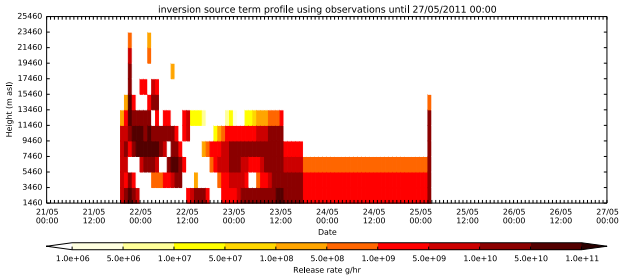

(c) emissions using satellite retrievals up to 00:00 UTC 27/05/2011

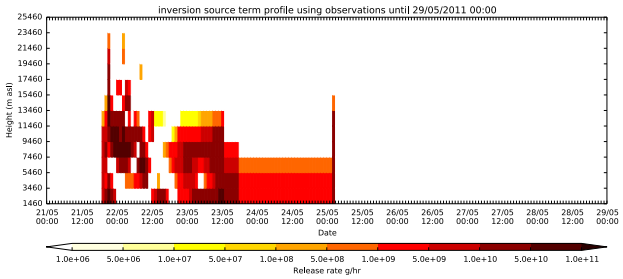

(d) emissions using satellite retrievals up to 00:00 UTC 29/05/2011

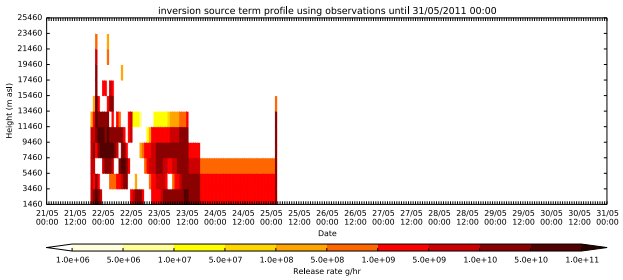

(e) emissions using satellite retrievals up to 00:00 UTC 31/05/2011

Figure 58: The best fit high resolution emission profile for the eruption of Grímsvötn using ash-only satellite observations. (Note the different scales used along the time axis.)

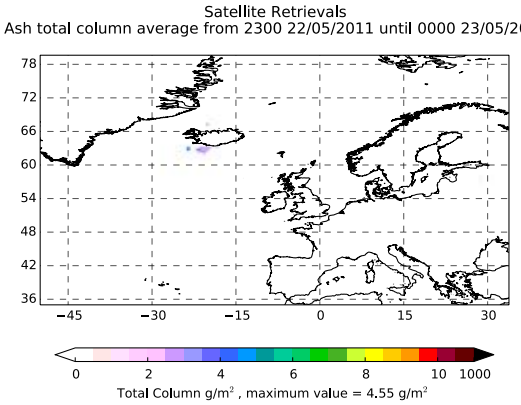

(a) ash-only satellite retrievals

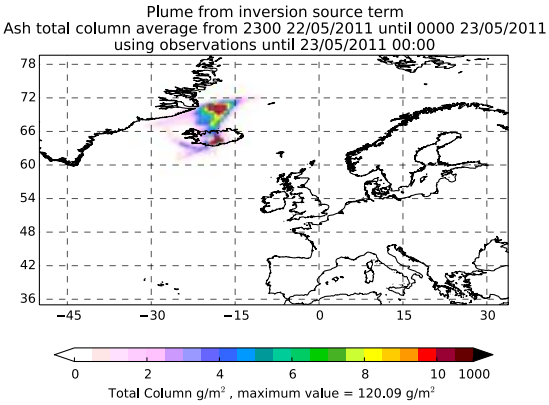

(b) plume using retrievals up to 00:00 UTC 23/05/2011

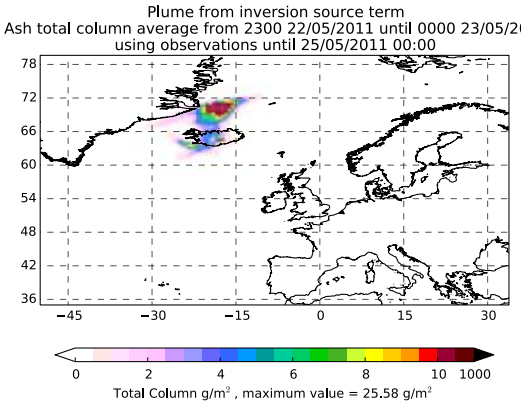

(c) plume using retrievals up to 00:00 UTC 25/05/2011

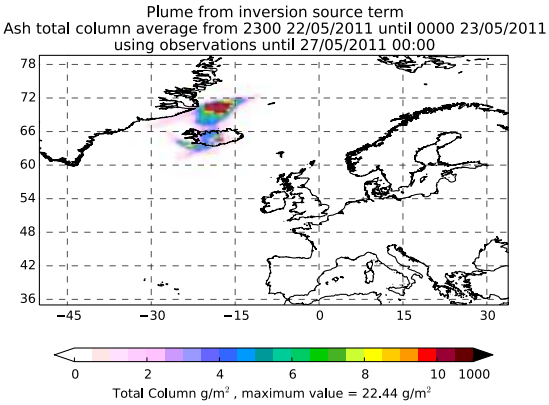

(d) plume using retrievals up to 00:00 UTC 27/05/2011

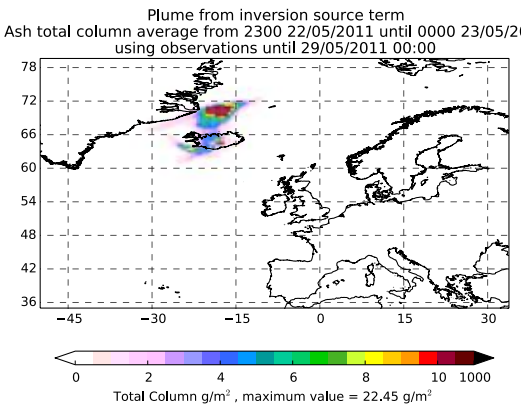

(e) plume using retrievals up to 00:00 UTC 29/05/2011

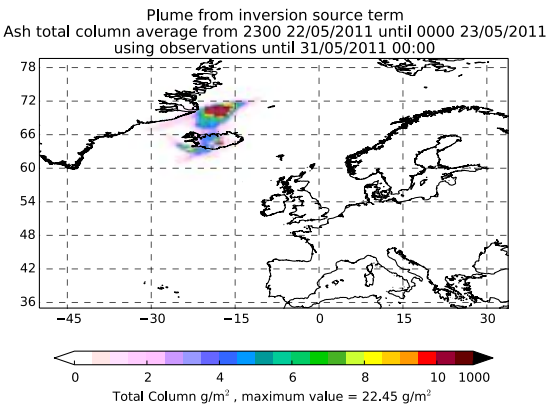

(f) plume using retrievals up to 00:00 UTC 31/05/2011

Figure 59: The Grímsvötn plume averaged between 23:00 UTC on 22/05/2011 and 00:00 UTC on 23/05/2011: (a) as observed by satellite (ash only); and (b-f) as predicted by NAME with high resolution emissions determined using ash-only satellite observations.

C.2 Ash and clear sky observations

Figure 60 shows the high resolution *a posteriori* source determined using both ash and clear sky observations until the dates given. Comparing with the lower resolution *a posteriori* emission profiles in figure 33, one can again see the additional detail that the increase in resolution gives.

Figure 61 shows the modelled plume between 23:00 UTC on 22/05/2011 and 00:00 UTC on 23/05/2011 using the high resolution *a posteriori* emission profiles in figure 60, together with the satellite observations valid at the same time. While the plume looks very similar to the results with the lower resolution source in figure 34, there are, as for the ash-only case, some significant differences in maximum column loads.

Table 8 compares the run-time of the inversion calculation for the higher resolution source to the corresponding run-time for the original, lower resolution, source. The run-time of the inversion calculation has, in this case, increased by a factor of about 6 which is in line with the increase in resolution of the source.

Source resolution	Run-time
Low (4 km and 3-hourly)	1 min 5.287 sec
High (2 km and hourly)	7 min 25.196 sec

Table 8: The inversion run time for the determined solution using 88791 satellite observations (both ash and clear skies) until 00:00 UTC on 31/05/2011 from the 2011 Grímsvötn eruption.

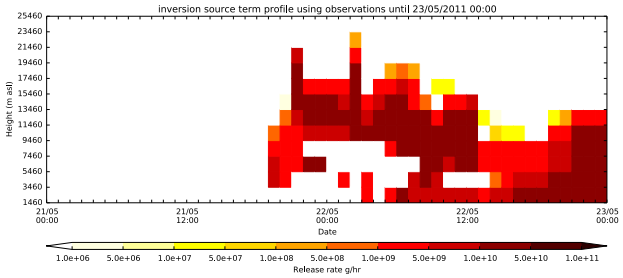

(a) emissions using satellite retrievals up to 00:00 UTC 23/05/2011

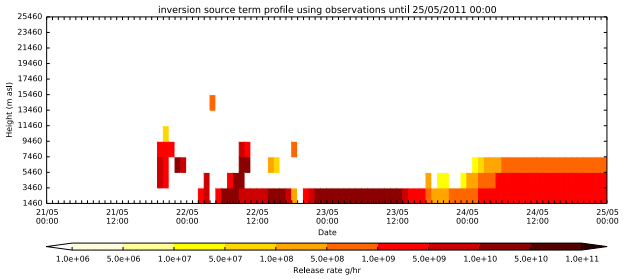

(b) emissions using satellite retrievals up to 00:00 UTC 25/05/2011

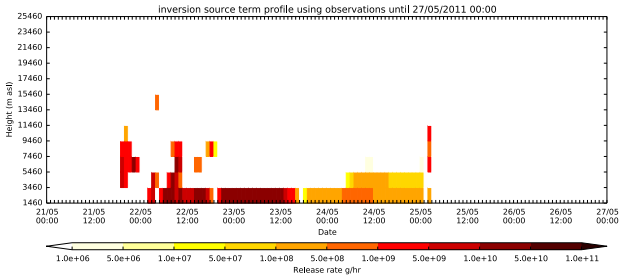

(c) emissions using satellite retrievals up to 00:00 UTC 27/05/2011

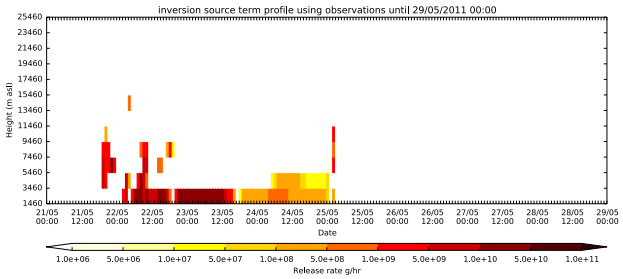

(d) emissions using satellite retrievals up to 00:00 UTC 29/05/2011

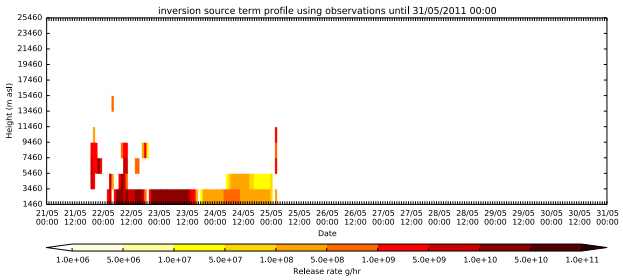

(e) emissions using satellite retrievals up to 00:00 UTC 31/05/2011

Figure 60: The best fit high resolution emission profile for the eruption of Grímsvötn using both ash and clear sky satellite observations. (Note the different scales used along the time axis.)

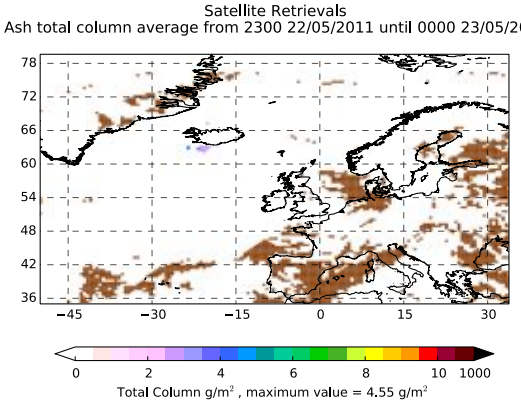

(a) ash and clear sky satellite retrievals

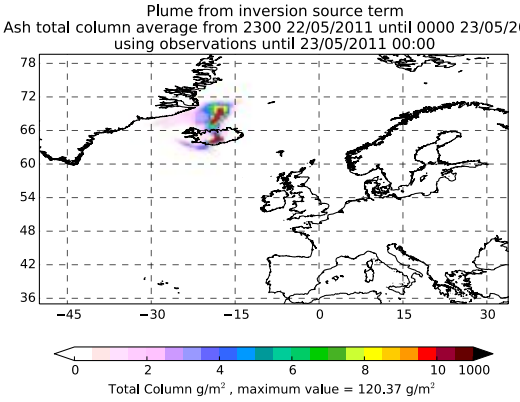

(b) plume using retrievals up to 00:00 UTC 23/05/2011

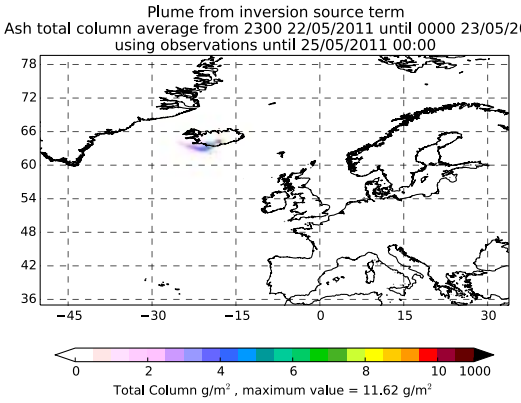

(c) plume using retrievals up to 00:00 UTC 25/05/2011

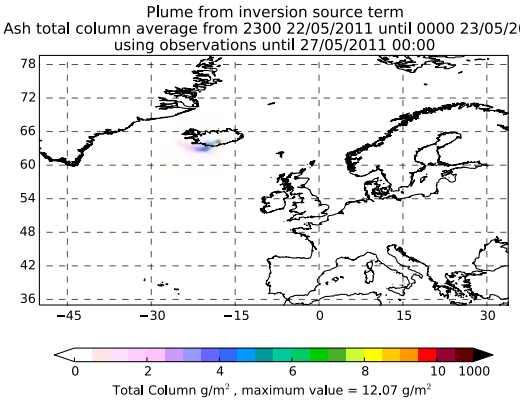

(d) plume using retrievals up to 00:00 UTC 27/05/2011

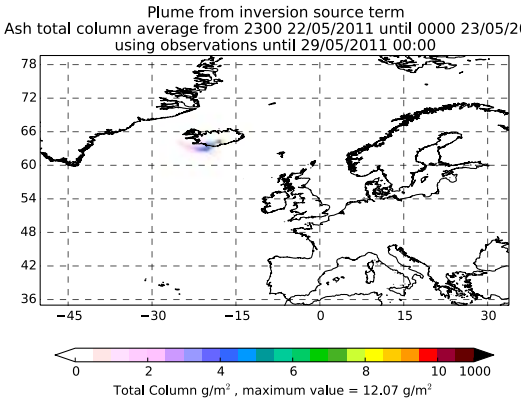

(e) plume using retrievals up to 00:00 UTC 29/05/2011

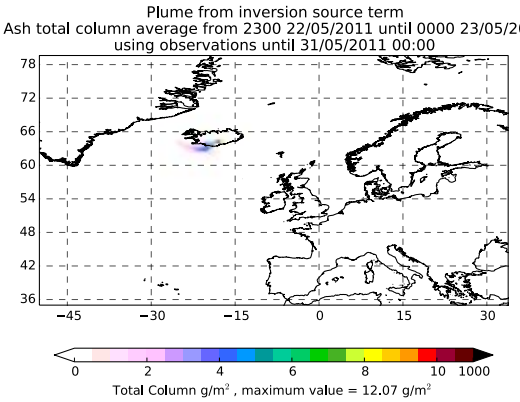

(f) plume using retrievals up to 00:00 UTC 31/05/2011

Figure 61: The Grímsvötn plume averaged between 23:00 UTC on 22/05/2011 and 00:00 UTC on 23/05/2011: (a) as observed by satellite (ash and clear skies, with clear skies shown in brown); and (b-f) as predicted by NAME with high resolution emissions determined using both ash and clear sky satellite observations.

References

[1] Anderson, E., Z. Bai, C. Bischof, S. Blackford, J. Demmel, J. Dongarra, J. Du Croz, A. Greenbaum, S. Hammarling, A. McKenney and D. Sorensen (1999) LAPACK Users' Guide, 3rd edition. Society for Industrial and Applied Mathematics, Philadelphia.

[2] Kristiansen, N. I., A. Stohl, F. J. Prata, N. Bukowiecki, H. Dacre, S. Eckhardt, S. Henne, M. C. Hort, B. T. Johnson, F. Marenco, B. Neininger, O. Reitebuch, P. Seibert, D. J. Thomson, H. N. Webster and B. Weinzierl (2012) Performance assessment of a volcanic ash transport model mini-ensemble used for inverse modeling of the 2010 Eyjafjallajökull eruption. *J. Geophys. Res.,* doi:10.1029/2011JD016844, **117,** D00U11.

[3] Lawson, C. L., and R. J. Hanson (1974) Solving least squares problems. Prentice-Hall.

[4] Mastin, L. G., M. Guffanti, R. Servranckx, P. Webley, S. Barsotti, K. Dean, A. Durant, J. W. Ewert, A. Neri, W. I. Rose, D. Schneider, L. Siebert, B. Stunder, G. Swanson, A. Tupper, A. Volentik and C. F. Waythomas (2009) A multidisciplinary effort to assign realistic source parameters to models of volcanic ash-cloud transport and dispersion during eruptions. *J. Volcanol. and Geotherm. Res.,* **186,** 10-21.

[5] Pelley, R. E., M. C. Cooke, A. J. Manning, D. J. Thomson, C. S. Witham and M. C. Hort (2015) Initial Implementation of an Inversion Technique for Estimating Volcanic Ash Source Parameters in Near Real time using Satellite Retrievals. *Forecasting Research Technical Report* 604, Met Office, UK.

[6] Press, W. H., S. A. Teukolsky, W. T. Vetterling and B. P. Flanner (1992) Numerical Recipes in Fortran: The Art of Scientific Computing, 2nd edition. Cambridge University Press, New York.

[7] Thomson, D. J., H. N. Webster and M. C. Cooke (2017) Developments in the Met Office InTEM volcanic ash source estimation system Part 1: Concepts. *Forecasting Research Technical Report* 616, Met Office, UK.

[8] Webster, H. N., D. J. Thomson, B. T. Johnson, I. P. C. Heard, K. Turnbull, F. Marenco, N. I. Kristiansen, J. Dorsey, A. Minikin, B. Weinzierl, U. Schumann, R. S. J. Sparks, S. C. Loughlin, M. C. Hort, S. J. Leadbetter, B. J. Devenish, A. J. Manning, C. S. Witham, J. M. Haywood and B. W. Golding (2012) Operational prediction of ash concentrations in the distal volcanic cloud from the 2010 Eyjafjallajökull eruption. *J. Geophys. Res.,* doi:10.1029/2011JD016790, **117,** D00U08.

Met Office
FitzRoy Road, Exeter
Devon, EX1 3PB
UK

Tel: 0370 900 0100
Fax: 0370 900 5050
enquiries@metoffice.gov.uk
www.metoffice.gov.uk

Produced with the Met Office LaTeX template v2.0.0